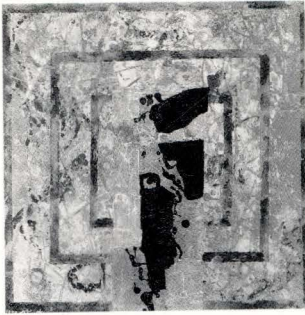



FUJITSU

**SCIENTIFIC & TECHNICAL
JOURNAL**

Summer 1990 VOL.26, NO.2





This Issue's Cover:

Creativity by Yukinobu Kudoh

What is the essence of mankind? Creativity. Through history, tools, the arts, and civilizations have been created by our ancestors' developed brains and by creativity.

To develop computers is indeed to challenge the complex mechanics of the human brain. Today, computer technology is approaching the complexity of the human brain, creating artificial intelligence, neurocomputers, and fuzzy computers.

High-performance computers with intricate brains will allow human life to be comfortable and enriched.

FUJITSU Scientific & Technical Journal is published quarterly by FUJITSU LIMITED of Japan to report the results of research conducted by FUJITSU LIMITED, FUJITSU LABORATORIES LTD., and their associated companies in communications, electronics, and related fields. It is the publisher's intent that FSTJ will promote the international exchange of such information, and we encourage the distribution of FSTJ on an exchange basis. All correspondence concerning the exchange of periodicals should be addressed to the editor.

FSTJ can be purchased through KINOKUNIYA COMPANY LTD., 3-17-7 Shinjuku, Shinjuku-ku, Tokyo 160-91, (Telex No. 2424344, answerback KINOKUNI J).

The price is US \$7.00 per copy, excluding postage.

FUJITSU LIMITED reserves all rights concerning the republication and publication after translation into other languages of articles appearing herein.

Permission to publish these articles may be obtained by contacting the editor.

FUJITSU LIMITED Takuma Yamamoto, *President*
FUJITSU LABORATORIES LTD. Masaka Ogi, *President*

Editorial Board

Editor Takahiko Misugi
Associated Editors Yukio Fukukawa Shigeru Sato

Editorial Representatives

Kunihiko Asama	Masakazu Fujita	Tatsuzumi Furukawa
Kazuhisa Kobayashi	Masaaki Kobayashi	Yoshimasa Miura
Makoto Mukai	Seiya Ogawa	Shinji Ohkawa
Shinya Okuda	Hirofumi Okuyama	Tohru Sato
Yoshio Tago	Shozo Taguchi	Jyun'ichi Tanahashi
Hirobumi Takanashi	Mitsuhiko Toda	Toru Tsuda
Akira Yoshida		

Editorial Coordinator

Kazuo Yono

FUJITSU LIMITED 1015 Kamikodanaka, Nakahara-ku,
Kawasaki 211, Japan

Cable Address: FUJITSULIMITED KAWASAKI

Telephone: +81-44-777-1111

Telex: 3842122, 3842221, 3842802, 3842803,
Answerback FTWKAW J

Printed by MIZUNO PRITECH Co., Ltd. in Japan
© 1990 FUJITSU LIMITED (June 14, 1990)

CONTENTS

Papers

- 115 **A Cubic Curve Generation LSI**
● Masayuki Okamoto ● Mitsuru Yamauchi ● Tomohiro Fukuoka
- 123 **Bi-Substituted Magnetic Garnet Film and its Application to an Optical Isolator**
● Hidema Uchishiba ● Masao Shibayama
- 131 **Magnetic Circuit Yoke by Metal Injection Molding**
● Yoshihiko Seyama ● Tsutomu Iikawa
- 138 **Bistable Laser Diode for Optical Signal Processing**
● Tetsufumi Odagawa ● Tatsuyuki Sanada ● Shigenobu Yamakoshi
- 149 **High Performance p-Substrate Buried Heterostructure Laser Emitting at 1.3 μm**
● Katsuhiko Kihara ● Shuichi Miura ● Ichiro Ushijima
- 156 **Sputtered Garnet Media for Magneto-Optic Recording**
● Keiji Shono ● Hiroshi Kano ● Sumio Kuroda

UDC 512.77:621.3.049.771.44

FUJITSU Sci. Tech. J., 26, 2, pp. 115-122(1990)

A Cubic Curve Generation LSI

• Masayuki Okamoto • Mitsuru Yamauchi • Tomohiro Fukuoka

This paper describes the processing algorithm, hardware architecture, and application of the Cubic Curve Engine (Cu²E). The Cu²E generates the coordinates of polygonal lines by approximating to the cubic Bézier curve or the cubic B-spline curve. The approximating algorithm is a combination of the midpoint subdivision and error calculation method. This LSI can transform the data which define a curve. It was designed using synchronous pipeline architecture and interfaces with TOKEN format data. Fujitsu has adopted a 1.2 μm CMOS fabrication technology, and has achieved such a high speed performance that the LSI can generate one million coordinates per second.

UDC 537.632:679.87

FUJITSU Sci. Tech. J., 26, 2, pp. 123-130(1990)

Bi-Substituted Magnetic Garnet Film and its Application to an Optical Isolator

• Hidema Uchishiba • Masao Shibayama

The growth and magneto-optical properties of thick epitaxial iron garnet films of composition (Tb_{3-x}Bi_x)(FeGaAl)₅O₁₂ and its application to an optical isolator were investigated. The influence of Bi³⁺ ions on the magneto-optical properties was determined experimentally, and Faraday rotation coefficients of 2370 deg/cm at a wavelength (λ) of 1.31 μm and 1590 deg/cm at 1.55 μm were obtained with x = 1.6. For λ = 1.55 μm, the film thickness required to obtain a 45° Faraday rotation was 280 μm. Also, an optical isolator mounted on an anisotropically etched silicon substrate was proposed. An extinction ratio of about 40 dB and an insertion loss of less than 0.3 dB were obtained after temperature cycle testing.

UDC 621.3.042:669-138

FUJITSU Sci. Tech. J., 26, 2, pp. 131-137(1990)

Magnetic Circuit Yoke by Metal Injection Molding

• Yoshihiko Seyama • Tsutomu Iikawa

Metal injection molding has attracted substantial attention in the powder metallurgy field because of the technology's promise for manufacturing parts with complex shapes.

An attempt has been made to apply the metal injection molding technology to the production of a magnetic circuit yoke. The yoke has a complex shape and is made from a soft magnetic alloy, Fe-50%Co, which has low workability due to its hardness and brittleness.

In this paper, the optimum starting powders and plastic binders, and the mixing which most affects metal injection molding were investigated. As a result, an Fe-50%Co alloy magnetic circuit yoke with a complex shape was obtained having good magnetic properties.

UDC 621.375.826:621.391

FUJITSU Sci. Tech. J., 26, 2, pp. 138-148(1990)

Bistable Laser Diode for Optical Signal Processing

• Tetsufumi Odagawa • Tatsuyuki Sanada
• Shigenobu Yamakoshi

A bistable laser diode with a saturable absorber was studied for optical signal processing from two points of view. First, for fast operation using optical set and electrical reset signals, the carrier density change caused by the electrical reset was decreased by optimizing the bias voltage of the laser. As a result, fast flip-flop operation at a 2.5 Gbit/s repetition rate was achieved. Second, for all-optical signal processing which will be important for future optical systems, a new optical reset using gain quenching was proposed and confirmed. All-optical flip-flop operation is demonstrated.

UDC 679.87:681.327.68

FUJITSU Sci. Tech. J., 26, 2, pp. 156-163(1990)

High Performance p-Substrate Buried Heterostructure Laser Emitting at 1.3 μm

• Katsuhiro Kihara • Shuichi Miura • Ichiro Ushijima

A high performance buried heterostructure laser diode emitting at 1.3 μm has been developed by applying a p-substrate to a flat-surface buried heterostructure. A high internal quantum efficiency of 94.3 percent, a very low threshold current of 5.8 mA at 25 °C, and a high temperature operation (for example, up to 15 mW at 100 °C) have been achieved with this structure. An error-floor-free transmission of up to 600 Mbit/s NRZ using pseudo-random modulation with a -80 ps/nm fiber dispersion and up to 1.2 Gbit/s with a -40 ps/nm fiber dispersion have also been obtained. Moreover, a high reliability (median lifetime of more than 1 × 10⁶ h for 70 °C at 5 mW) has been realized.

UDC 621.375.826:621.391.5

FUJITSU Sci. Tech. J., 26, 2, pp. 149-155(1990)

Sputtered Garnet Media for Magneto-Optic Recording

• Keiji Shono • Hiroshi Kano • Sumio Kuroda

In-situ crystallized Bi-substituted iron garnet films were deposited by RF sputtering. The films had a columnar microstructure and the surfaces were as smooth as a single crystal. They showed square hysteresis loops with large coercivity.

The films' perpendicular magnetic anisotropy is ascribed to inverse magnetostriction. A disk four inches in diameter was dynamically recorded using an Ar ion laser. The figure of merit of the disk with an Al reflector was about ten times higher than that of a magneto-optic disk made of an amorphous rare-earth transition metal. CNRs of 57 dB and 54 dB were obtained for bit lengths of 5 μm and 1.4 μm, respectively.

A Cubic Curve Generation LSI

• Masayuki Okamoto • Mitsuru Yamauchi • Tomohiro Fukuoka

(Manuscript received November 30, 1989)

This paper describes the processing algorithm, hardware architecture, and application of the Cubic Curve Engine (Cu²E). The Cu²E generates the coordinates of polygonal lines by approximating to the cubic Bézier curve or the cubic B-spline curve. The approximating algorithm is a combination of the midpoint subdivision and error calculation method. This LSI can transform the data which define a curve. It was designed using asynchronous pipeline architecture and interfaces with TOKEN format data. Fujitsu has adopted a 1.2 μm CMOS fabrication technology, and has achieved such a high speed performance that the LSI can generate one million coordinates per second.

1. Introduction

Curves have been used as a common technology for high quality outline fonts. In the case of Kanji characters, it has been difficult to generate high quality fonts without such curves. Recently, most of the high quality Kanji outline fonts have used the cubic Bézier curve or the cubic B-spline curve. This curve is usually generated by software on the processor. However, the speed has been too low for systems required to produce thousands of characters per second, for example, desk top publishing systems (DTP). A high speed curve generator is required for such systems.

PostScript^{Note)}, which is becoming a standard of PDL (Page Description Language), supports the cubic Bézier curve. One of the features of Postscript, is that it approximates a cubic curve to a polygonal line. In PostScript, the error between the original curve and the approximated polygonal line, called the flatness parameter, is programmable by the user¹⁾.

Cu²E satisfies PostScript's specifications and the demands of high speed outline font generation.

2. Characteristics of the cubic curve^{2), 3)}

2.1 The Bézier curve

The shape of the cubic Bézier curve is shown in Fig. 1.

Given the four points Q_{00} , Q_{01} , Q_{02} , and Q_{03} , the curve passes through Q_{00} and Q_{03} and is laid within the concave sections defined by the control points. Therefore, its shape can be visualized from the control points.

The cubic Bézier curve is given by the following equation using the parameter t :

$$P(t) = [t^3 \ t^2 \ t \ 1] \begin{bmatrix} -1 & 3 & -3 & 1 \\ 3 & -6 & 3 & 0 \\ -3 & 3 & 0 & 0 \\ 1 & 0 & 0 & 0 \end{bmatrix} \begin{bmatrix} Q_{00} \\ Q_{01} \\ Q_{02} \\ Q_{03} \end{bmatrix}, \quad \dots \dots \dots (1)$$

where

$$0 \leq t \leq 1. \quad \dots \dots \dots (2)$$

Using the cubic Bézier curve to obtain the outline font is practical for simple characters such as letters and numerals.

2.2 The B-spline curve

There are two methods to define the cubic B-spline curve using the Cu²E LSI. One is to define the control points of the curve. The other is to define the knot points of the curve.

An example of continuous B-spline segments defined by control points is shown in Fig. 2.

Note: PostScript is trade mark of Adobe Systems Inc.

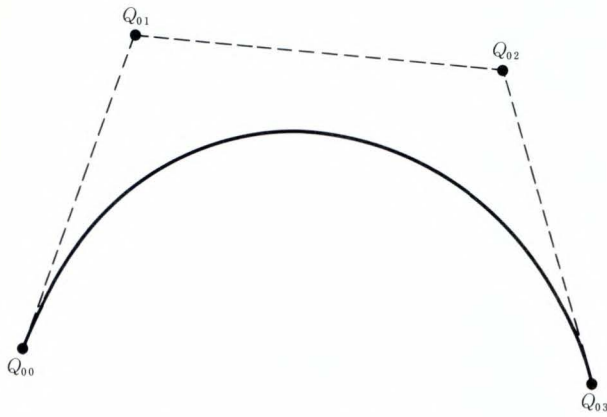


Fig. 1—Cubic Bézier curve.

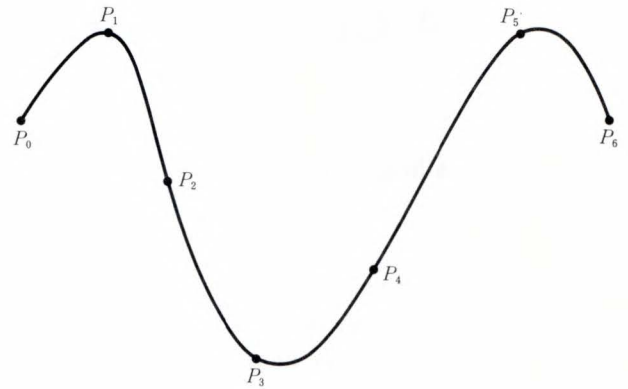


Fig. 3—Cubic B-spline curve defined by knot points.

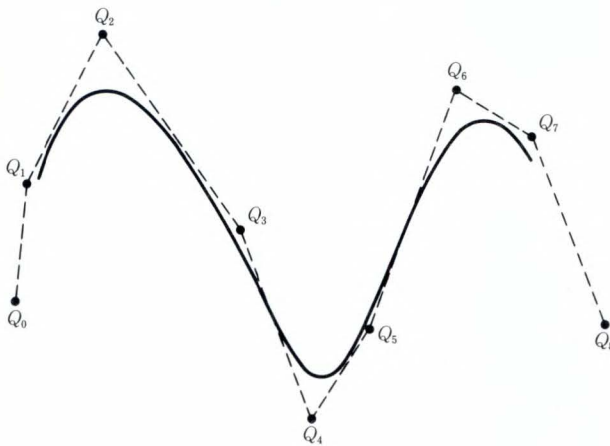


Fig. 2—Cubic B-spline curve defined by control points.

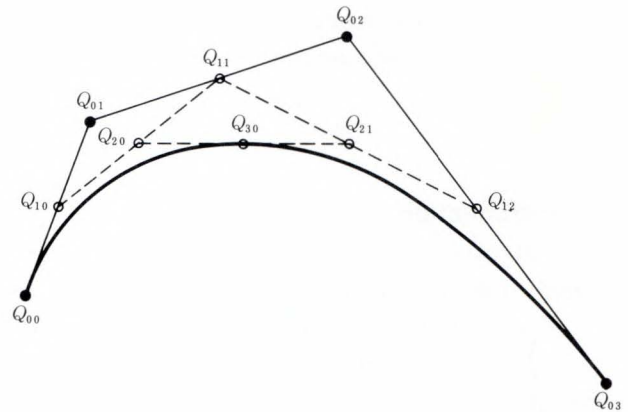


Fig. 4—Midpoint subdivision.

Generally, the curve does not pass through all control points but is laid within the concave sections defined by the control points. Therefore, its shape can be visualized from the control points. When a control point is moved, the shape of just a few adjacent segments will be affected (local controllability).

The cubic B-spline curve defined by four control points Q_{i-1} , Q_i , Q_{i+1} , and Q_{i+2} is given as

$$P(t) = [t^3 \ t^2 \ t \ 1] \frac{1}{6} \begin{bmatrix} -1 & 3 & -3 & 1 \\ 3 & -6 & 3 & 0 \\ -3 & 0 & 3 & 0 \\ 1 & 4 & 1 & 0 \end{bmatrix} \begin{bmatrix} Q_{i-1} \\ Q_i \\ Q_{i+1} \\ Q_{i+2} \end{bmatrix}, \quad \dots \dots \dots (3)$$

where

$$0 \leq t \leq 1. \quad \dots \dots \dots (4)$$

An example of a shape defined by knot points is shown in Fig. 3. In the case of a curve

defined by knot points, the curve passes through all knot points. When a knot point is moved, the shape of all curve segments will be affected (global controllability).

The cubic B-spline curve is defined by less data and can define smooth continuous curves. Therefore, using the cubic B-spline curve as an outline font is effective for complicated characters such as Kanji.

3. Processing algorithm of Cu²E LSI

3.1 Approximation of a curve to a polygonal line

The approximation algorithm of the Cu²E is a combination of midpoint subdivision and an error calculation method to complete the calculation.

3.1.1 Subdividing a curve²⁾

A parametric curve segment can be generated using Equation (1). However, this method

increases the load on hardware because it requires floating point calculation. There is a simpler algorithm called the midpoint subdivision algorithm, that calculates the midpoint (parameter $t = 0.5$) on the Bézier curve.

Provided the four control points Q_{00} , Q_{01} , Q_{02} , and Q_{03} of the cubic Bézier curve are as shown in Fig. 4, the midpoint on the curve can be obtained using the following equations:

$$Q_{10} = (Q_{00} + Q_{01})/2. \quad \dots\dots\dots (5)$$

$$Q_{11} = (Q_{01} + Q_{02})/2. \quad \dots\dots\dots (6)$$

$$Q_{12} = (Q_{02} + Q_{03})/2. \quad \dots\dots\dots (7)$$

$$Q_{20} = (Q_{10} + Q_{11})/2. \quad \dots\dots\dots (8)$$

$$Q_{21} = (Q_{11} + Q_{12})/2. \quad \dots\dots\dots (9)$$

$$Q_{30} = (Q_{20} + Q_{21})/2. \quad \dots\dots\dots (10)$$

Point Q_{30} becomes the midpoint of the given cubic Bézier curve. The curve is divided into two segments and smaller curves defined by Q_{00} , Q_{10} , Q_{20} , and Q_{30} ; and Q_{30} , Q_{21} , Q_{12} , and Q_{03} . The Cu²E repeats the same procedure for each segment of the divided curves. When the subdivided curves become small enough, the approximation of the curve to a polygonal line is completed.

This algorithm is realized by the execution of add and bit-shift operations that can be implemented on LSI.

3.1.2 Error calculation

It is necessary to specify at what point the midpoint subdivision process should be finished. For this purpose, the error parameter *ERR* (flatness parameter in PostScript) is introduced in the Cu²E operation. The subdivision process is completed, when the calculated error becomes smaller than the given value of *ERR*. It is difficult to compute the error between a curve and an approximated line. Therefore, the Cu²E uses an approximating calculation that computes the error at high speed without lowering the quality of the generated curve. The error is calculated from the coordinates of four control points Q_{00} , Q_{01} , Q_{02} , and Q_{03} using the following equation:

$$ERR = |(Q_{00} + Q_{03})/2 - (Q_{01} + Q_{02})/2|. \quad \dots\dots\dots (11)$$

This equation is applied to the characteristics

of cubic Bézier curves laid within the concave sections defined by the control points. The calculation is executed by add, subtract, and bit-shift operations.

3.2 Transformation of B-spline curves³⁾

It is possible to transform a B-spline curve into a Bézier curve without losing the shape. The Cu²E can perform this transformation.

The B-spline control points Q_{i-1} , Q_i , Q_{i+1} , and Q_{i+2} are transformed into the control points of the cubic Bézier curve Q_{00} , Q_{01} , Q_{02} , and Q_{03} using the following equation:

$$\begin{bmatrix} Q_{00} \\ Q_{01} \\ Q_{02} \\ Q_{03} \end{bmatrix} = \frac{1}{6} \begin{bmatrix} 1 & 4 & 1 & 0 \\ 0 & 4 & 2 & 0 \\ 0 & 2 & 4 & 0 \\ 0 & 1 & 4 & 1 \end{bmatrix} \begin{bmatrix} Q_{i-1} \\ Q_i \\ Q_{i+1} \\ Q_{i+2} \end{bmatrix} \quad \dots (12)$$

The knot points of the B-spline curve are transformed into the Bézier control points via the B-spline control points. The B-spline control points can be calculated to solve the simultaneous equations for the knot points of the B-spline curve.

4. Hardware

The block diagram of the Cu²E LSI is shown in Fig. 5. The LSI consists of a DATA INPUT BLOCK (DI), DATA OUTPUT BLOCK (DO), two identical OPERATION BLOCKs (OP), a STACK RAM, and a CONTROL BLOCK (CTL).

4.1 DATA INPUT BLOCK and DATA OUTPUT BLOCK

The Cu²E has two 16-bit external busses. These are the input data bus and the output data bus. They were designed using asynchronous pipeline architecture with a two-line handshake connection. This architecture is suitable for the Cu²E LSI because the data output timing and the number of output coordinates vary with the shape of the given curve. A FIFO memory is included in DI (2-word) and DO (4-word) for asynchronous operation. The interfaces of the Cu²E LSI are connected to a preprocessor, for example, a coordinate transformation processor, and are connected to a postprocessor, for example, a drawing processor.

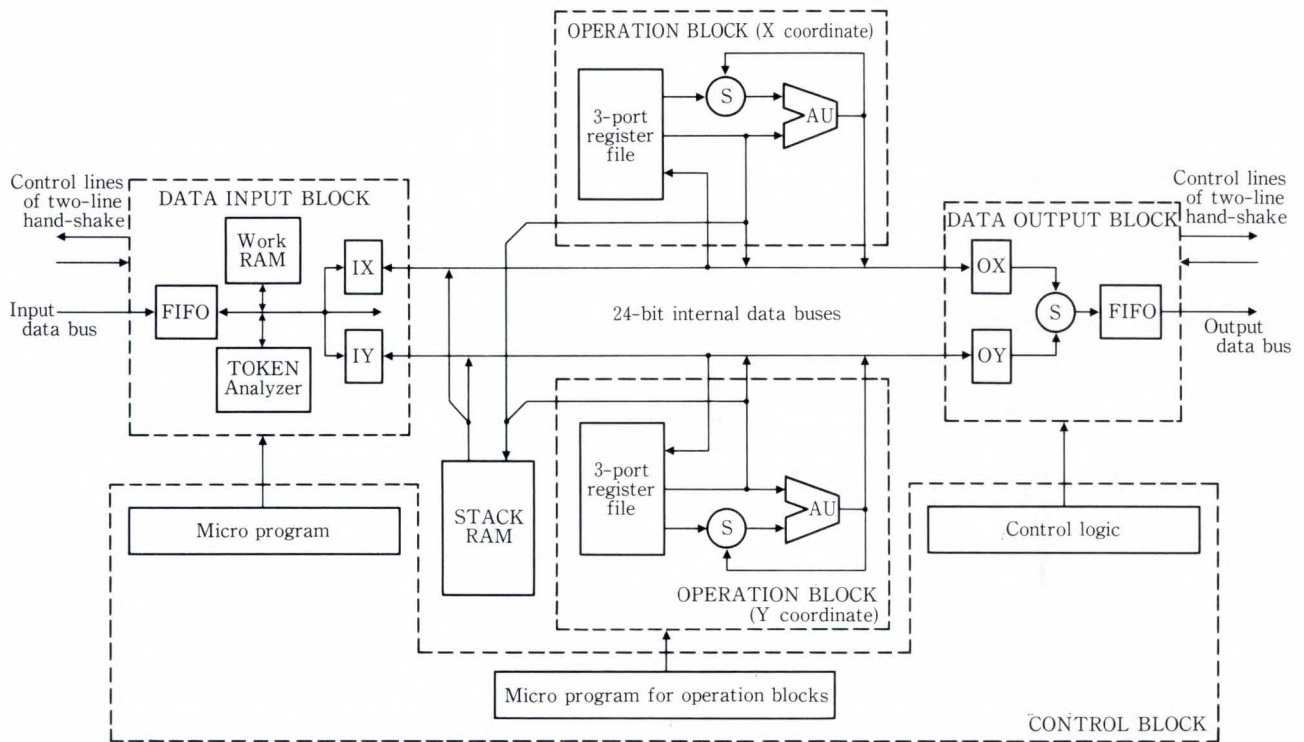


Fig. 5—Block diagram of Cu²E.

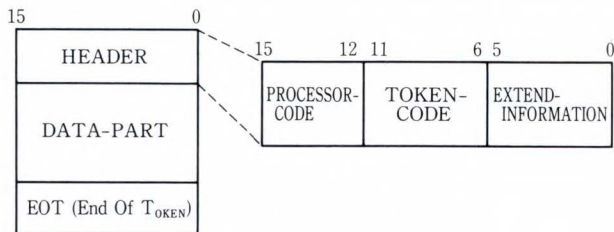


Fig. 6—TOKEN format.

The input and output data are in TOKEN format and consist of the HEADER, DATA-PART, and EOT (End Of TOKEN) (see Fig. 6). The HEADER is separated into the PROCESSOR-CODE (PC), TOKEN-CODE (TC), and EXTEND-INFORMATION (EI). The PC defines which processor is selected for the given TOKEN. The TC defines the data format of the DATA-PART and the type of data processing to be executed. The EI defines further information on each TC. The TOKEN ANALYZER UNIT in DI analyzes the input HEADER and outputs the TOKEN analyzed information. This information is used in the CTL to determine processing for the input TOKEN.

The other function of DI is to preprocess the

data for the OPs. The input data is converted from 16 bit integers to 24-bit fixed point values at the DI. The DI constructs a set of four B-spline control points.

4.2 OPERATION BLOCK and STACK RAM

The OPs are connected to the DI and DO via dual 24-bit internal data busses. One of these busses is dedicated to X coordinates and the other to Y coordinates. These busses are used to retrieve (POP) data from the STACK RAM, but are not used to store (PUSH) data into the STACK RAM. Other data lines are connected directly between the OPs and the STACK RAM block so that the PUSH operation can be executed in parallel with other operations. The performance of OPs is therefore not reduced even if the PUSH operation is executed.

The OP includes a 3-port REGISTER-FILE (REG: 8 × 24-bit, 2-read/1-write) and a 24-bit ARITHMETIC UNIT (AU) consisting of a 24-bit adder and a 24-bit bit-shifter. The AU has MSB correction logic to avoid overflow at mid-point calculation. The AU outputs information indicating the sign of the result. This sign infor-

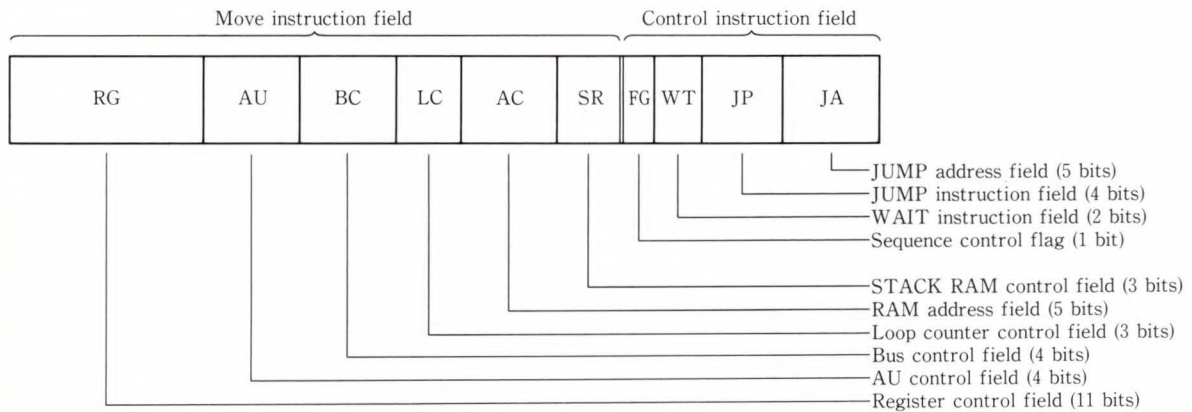


Fig. 7—Micro instruction field for OPs.

mation becomes the condition used to determine when to finish a subdividing process. Whether *ERR* or the calculating error is the bigger value can be determined at high speed.

The primary function of the OP is to calculate the midpoint as performed by the midpoint subdivision algorithm. The execution procedure loads two values from the REG, adds the values, shifts them in AU, and store the result into the REG. All other instructions, for example, transformation from a B-spline curve to a Bézier curve, are performed by the adder and shifter.

The STACK RAM consists of a RAM (32 × 48-bit) and a 5-bit counter to generate the RAM address for loading and storing. The STACK RAM stores the coordinate data of each subdivided curve. A pair of X and Y coordinates are stored into the STACK RAM, while the two OP blocks simultaneously execute the operation for X and Y. The STACK RAM block is also used as the work area for calculation of the simultaneous equations used to transform the B-spline knot point.

4.3 CONTROL BLOCK

The DI, DO, and OPs are controlled by their own CONTROL UNIT in the CTL. The clocks for the CONTROL UNITS and controlled BLOCKs are in anti-phase.

The DI and OP are controlled by a horizontal microprogram resident in each CONTROL UNIT. The micro instruction has a move instruction field and a control instruction field. The move instruction control the DATA-PATH,

```

NAME : CNTLO ;
ANDIN : ODLX , ODLY , FIFOR , CLRX ;
OROUT : +OGRANT , +ODSEL , +HHL , +WTFIFO , -BUSY0 ;

STATUS ;

$LOGIC : IF ^CLRX THEN GOTO S0 ;

S0'0000' : CASE ODLX , ODLY OF
0 : { OGRANT , BUSY0 , GOTO @SELF }
1 : { OGRANT , HHL , GOTO @NEXT }
2 : GOTO S4
3 : GOTO S7 ;

S1 : CASE ODLX , ODLY OF
0 : { OGRANT , HHL , GOTO @SELF }
1 : GOTO @SELF
2 : { HHL , GOTO @NEXT }
3 : { HHL , GOTO S5 } ;

S2 : HHL ,
IF FIFOR THEN { WTFIFO , GOTO @NEXT }
ELSE GOTO @SELF ;

S3 : GOTO S4 ;

S4 : IF FIFOR THEN { ODSEL , WTFIFO , OGRANT , GOTO S0 } ;
ELSE GOTO @NEXT ;

S5 : HHL ,
IF FIFOR THEN { WTFIFO , GOTO @NEXT }
ELSE GOTO @SELF ;

S6 : GOTO S7 ;

S7 : IF FIFOR THEN { ODSEL , WTFIFO , GOTO @NEXT }
ELSE GOTO @SELF ;

S8 : GOTO S9 ;

S9 : IF FIFOR THEN { WTFIFO , OGRANT , GOTO S0 }
ELSE GOTO @SELF ;

ENDSTATES ;
    
```

Fig. 8—Control sequence of the DATA OUTPUT BLOCK.

for example, gates and selectors. The control instructions manage the sequence of operations. These control instructions are conditional WAIT, conditional JUMP, and unconditional JUMP. It may happen that conditional WAIT and conditional JUMP are used at the same time; in this case, the JUMP instruction has priority. This priority enables multiway JUMP instructions and reduces the number of program steps. The step and bit length of microprograms are 160 steps and 26 bits for the DI, and 240 steps and

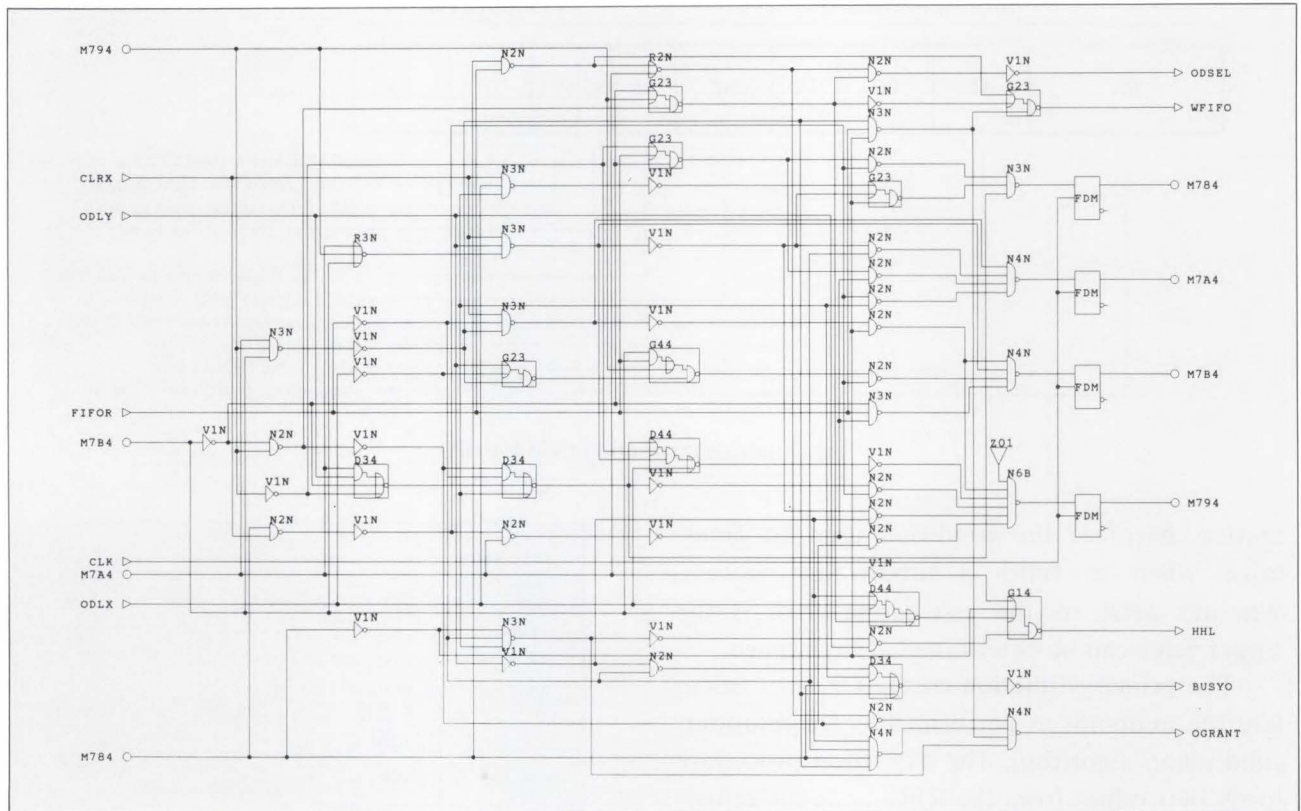


Fig. 9—Control logic for the DATA OUTPUT BLOCK.

42 bits for the OPs (see Fig. 7). The entry address of each sequence used to process the input TOKEN is decided at the CTL using the TOKEN analyzed information received from the DI.

The logic design of the CONTROL UNIT for the DO was performed on our logic synthesis tool ZEPHCADTM 4). The control sequence is written in a hardware description language (HDL) that has ten states (see Fig.8). The logic gates of this unit are generated by ZEPHCADTM as shown in Fig. 9.

4.4 Summary of the Cu²E LSI

This LSI was fabricated using 1.2 μ m CMOS Sea Of Gates (SOG) technology⁵⁾. A photograph of the chip is shown in Fig.10. The features are summarized in Table 1. It can produce 3 000-5 000 characters per second in Kanji outline font.

This LSI is suited to a two dimensional coordinate system. It is easy to expand dimen-

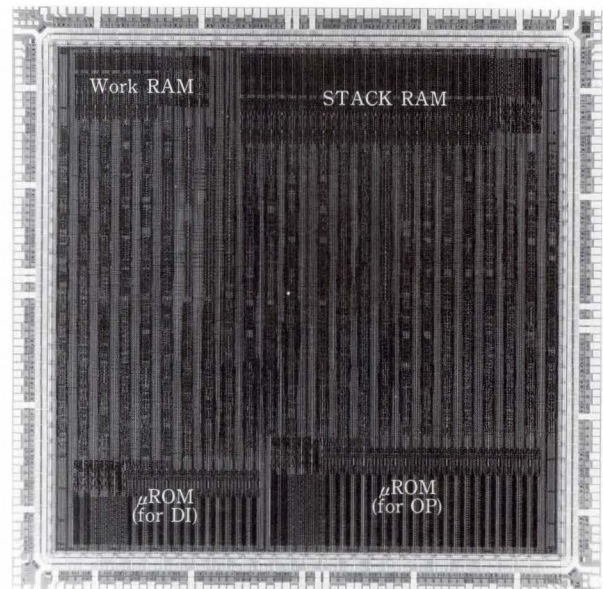


Fig. 10—Photograph of chip.

sions by adding extra OPs to the Cu²E using the same hardware architecture.

Table 1. Summary of Cu²E LSI

Physical Technology Package	CMOS 1.2 μ m triple-layer metal RIT-88
Organization	112-k basic cells
Random logic ROM	26-bit \times 160-word (microprogram for the INPUT BLOCK) 42-bit \times 240-word (microprogram for the OPERATION BLOCK)
RAM	48-bit \times 32-word (STACK RAM) 16-bit \times 12-word (work RAM)
Performance	20 MHz
Clock	20 MHz
Bézier curve approximation	1 M coordinates/s
Curve transformation	100-k segments/s (B-spline control point to Bézier control point) 70-k segments/s (B-spline knot point to B-spline control point)

5. Applications

5.1 Outline font design system

The block diagram of an example outline font design system is shown in Fig. 11.

The original font is read from the IMAGE SCANNER, converted to binary using image processing, and then stored in memory. The stored font becomes the basic data used to generate the desired outline font. A character is selected from the stored basic data and displayed on the CRT. Then, the designer assigns curves to fit the outline of displayed character. At this time, the control points of the curves are input from a pointing device such as TABLET. The input control points are transformed by the coordinate transformation processor and then input to the Cu²E to generate the curves. The generated curves are overlapped on the selected character to help the designer decide whether the curves are suitable. If the generated curves are not suitable, the designer readjusts the control points of the curves to suit the outline font data. The data is then stored in memory.

An effective way to use the Cu²E in this system is described below. First, to obtain a rough curve, the knot point of the cubic B-spline curve is used to point the shape of curve. It is easy to obtain the desired curve using the knot point because the curve passes through all of the given knot points. However, a curve defined by knot points is not suitable for fine adjust-

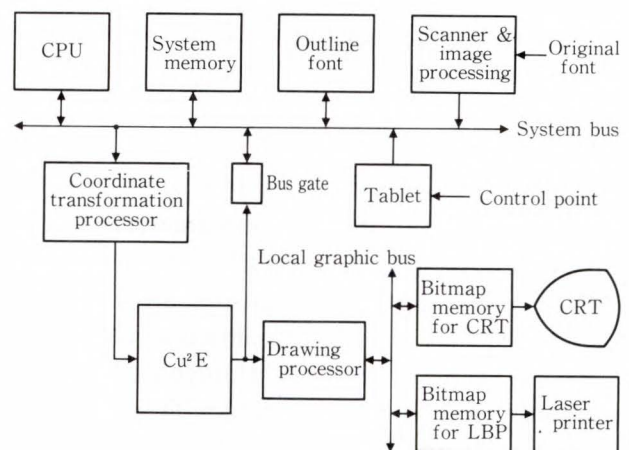


Fig. 11—Example of an outline font design system.

Table 2. Processing speed

Number of Cu ² E	Total time (clocks)	Ratio
1	28 231	1
2	20 511	0.73
3	15 309	0.54

ment because all of the curve segments are changed if a knot point is modified. Therefore, these knot points are transformed to the control points of a cubic B-spline curve using the Cu²E. The curve defined by the control points is such that only a few adjacent segments will be affected if a control point is moved. Consequently, the B-spline control points are very suitable for the fine modification of outline fonts at the final stage.

5.2 Pipeline operation of Cu²Es

The Cu²E can be connected to an asynchronous pipeline to disperse the processing. Consider the case in which three Cu²Es are connected to generate the curve defined by the B-spline knot points. In this case, each Cu²E performs the following: The first Cu²E transforms the B-spline knot points to B-spline control points; the second transforms the B-spline control points to the Bézier control points; and the third generates the coordinates of a polygonal line from the Bézier control points. The processing speed for a TOKEN depends on the number of connected Cu²Es. Table 2 shows the processing

times required when ten TOKENs were used to transform B-spline knot points to polygonal lines.

6. Conclusion

We have successfully implemented a hardware architecture on the Cu²E LSI which combines the midpoint subdivision algorithm and error calculation to approximate a cubic Bézier or cubic B-spline curve to a polygonal line. The flatness error is programmable. This Cu²E LSI can transform the data which defines a curve. A high-speed operation of one million coordinates per second was achieved. This speed is sufficient to process the curve segments of 3 000-5 000 Kanji characters per second. It was proved that the Cu²E LSI was suitable for application in outline font design/operation systems. We are convinced that the Cu²E LSI is suitable for systems such as DTP and LBP.



Masayuki Okamoto

LSI Design Dept.
MOS Div.
FUJITSU LIMITED
Bachelor of Electronics Eng.
Nihon University 1986
Specializing in Graphics LSI Design



Mitsuru Yamauchi

LSI Design Dept.
MOS Div.
FUJITSU LIMITED
Niigata Technical High School 1974
Specializing in Graphics and Image
Processing VLSI

References

- 1) Adobe Systems Inc.: PostScript Language Reference Manual. 1st ed., Addison-Wesley, 1985, 321p.
- 2) Newman, W.M., and Sproull, R.F.: "21. Curves and Surfaces", Principles of Interactive Computer Graphics. Int. Student ed., New York, McGraw-Hill, 1981, pp. 309-331.
- 3) Yamaguchi, F.: Shape Processing Technology by Computer Display (II). (in Japanese), 1st ed., Tokyo, Nikkan Kogyo, 1982, pp. 69-87.
- 4) Sato, H., Sugiura, Y., and Fujita, M.: Speed Tunable Finite State Machine Compiler: ZEPHCADTM. *FUJITSU Sci. Tech. J.*, **24**, 4 (Special Issue on Semiconductors), pp. 464-468 (1988).
- 5) Suehiro, Y., Matsumura, N., and Goto, G.: Development of Sea of Gates. *FUJITSU Sci. Tech. J.*, **24**, 4 (Special Issue on Semiconductors), pp. 318-327 (1988).



Tomohiro Fukuoka

LSI Design Dept.
MOS Div.
FUJITSU VLSI LIMITED
Bachelor of Mathematic
Meijo University 1988
Specializing in Graphics LSI Design

Bi-Substituted Magnetic Garnet Film and its Application to an Optical Isolator

• Hidema Uchishiba • Masao Shibayama (*Manuscript received December 13, 1989*)

The growth and magneto-optical properties of thick epitaxial iron garnet films of composition $(\text{Tb}_{3-x}\text{Bi}_x)(\text{FeGaAl})_5\text{O}_{12}$ and its application to an optical isolator were investigated. The influence of Bi^{3+} ions on the magneto-optical properties was determined experimentally, and Faraday rotation coefficients of 2370 deg/cm at a wavelength (λ) of 1.31 μm and 1590 deg/cm at 1.55 μm were obtained with $x = 1.6$. For $\lambda = 1.55 \mu\text{m}$, the film thickness required to obtain a 45° Faraday rotation was 280 μm . Also, an optical isolator mounted on an anisotropically etched silicon substrate was proposed. An extinction ratio of about 40 dB and an insertion loss of less than 0.3 dB were obtained after temperature cycle testing.

1. Introduction

Bismuth-substituted iron garnet films with high magneto-optical effects have been used as optical isolators¹⁾ and magneto-optical switches²⁾. These isolators have been used to prevent reflected light from interfering with coherent laser sources. The requirements for these isolators are 1) small size, 2) low insertion loss, 3) high isolation, 4) easy coupling to other optical components (for example, optical fibers), 5) high tolerance to environmental influences, and 6) low cost. To satisfy these requirements, isolator materials (Faraday rotators) having excellent properties were developed, and a new isolator mounting technique was proposed.

This paper is divided into two main sections. One section discusses Faraday rotator materials and the other discusses the isolators.

2. Faraday rotator

The important characteristics of Faraday rotator materials are:

- 1) high Faraday rotation coefficient,
- 2) low optical absorption,
- 3) high extinction ratio,
- 4) low temperature dependence of Faraday

rotation, and

- 5) saturation at low magnetic field intensities.

It has been reported that Faraday rotation is increased by Bi concentration in Bi-substituted garnet films³⁾. The required thickness of Bi-substituted rare earth iron garnet films is 300-400 μm at a wavelength of 1.31-1.55 μm ¹⁾. However, these films have a tendency to form cracks and sometimes fracture during growth at thicknesses of 300-400 μm . In this study, we found that by carefully controlling the concentration of Tb and Bi ions, the required thickness of $(\text{TbBi})_3(\text{FeAlGa})_5\text{O}_{12}$ thick films could be decreased to 190 μm for $\lambda = 1.31 \mu\text{m}$ and to 280 μm for 1.55 μm .

This section describes the film growth, stability of super-saturated melts, bismuth substitution, and magneto-optical properties of the thick films.

2.1 Film growth and characterization of film properties

$(\text{TbBi})_3(\text{FeGaAl})_5\text{O}_{12}$ thick films were grown on 23 mm diameter (111)-oriented nonmagnetic garnet substrates with $\text{PbO-Bi}_2\text{O}_3\text{-B}_2\text{O}_3$ -based fluxes. The method used was liquid phase epitaxial (LPE) dipping⁴⁾. Because the bismuth

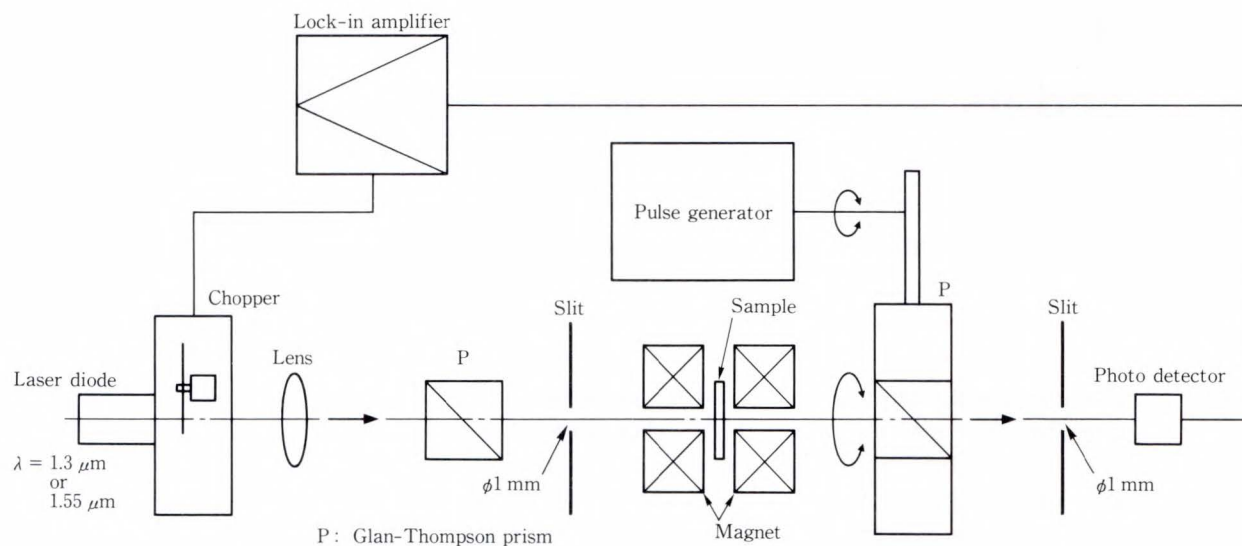


Fig. 1—Measurement method.

ion is large, bismuth substitution expands the garnet lattice. The Bi concentration increases with decreasing growth temperature. The lattice parameters of films were therefore controlled by controlling the growth temperature. The films were grown on substrates that most closely matched the lattice of the films, that is, $(\text{GdCa})_3(\text{MgZrGa})_5\text{O}_{12}$ or $\text{Nd}_3\text{Ga}_5\text{O}_{12}$. The difference between the lattice parameters of the thin film and the substrate, $\Delta a = a_s - a_f$, was measured using the X-ray double crystal method. (Where a_s and a_f are the lattice parameters of the substrate and film respectively.) The 1-2 μm thick films were grown so that both the film and substrate diffraction peaks were observed in the same scan.

From Bragg's equation:

$$\begin{aligned} 2d_s \sin \omega_s &= n\lambda_X, \\ 2d_f \sin \omega_f &= n\lambda_X, \end{aligned} \quad \dots \dots \dots (1)$$

where d_s and d_f are the lattice plane spacings, ω_s and ω_f are the Bragg angles of the substrate and film, and λ_X is the X-ray wavelength. It follows that

$$\frac{\Delta d}{d_s} = -(\cot \omega_s) \Delta \omega, \quad \dots \dots \dots (2)$$

where $\Delta d = d_s - d_f$ and $\Delta \omega = \omega_s - \omega_f$.

In addition, the data of the strained films are corrected via Poisson's ratio ν ; namely,

$$\Delta a = \frac{(1 - \nu)}{(1 + \nu)} \Delta d. \quad \dots \dots \dots (3)$$

Using Equations (2) and (3), the relative difference

ence $\frac{\Delta a}{a_s}$ is given by

$$\frac{\Delta a}{a_s} = -\frac{1 - \nu}{1 + \nu} (\cot \omega_s) \Delta \omega. \quad \dots (4)$$

Because the substrates are cubic crystals, a_s is equal to d_s .

The Δa was proportional to the growth temperature. It was therefore controlled by controlling the growth temperature.

Films were grown by the following method. After homogenization at 1030 °C, the temperature of the melt was lowered to the growth temperature (~720 °C). The substrate, clamped in a horizontal position by a holder, was held 10 mm above the melt surface for about 20 min. It was then placed on the melt surface. The thin films were grown over 5 min to a thickness of 1-2 μm . The thick films were grown over 20-35 h to a thickness of 200-400 μm .

The film compositions were determined by electron probe microanalysis (EPMA). The magneto-optical properties were measured in the normal transmission configuration with Glan-Thompson prisms as polarizers. Monochromatized light beams from laser diodes (1.31 μm and 1.55 μm wavelengths) were used as the light source. The measurement method is shown in Fig. 1.

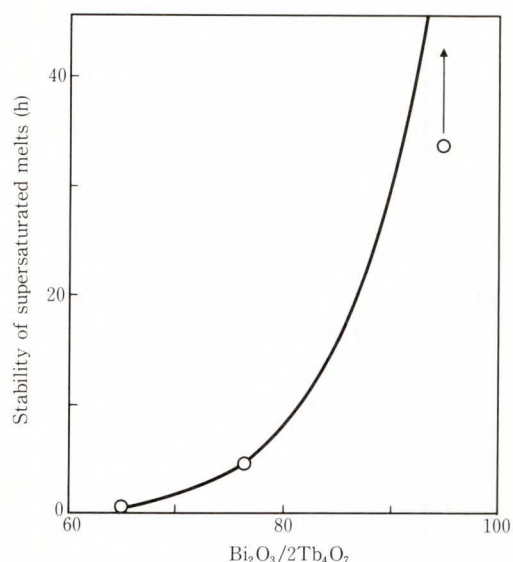


Fig. 2— $\text{Bi}_2\text{O}_3/2\text{Tb}_4\text{O}_7$ dependence of stability of supersaturated melts.

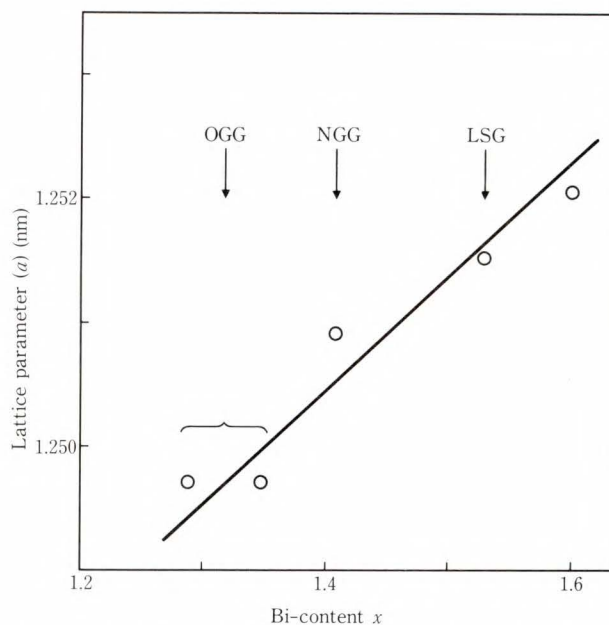


Fig. 3—Lattice parameters (a) vs. Bi-contents (x).

Table 1 Growth conditions and properties of $(\text{TbBi})_3(\text{FeAlGa})_5\text{O}_{12}$ thick films grown on OGG

Sample No.	#1	#2
Growth temperature ($^{\circ}\text{C}$)	755.3	757.9
Growth time (h)	30	30
Growth rate ($\mu\text{m}/\text{min}$)	0.25	0.27
θ_F ($\lambda = 1.31 \mu\text{m}$) (deg/cm)	1 850	1 980
Magnetic field saturation (A/m)	2.79×10^4	2.63×10^4

2.2 Stability of the supersaturated melt

Solutions of garnet components in the $\text{PbO-Bi}_2\text{O}_3\text{-B}_2\text{O}_3$ -fluxes are readily supersaturated with respect to the garnet phase without spontaneous nucleation. This makes it possible to grow thick garnet films by the LPE dipping method using these solvents. The decrease in supersaturation causes a decrease in growth rate and possibly changes the film composition.

Figure 2 shows the stability of supersaturation as a function of the $\text{Bi}_2\text{O}_3/2\text{Tb}_4\text{O}_7$ molar ratio in the melts. The stability of supersaturation was defined as the time at which spontaneous nucleation occurs after the substrate contacts the melt surface. The stability of the melts was proportional to the $\text{Bi}_2\text{O}_3/2\text{Tb}_4\text{O}_7$ concentration and was more than 35 h for a $\text{Bi}_2\text{O}_3/2\text{Tb}_4\text{O}_7$ of 90. A $470 \mu\text{m}$ thick

$(\text{TbBi})_3(\text{FeGaAl})_5\text{O}_{12}$ film was obtained on a $(\text{GdCa})_3(\text{MgZrGa})_5\text{O}_{12}$ (OGG) substrate after dipping for 30 h at 755°C . Typical growth conditions and properties of the thick garnet films are summarized in Table 1.

2.3 Faraday rotation

Films of $(\text{Tb}_{3-x}\text{Bi}_x)(\text{FeGaAl})_5\text{O}_{12}$ were grown on substrates that most closely matched the lattice of the films, that is, $(\text{GdCa})_3(\text{MgZrGa})_5\text{O}_{12}$ (OGG) ($a = 1.2497 \text{ nm}$), $\text{Nd}_3\text{Ga}_5\text{O}_{12}$ (NGG) ($a = 1.2509 \text{ nm}$) and $(\text{GdCa})_3(\text{MgZrGa})_5\text{O}_{12}$ (LSG) ($a = 1.2515 \text{ nm}$ to 1.2520 nm). The Bi-content and lattice parameters of the films were proportional to the $\text{Bi}_2\text{O}_3/2\text{Tb}_4\text{O}_7$ concentration and lattice constant of the substrates, and were inversely proportional to the growth temperature. The iron contents of the films were almost constant.

Figure 3 shows the lattice parameter a as a function of the Bi-contents x for $(\text{Tb}_{3-x}\text{Bi}_x)(\text{FeAlGa})_5\text{O}_{12}$ films. The substrates used are shown in Fig. 3. Table 2 shows the magneto-optical properties of films grown on various substrates from melts with various $\text{Bi}_2\text{O}_3/2\text{Tb}_4\text{O}_7$ concentrations. Figure 4 shows the Faraday rotation coefficients θ_F at $1.31 \mu\text{m}$ and $1.55 \mu\text{m}$ as a function of the Bi contents x for $(\text{Tb}_{3-x}\text{Bi}_x)(\text{FeGaAl})_5\text{O}_{12}$ films. A θ_F

Table 2 Magneto-optical properties of $(\text{TbBi})_3(\text{FeAlGa})_5\text{O}_{12}$ thick films

Sample No.	#3		#4		#5	
Wavelength (μm)	1.31	1.55	1.31	1.55	1.31	1.55
θ_F (deg/cm)	1 820	1 230	2 040	1 360	2 370	1 590
Thickness for 45° rotator (μm)	247	365	220	330	190	280
$\text{Bi}_2\text{O}_3/2\text{Tb}_4\text{O}_7$	95.4		120		120	
Substrate	OGG		NGG		LSG	
{ a (nm) }	(1.249 7)		(1.250 9)		(1.251 9)	

#3: $(\text{Tb}_{1.65}\text{Bi}_{1.35})(\text{FeGaAl})_5\text{O}_{12}$
 #4: $(\text{Tb}_{1.59}\text{Bi}_{1.41})(\text{FeGaAl})_5\text{O}_{12}$
 #5: $(\text{Tb}_{1.47}\text{Bi}_{1.53})(\text{FeGaAl})_5\text{O}_{12}$

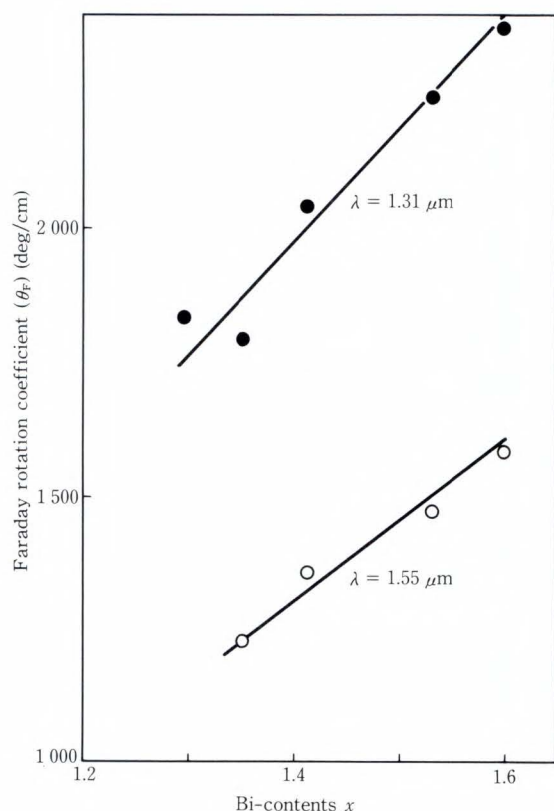


Fig. 4—Faraday rotation coefficients (θ_F) vs. Bi-contents (x).

as high as 2 370 deg/cm at 1.31 μm and 1 590 deg/cm at 1.55 μm were obtained with $x = 1.6$. θ_F depends mainly on the Bi concentration, that is, θ_F increases with an increasing concentration of Bi^{3+} ions³⁾. Figure 5 combines the results shown in Figs. 3 and 4. It shows the Faraday rotation coefficients at wavelengths of 1.31 μm and 1.55 μm as a function of the lattice parameters. Even for $\lambda = 1.55 \mu\text{m}$, the

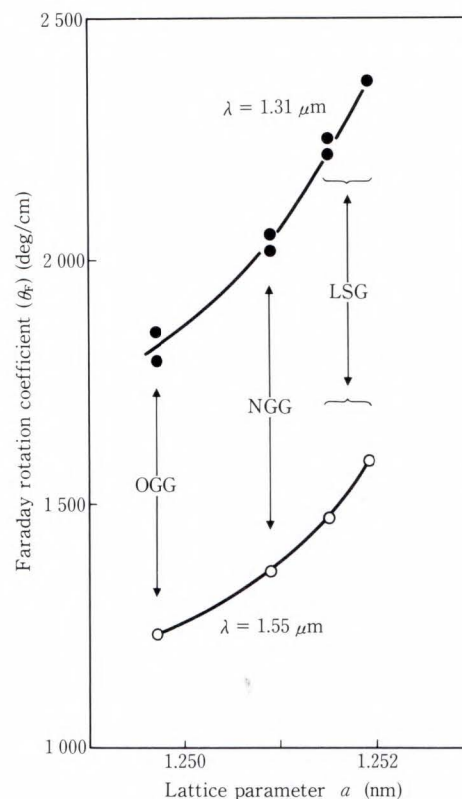


Fig. 5—Faraday rotation coefficients (θ_F) vs. lattice parameters (a) at $\lambda = 1.31 \mu\text{m}$ and $1.55 \mu\text{m}$.

Table 3 Properties of $(\text{TbBi})_3(\text{FeAlGa})_5\text{O}_{12}$ thick films

Sample No.	#5		#6	
Wavelength (μm)	1.31	1.55	1.31	1.55
θ_F (deg/cm)	2 370	1 590	2 060	1 380
Thickness for 45° rotator (μm)	190	280	220	330
Insertion loss (dB)	0.12	0.12	0.25	0.26
Extinction ratio (dB)	40	39	42	39
Magnetic field for saturation (A/m)	3.11×10^4	3.50×10^4	2.79×10^4	3.34×10^4
Temperature coefficient (deg/ $^\circ\text{C}$)	-0.07	-0.07	-0.07	-0.07
Substrate	LSG { 1.251 9 }		NGG { 1.250 9 }	
{ a (nm) }	LSG { 1.251 9 }		NGG { 1.250 9 }	

film thickness required to obtain a 45° Faraday rotation was only 280 μm . The formation of cracks was appreciably reduced by decreasing the film thickness.

Typical properties of the film in the $(\text{TbBi})_3(\text{FeGaAl})_5\text{O}_{12}$ system are summarized in Table 3.

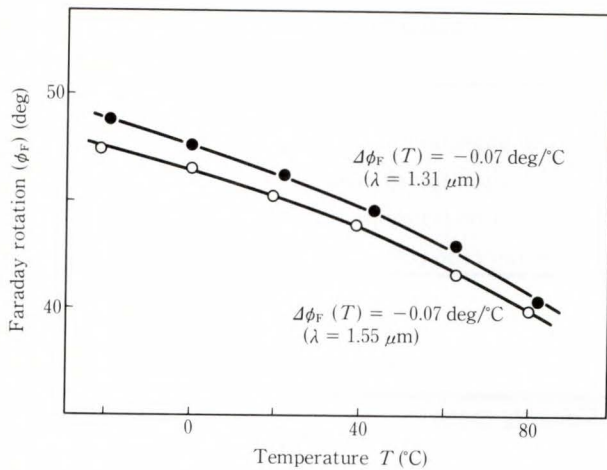


Fig. 6—Temperature dependence of Faraday rotation (ϕ_F) at $\lambda = 1.31 \mu\text{m}$ and $1.55 \mu\text{m}$ for sample #6.

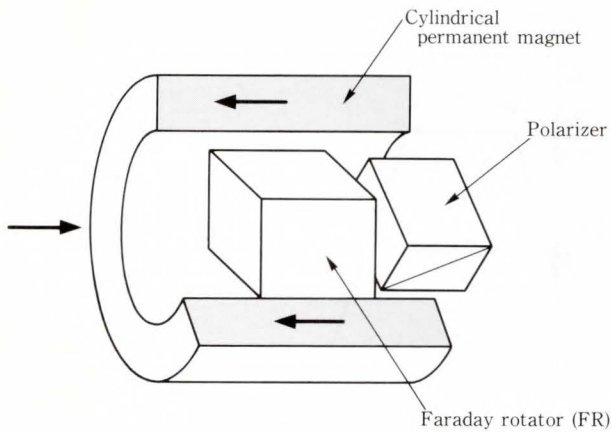


Fig. 7—Cut-away diagram of the optical isolator.

The temperature dependence of the Faraday rotation ϕ_F at $\lambda = 1.31 \mu\text{m}$ and $1.55 \mu\text{m}$ for sample #6 of Table 3 is shown in Fig. 6. The temperature coefficient $\Delta\phi_F(T)$ of the Faraday rotation was $-0.07 \text{ deg}/^\circ\text{C}$,

where,

$$\Delta\phi_F(T) = \frac{\phi_F(50^\circ\text{C}) - \phi_F(0^\circ\text{C})}{50^\circ\text{C} - 0^\circ\text{C}} \quad (5)$$

3. Optical isolator

3.1 New mounting technique of optical isolators

A typical optical isolator for a Laser diode (LD) module using the Faraday effect is shown in Fig. 7. It consists of a polarizer, a Faraday rotator (FR), and a cylindrical permanent magnet. Bi-substituted garnet films grown by

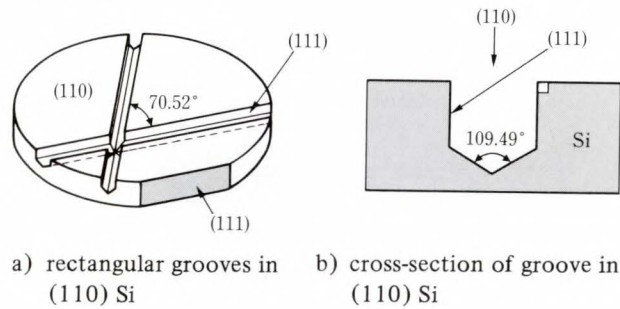


Fig. 8—Anisotropic etching of (110) Si.

the LPE method have recently been used for the FR. A polarization beam splitter (PBS) is used for the polarizer. The permanent magnet provides the saturation magnetic field for the FR.

One of the problems concerning this type of isolator is that the components are often very small and therefore difficult to optically align. To solve this problem, a new mounting technique in which the optical components are inserted in an anisotropically etched groove in silicon (Si) was devised.

In anisotropic etching of Si wafers, the crystallographic planes are etched at different rates to produce various shapes⁵. A high-precision rectangular groove in (110) Si substrate can be made using photolithography (see Fig. 8). The components of the optical isolator were inserted in these grooves. It then became easy to optically align the components.

The rectangular groove is made by anisotropic etching of an Si wafer. Thermally grown SiO_2 is used as an etch mask, and $0.4 \mu\text{m}$ thick SiO_2 films were grown at 1100°C in wet O_2 . The Si wafer was etched using anisotropic etching equipment⁶. The etchant used was ethylene diamine pyrocatechol and water (EDA) which yielded a higher etch ratio (Si/SiO_2).

A rectangular groove in an Si wafer is illustrated in Fig. 9. The groove is $330 \mu\text{m}$ deep and was etched over 9.5 h at 110°C . The etching rates of the (110) plane and (111) plane were about $0.57 \mu\text{m}/\text{min}$ and $0.03 \mu\text{m}/\text{min}$ respectively. The angle of the (111) and $(\bar{1}\bar{1}\bar{1})$ planes to the (110) plane was almost 90° (the deviation was 0.3°).

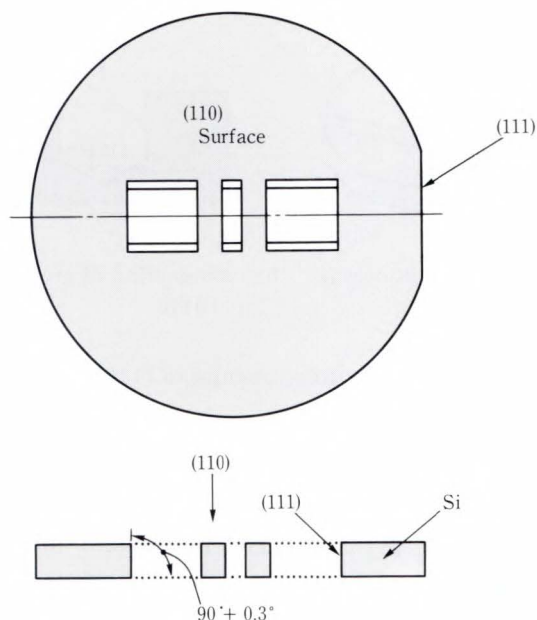


Fig. 9—Etching of the optical isolator.

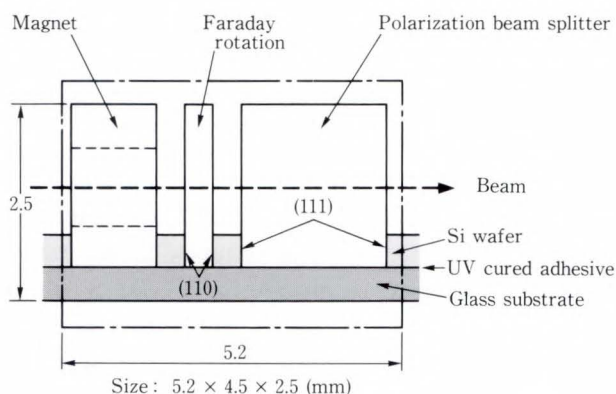


Fig. 10—Structure of optical isolator.

3.2 Assembly of optical isolator components

Figure 10 illustrates the structure of the optical isolator on etched Si. The isolator was 5.2 × 4.5 × 2.5 mm. The Si wafer was fixed to 500 μm thick Pyrex glass by UV cured adhesive. There are two reasons why this method was used. One reason is that the thermal expansion of Si (2.4 × 10⁻⁶ deg⁻¹) is nearly equal to that of Pyrex glass (3.0-3.6 × 10⁻⁶ deg⁻¹). The other is that Pyrex glass passes ultraviolet rays. The permanent magnet is cylindrical and made of Sm-Co. This magnet creates a magnetic field in the saturation magnetic field ($H_s = 2.79 \times 10^4$ A/m) of the

Table 4 Optical properties of the polarization beam splitter

Wavelength (μm)	1.26-1.35
Incident angle (deg)	45-58
P polarization transparent (%)	99
S polarization transparent (%)	0.02
Extinction ratio (dB)	> 45

Table 5 UV cure adhesive

Viscosity (poise)	35-50
Cured state	Wavelength : 350-380 nm < 30 min
Temperature range	-54 °C to +100 °C

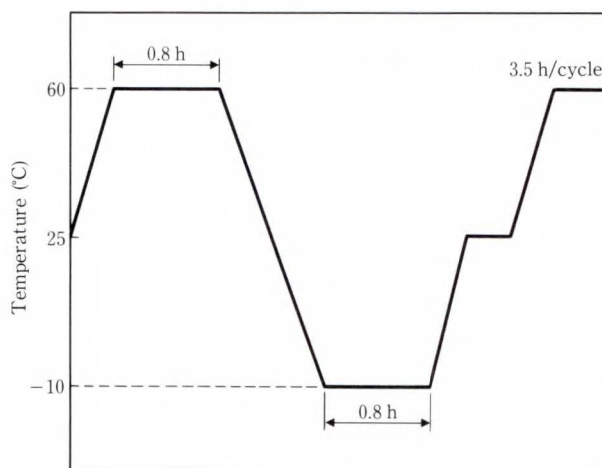


Fig. 11—Temperature cycle test.

FR. The PBS is a multilayer dielectric of TiO₂ and SiO₂ films.

Table 4 shows the optical properties of the PBS.

The isolator components were fixed in the etched groove of the Si substrate using UV cured adhesive (see Table 5). This adhesive is a polymer of acrylic resins and is cured by ultraviolet irradiation at room temperature.

3.3 Properties of the optical isolator

Because it was extremely difficult to measure the isolation of the optical isolator shown in Fig. 10, the extinction ratio was

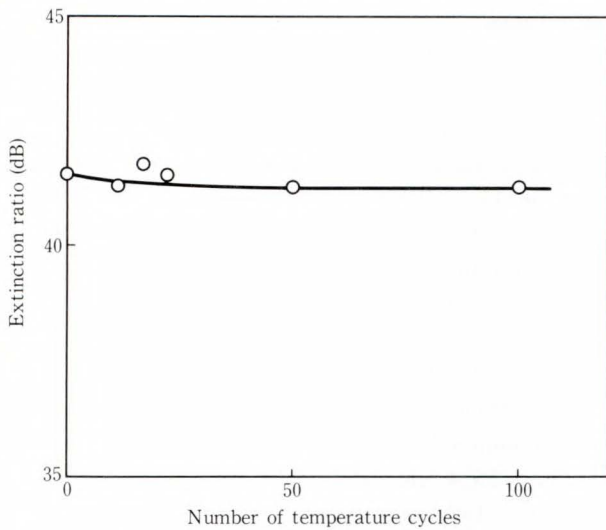
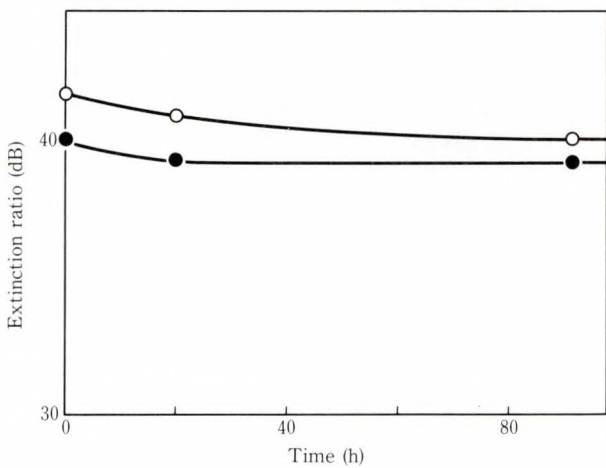
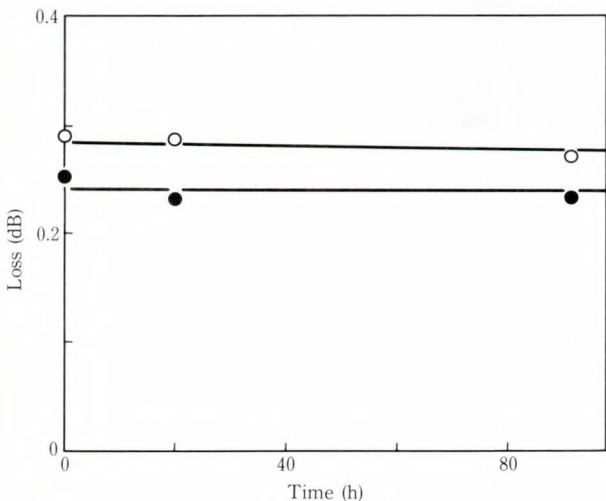


Fig. 12—Extinction ratio as a function of temperature.



a) Extinction ratio



b) Insertion loss

Fig. 13—Extinction ratio and insertion loss as a function of time at 80 °C.

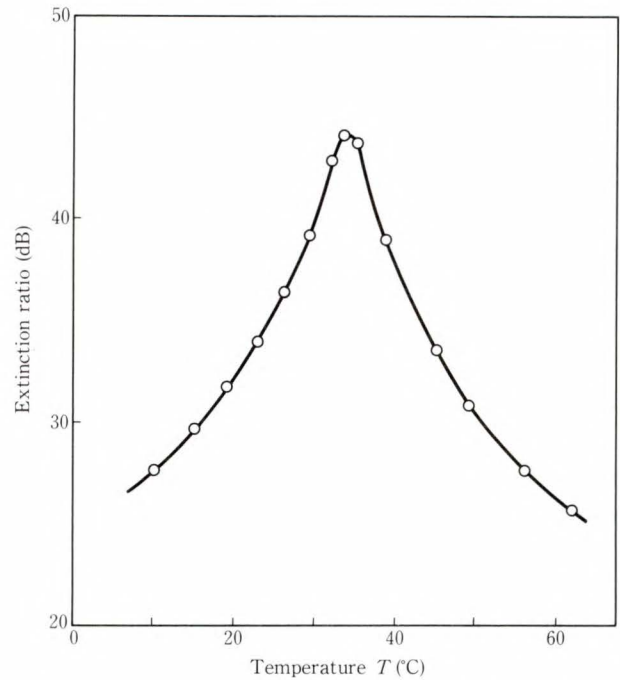


Fig. 14—Temperature properties of extinction ratio.

measured instead. The measurement method is shown in Fig. 1. The extinction ratio of this isolator was more than 40 dB.

The optical properties (insertion loss and extinction ratio) were measured after temperature cycle testing. Figure 11 shows the temperature cycle that was used. One cycle took 3.5 h and the temperature was varied between -10°C and $+60^{\circ}\text{C}$. Figure 12 shows the extinction ratio measured at room temperature as a function of the number of temperature cycles the device was subjected to. There was no remarkable degradation of the extinction ratio over the first 100 cycles. After 100 cycles, the extinction ratio was still greater than 40 dB. Figure 13 shows the extinction ratio and insertion loss measured at room temperature as a function of time at 80°C for two samples. The extinction ratio decreased less than 1 dB and over an 86 h period was almost a constant 40 dB. There was no remarkable degradation of insertion loss (insertion loss was less than 0.3 dB over an 86 period).

Figure 14 shows the extinction ratio as a function of temperature. An extinction ratio of more than 25 dB was obtained over the range of 10°C to 60°C .

4. Conclusion

The growth and magneto-optical properties of thick epitaxial iron garnet films of composition $(\text{TbBi})_3(\text{FeGaAl})_5\text{O}_{12}$ and the use of these films in an optical isolator were investigated.

θ_F at $\lambda = 1.31 \mu\text{m}$ and $1.55 \mu\text{m}$ were 2370 deg/cm and 1590 deg/cm respectively. The magnetic field required for saturation was $3.11 \times 10^4 \text{ A/m}$ and $3.50 \times 10^4 \text{ A/m}$ respectively. At $\lambda = 1.55 \mu\text{m}$, the film thickness required to obtain a 45° Faraday rotation was only $280 \mu\text{m}$. The extinction ratio at both these wavelengths was 42 dB , and the insertion loss was 0.20 dB and 0.16 dB respectively. The temperature coefficient of the Faraday rotation was $-0.07 \text{ deg/}^\circ\text{C}$.

The optical isolator components were positioned in a rectangular groove etched into an Si wafer and were fixed using UV cured adhesive. An extinction ratio of about 40 dB and an insertion loss of 0.3 dB were obtained after temperature cycling. The extinction ratio of the optical isolator between 10°C and 60°C was greater than 25 dB .

References

- 1) Hibiya, T., Ishikawa, T., and Ohta, Y.: Growth and Characterizations of $300\text{-}\mu\text{m}$ Thick Bi-Substituted Gadolinium Iron Garnet Films for an Optical Isolator. *IEEE Trans. Magnetics*, **MAG-22**, 1, pp. 11-13 (1986).
- 2) Hibiya, T.: Effects of Melt $\text{PbO/B}_2\text{O}_3$ Molar Ratio on Morphological Change for $\{111\}$ Thick Garnet Films Grown by Liquid Phase Epitaxy. *J. Cryst. Growth*, **64**, 2, pp. 400-402 (1983).
- 3) Hansen, P., Witter, K., and Tolksdorf, W.: Magnetic and Magneto-Optic Properties of Bismuth-and Aluminum-Substituted Iron Garnet Films. *J. Appl. Phys.*, **55**, 4, pp. 1052-1061 (1984).
- 4) Klages, C-P., and Tolksdorf, W.: LPE Growth of Bismuth Substituted Gadolinium Iron Garnet Layers: Systematization of Experimental Results. *J. Cryst. Growth*, **64**, 2, pp. 275-284 (1983).
- 5) Bassous, E.: Fabrication of Novel Three-Dimensional Microstructure by the Anisotropic Etching of (100) and (110) Silicon. *IEEE Trans. Electron Devices*, **ED-25**, 10, pp. 1178-1185 (1978).
- 6) Reisman, A., Berkenblit, M., Chan, S.A., Kaufman, F.B., and Green, D.C.: The Controlled Etching of Silicon in Catalyzed Ethylenediamine-Pyrocatechol-Water Solutions. *J. Electrochem. Soc.*, **126**, 8, pp. 1408-1415 (1979).



Hidema Uchishiba

Components Technology Laboratory
FUJITSU LABORATORIES, ATSUGI
Bachelor of Physics
Gakushuin University 1965
Dr. of Physics
Gakushuin University 1972
Specializing in Magneto-Optical
Materials and Crystal Growth



Masao Shibayama

Components Technology Laboratory
FUJITSU LABORATORIES, ATSUGI
Bachelor of Electronics
Nihon University 1982
Master of Electronics
Nihon University 1984
Specializing in Magneto-Optical
Materials and Optical Isolators

Magnetic Circuit Yoke by Metal Injection Molding

• Yoshihiko Seyama • Tsutomu Iikawa (Manuscript received December 4, 1989)

Metal injection molding has attracted substantial attention in the powder metallurgy field because of the technology's promise for manufacturing parts with complex shapes. An attempt has been made to apply the metal injection molding technology to the production of a magnetic circuit yoke. The yoke has a complex shape and is made from a soft magnetic alloy, Fe-50%Co, which has low workability due to its hardness and brittleness. In this paper, the optimum starting powders and plastic binders, and the mixing which most affects metal injection molding were investigated. As a result, an Fe-50%Co alloy magnetic circuit yoke with a complex shape was obtained having good magnetic properties.

1. Introduction

Metal injection molding (MIM) is a marriage of conventional sintering technology and thermoplastic injection molding. This process has attracted substantial attention in the powder metallurgy field because of the technology's promise for manufacturing parts with complex shapes^{1),2)}.

The authors have developed the soft magnetic sintered Fe-50%Co alloy, which has a low workability due to its hardness and brittleness, to produce near net shaped magnetic circuit yoke³⁾. This sintered alloy has been applied to an electromagnetic part in a printing head of a 24-wire dot-matrix printer.

In conventional sintering, however, it is difficult to make parts with complex shapes because the flexibility is limited along one axis. This is because a press is used to compact the powders.

The authors tried to apply the MIM process to make an Fe-50%Co magnetic circuit yoke with a complex shape. The authors identified the optimum starting powders, plastic binders, and the mixing method. As a result, an Fe-50%Co magnetic circuit yoke with a complex shape was obtained having good magnetic prop-

erties.

2. Metal injection molding

Figure 1 shows the flow of the MIM process. The starting metal powder is mixed with a lot of plastic binder at a ratio of 40-45 vol%. The mixture can be easily injected into mold cavities to form precious components under moderate temperature and pressure as with conventional thermoplastics fabrication. This is because the metal powders are embedded in the viscous and malleable plastic binder matrix. Any parts with a complex shape can be formed if the mold cavities are machinable. To obtain the metal part, the plastic binder is extracted by low-temperature heat treatment to break down and vaporize. This process is known as debinding. The debound bodies are then sintered to obtain metal parts with high density.

In this process, however, it is difficult to select the starting powders and plastic binders which determine the molding and debinding ability through the thermal fluidity of the mixture.

The generally used metal powder has an average particle size of less than $10 \mu\text{m}^4)$. The mixture using this powder has higher fluidity

than that using large particles in conventional sintering, when the amount of binder in each powder is the same.

Various plastics are used as binders. These are selected for their thermal fluidity and decomposed properties. The amount of plastic binder most affects the molding and debinding ability. The mixture using a lot of plastic binder shows a high thermal fluidity and is easily molded. The molded body using this mixture, however, breaks down during debinding. Therefore, a mixture with a high thermal fluidity with a

small amount of binder is necessary. For the mixture to satisfy this demand, a suitable mixing method is also necessary.

The authors concentrated on the relationship between the characteristics of the starting powder and the molding ability. The effects of the amount of plastic binder and the mixing method on the mold ability were also studied.

3. Experimental procedure

Table 1 lists the characteristics of the starting powders. Figure 2 shows the distribution of the particle size of these powders. Powders with an average particle size of about 20 μm were used. These powders are easily obtained because they are used in conventional sintering technology. Powder D, however, was mixed from three powders with an average particle size of 5, 20, and 40 μm .

Polyethylene (PE) and Polymethylmethacrylate (PMMA) were selected as the binders because they do not dissolve each other, and because less carbon remains after debinding. Carbon adversely affects the magnetic properties of Fe-50%Co alloy.

To study the optimum amount of binders, the starting powders and two plastic binders, PE and PMMA, were mixed in the range from

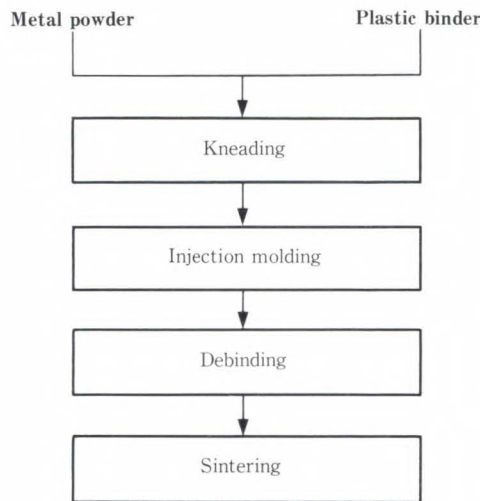
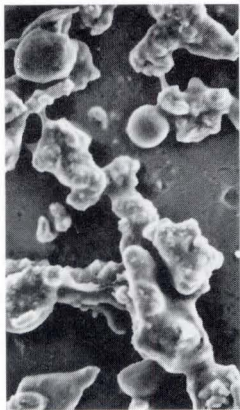
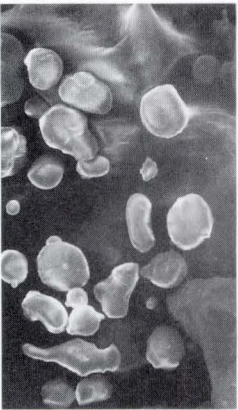
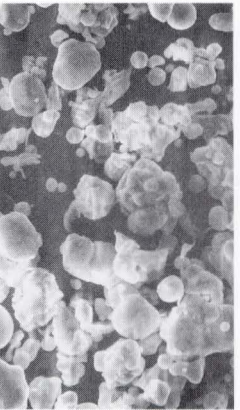
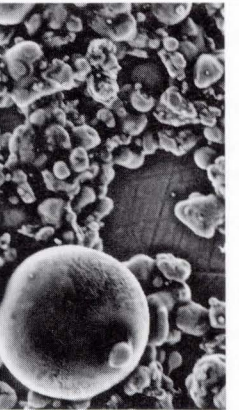


Fig. 1—Metal injection molding process.

Table 1. Properties of starting powders

Powder	A	B	C	D
Specific surface area (m ² /g)	5.84	3.01	2.85	2.84
SEM photographs				
Tap density (%)	39.8	42.0	46.9	44.7

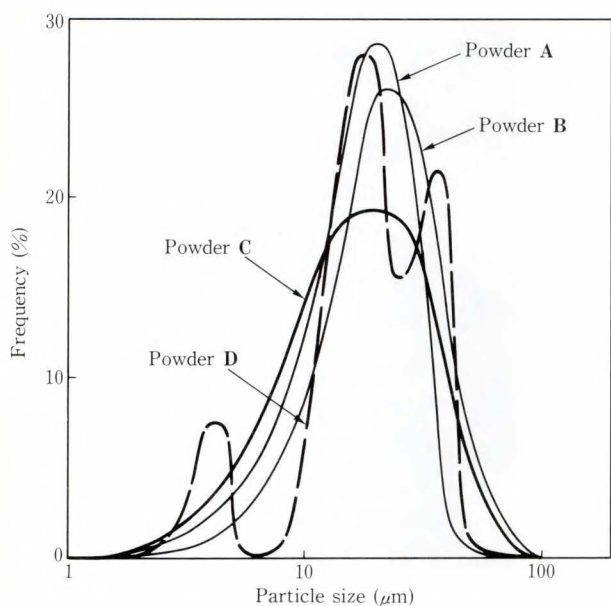


Fig. 2—Distribution of particle size of starting powders.

Table 2. Mixing method

Method	Process		
	Material	Kneading	
		First	Second
A	Metal powder	Mixture	
	PMMA		
	PE		
B	Metal powder	Premixture	Mixture
	PMMA		
	PE		

35 vol% to 45 vol% using a kneader.

The mixing methods were varied as shown in Table 2. In method A, the raw materials were mixed to lump together at a relatively high temperature. In method B, PE was mixed at relatively low temperature after the PMMA was mixed with the metal powders at high temperature.

These mixtures were injected into the mold cavity shown in Fig. 3. After molding, the molded bodies were debound and sintered.

The torque of the mixtures was measured as a standard of thermal fluidity. Cross-sections of the mixtures and molded bodies were observed by using an optical microscope.

The densities of the sintered bodies were

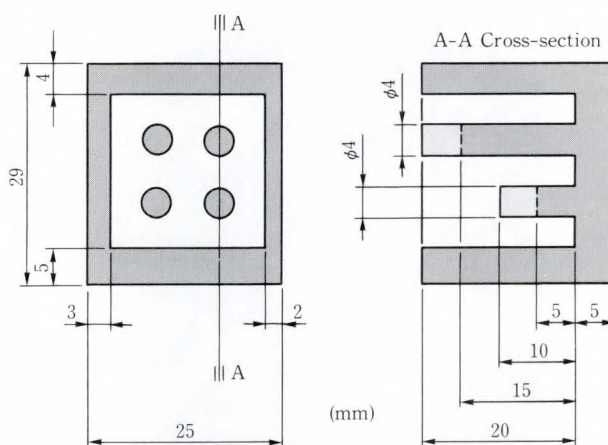


Fig. 3—Mold cavities.

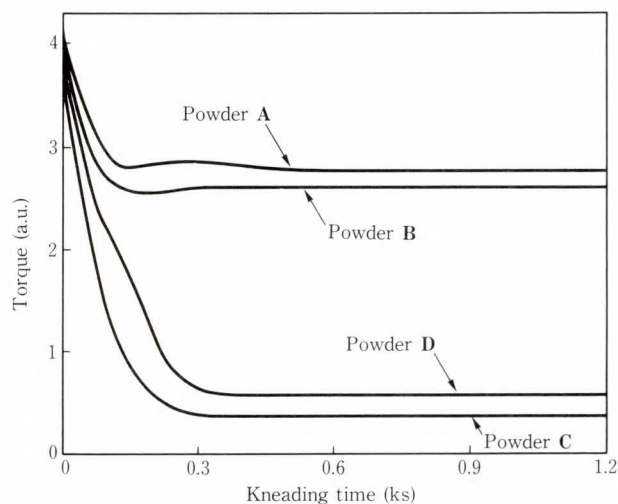


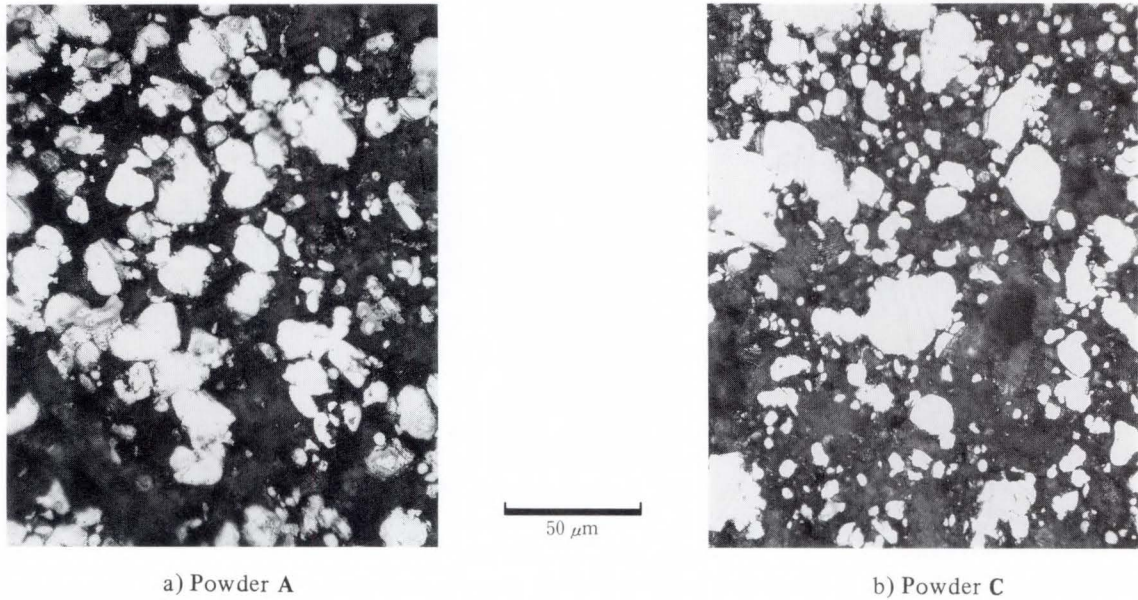
Fig. 4—Torque changes in the mixtures.

measured using Archimedes' method. The magnetic properties were measured in a magnetic field of 4 kA/m using the ring samples which were cut down from the sintered bodies.

4. Results and Discussion

4.1 Effect of starting powder

Figure 4 shows the torques of the mixtures used as the various starting powders. In this case, the amount of plastic binder was 45 vol%, and method A shown in Table 2 was used to make mixtures. In all the mixtures, the torque became constant after mixing for 0.3 ks. The torque of the mixture using powders A and B are, however, four times higher than that of the mixture using powders C and D.



a) Powder A

b) Powder C

Fig. 5—Cross-sections of the mixtures.

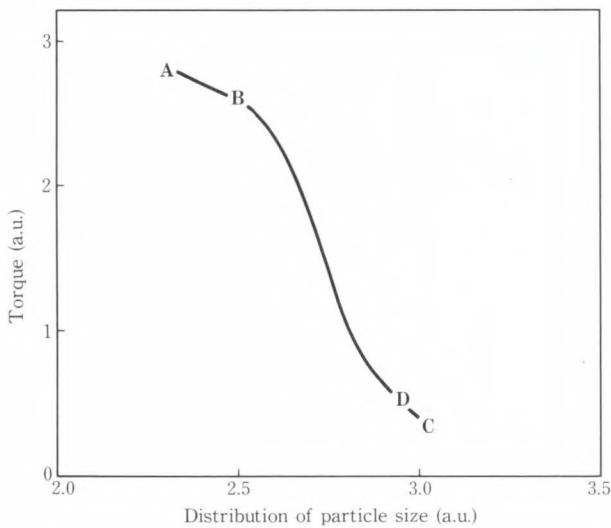
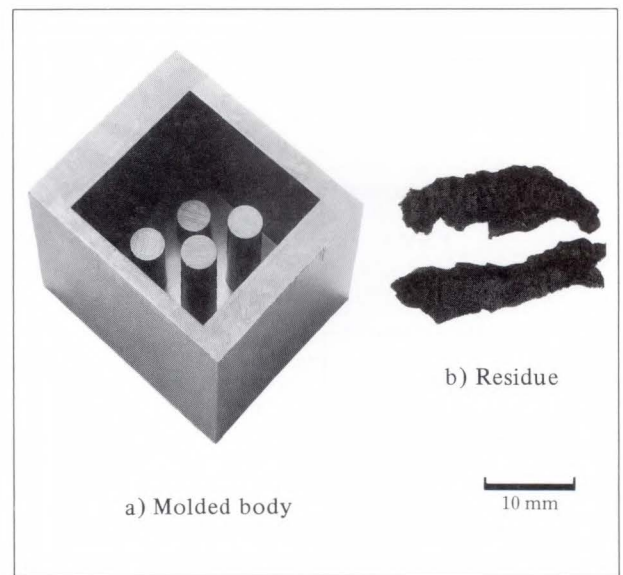


Fig. 6—Relationship between the distribution of particle sizes and torque of the mixtures.

Figure 5 shows the cross-sections of the mixtures using powders A and C. In powder A, particles of about $20\ \mu\text{m}$ agglomerate together. In powder C, the particles disperse homogeneously. The difference of the torque in these two mixtures is due to this agglomeration. The authors propose the following explanation. When the particles accumulate, the powder with narrow distribution A has more porosity than that with wide distribution C. And the binder is wasted as it is used to fill the porosity.



a) Molded body

b) Residue

Fig. 7—Molding body of powder C and the residue in the injection machine for powder A.

Therefore, the distance between each particle in the mixture used for powder A is narrower because the effective amount of binder is reduced. This is why the powder with a narrow distribution is prone to agglomeration.

Figure 6 shows the relationship between the distribution of the particle size and the torque of the mixtures. The torque of the mixtures decreases with an increase in the distribution of the particle size. The result of powder D shows

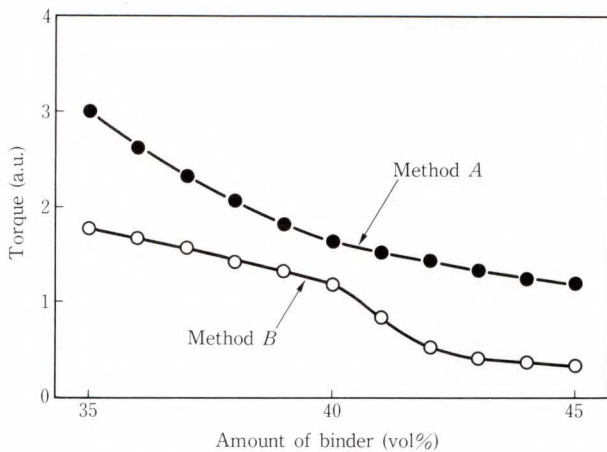


Fig. 8—Relationship between the amount of binder and torque of the mixtures prepared by methods A and B.

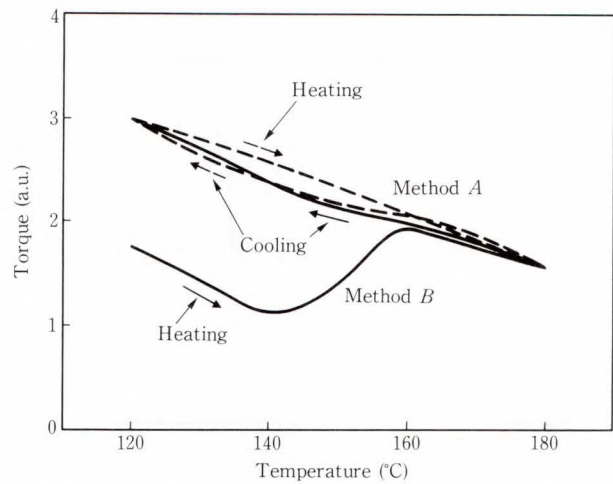


Fig. 10—Torque change during heating and cooling.

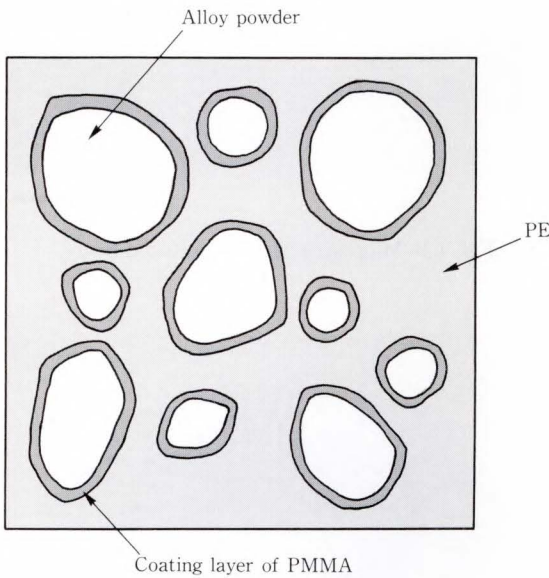


Fig. 9—Model for mixtures.

that the mixed powders with different particle sizes also have higher molding ability.

The mixture for powders A and B cannot be molded. This is because the particles in these mixtures agglomerate under the injection pressure and remain in the injection machine. The mixture for powders C and D can be molded as shown in Fig. 7 because they have low torque.

The distribution of the particle size varied at the atomizing lots. However, the distribution of the particle size in the mixed powder can be controlled to a constant value. From these results, mixed powder D was selected as the optimum starting powder.

4.2 Binder content and mixing method

Figure 8 shows the relationship between the amount of binder and torque of the mixture prepared by the two methods shown in Table 2 using powder D. The torque of the mixture prepared by method A is lower than that prepared by method B in all the amount of binder. Furthermore, the torque of the mixture prepared by method B is low even if the amount of binder is 35 vol%, which is about 10 vol% less than that generally used in MIM.

The reason for this is thought to be as follows. As shown in Fig. 9, method B fabricates the coating layer of PMMA around the particles which acts as a sliding layer between the particles. Because this layer prevents the agglomeration of particles, the mixture can maintain high thermal fluidity under the injection pressure even if the amount of binder is 35 vol%. However, method A fabricates a homogeneous mixture of two binders. Because the agglomeration of the particles increases when the amount of binder decreases, the thermal fluidity of the mixture decreases.

To prove that a coating layer was formed, the torque change during heating and cooling was measured. As shown in Fig. 10, the torque of the mixture prepared by method A decreases proportionally during heating as well as increasing proportionally during cooling, and traces almost the same curve during both heating and cooling. The torque of the mixture prepared by

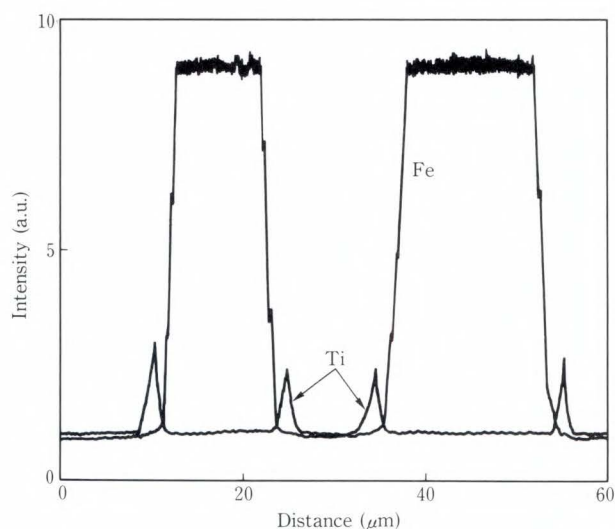


Fig. 11—EPMA analysis of the mixture prepared by method B.

method B is three times lower at 120 °C and decreases until the temperature reaches 140 °C. However, it increases as the temperature exceeds 140 °C and shows the same value as that prepared by method A. Moreover, it increases in the same way as that in method B with cooling.

This result shows that the structure of the mixture prepared by method B changes at 140 °C, that the coating layer of PMMA begins to soften at 140 °C, and that PMMA then disperses in the PE as the temperature increases. Finally, the structure of the mixture becomes homogeneous like the mixture prepared by method A. This result suggests that the coating layer of PMMA is formed by method B.

Using EPMA, the authors analyzed the mixtures by method B. In this case, PMMA was added to organic titanium because organic materials cannot be analyzed by EPMA. As shown in Fig. 11, titanium peaks are observed around the particles. This means that the coating layer of PMMA is formed around the particles. This result proves that the coating layers are formed by method B.

In debinding, the molded bodies break down when the binders begin to soften and flow at once. However, no problem occurs with the mixture prepared by method B when the amount of binder is 35 vol%. This indicates why the amount of binder is less and why the binder

Table 3. Properties of sintered body fabricated by metal injection molding

Relative density (%)	Magnetic properties		
	B _{4k} (T)	μ _m (mH/m)	H _c (A/m)
92.4	2.05	4.1	180

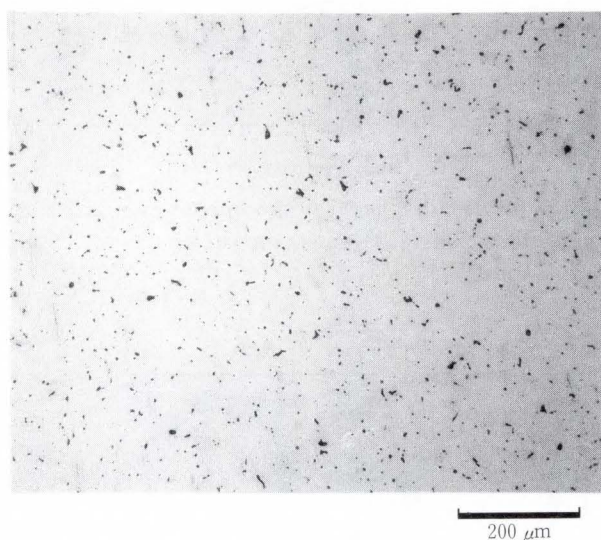


Fig. 12—Microstructure of sintered body.

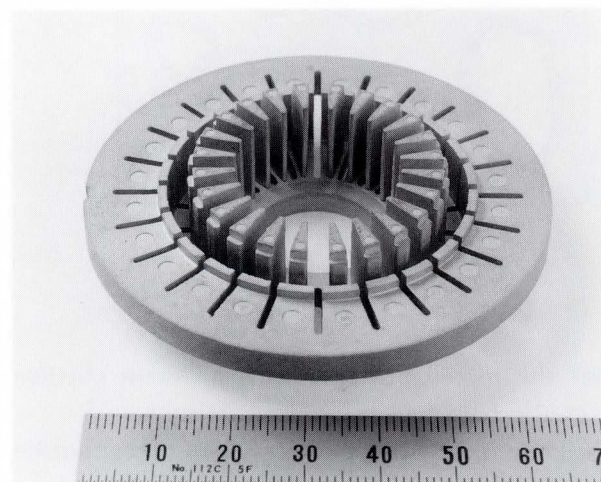


Fig. 13—Magnetic circuit yoke made by metal injection molding.

thermally decomposes step by step due to the presence of two layers and the difference in softening points in PE and PMMA.

The authors sintered these debound bodies. Table 3 shows the relative density and the magnetic properties of Fe-50%Co alloy. The microstructure is shown in Fig. 12. These prop-

erties are sufficient to apply the magnetic circuit yokes for various OA equipment.

5. Application

This MIM technology was applied to an Fe-50%Co magnetic circuit yoke with a complex shape in a printing head of a 24-wire dot-matrix printer. The trial product, which has 24 inner cores, is shown in Fig. 13.

6. Conclusion

The authors applied metal injection molding to a magnetic circuit yoke with a complex shape made from Fe-50%Co alloy. This alloy had few applications due to its low workability, although it has the highest magnetization of all metals.

The authors identified the optimum starting powder and plastic binder. And the mixing method was optimized to obtain a high thermal fluidity even if the amount of binder was 35 vol%. As a result, an Fe-50%Co alloy magnetic circuit yoke with an extremely complex shape

was obtained which had sufficient magnetic properties to be applied to the new OA equipment.

This technology is applicable to ceramics and to composite materials which are less practical due to low workability.

References

- 1) Billiet, R.: Net-shaped full-density P/M parts by injection molding. *Int J. Powder Met. Powder Tech.*, **21**, 2, pp. 112-118 (1985).
- 2) Merhar, J.R.: Overview of metal injection molding. *Proc. Int. Business High-Tech Conf. Adv. Mater. Injec. Mold. Appl.*, 1988, pp. 1-20.
- 3) Yamagishi, W., and Iikawa, T.: Fe-50%Co Sintered Alloy for Magnetic Circuit Yoke. *FUJITSU Sci. Tech. J.*, **24**, 3, pp. 254-261 (1988).
- 4) Beuers, J., and Poniatowski, M.: Metal injection molding – a progressive shaping process requires sophisticated sintering techniques. *Pro. Int. Inst. Sci. Sint.*, (Sintering 87), 1989, Elsevier Appl. Sci., England, pp. 230-236.



Yoshihiko Seyama

Inorganic Materials Laboratory
FUJITSU LABORATORIES, ATSUGI
Bachelor of Physics
Chiba University 1986
Specializing in Powder Metallurgical
Materials



Tsutomu Iikawa

Inorganic Materials Laboratory
FUJITSU LABORATORIES, ATSUGI
Bachelor of Metallurgical Eng.
Tohoku University 1971
Specializing in Powder Metallurgical
Materials

Bistable Laser Diode for Optical Signal Processing

• Tetsufumi Odagawa • Tatsuyuki Sanada • Shigenobu Yamakoshi

(Manuscript received December 4, 1989)

A bistable laser diode with a saturable absorber was studied for optical signal processing from two points of view. First, for fast operation using optical set and electrical reset signals, the carrier density change caused by the electrical reset was decreased by optimizing the bias voltage of the laser. As a result, fast flip-flop operation at a 2.5 Gbit/s repetition rate was achieved. Second, for all-optical signal processing which will be important for future optical systems, a new optical reset using gain quenching was proposed and confirmed. All-optical flip-flop operation is demonstrated.

1. Introduction

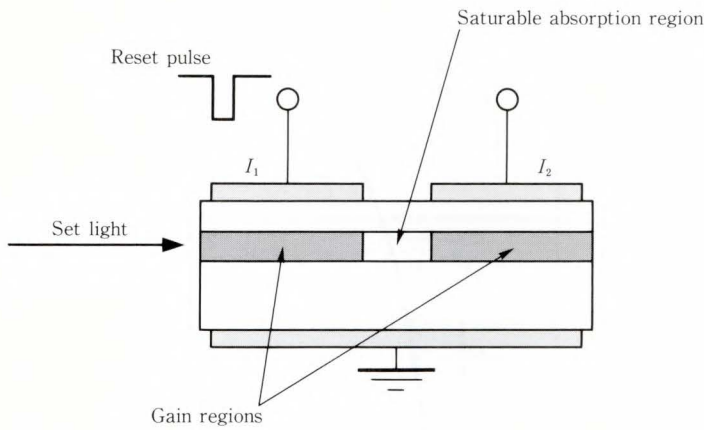
As photonic networks increase, optical signal processing such as optical signal switching is gaining attention because it can use a large bandwidth of light and does not need *O/E* or *E/O* conversion. In the construction of optical signal processing systems, optical bistable devices will play an important role in the logic and memory devices.

So far, many optical bistable devices have been researched, e.g. Fabry-Perot etalon with nonlinear materials¹⁾, Fabry-Perot laser amplifier²⁾, SEED³⁾, VSTEP⁴⁾, a bistable laser diode (BSLD) with saturable absorber⁵⁾⁻²¹⁾. Among these devices, the BSLD is the most useful, because it has a large optical gain, relatively small switching energy, and a large on/off ratio. Some system applications for optical signal processing have been reported, e.g. optical time division switching^{19),20)}, and optical data latch²¹⁾.

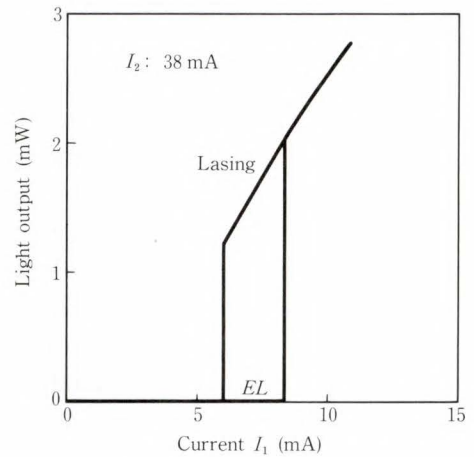
Usually the BSLD is set by light injection and is reset by decreasing the electrical bias. For high-speed operation, many studies about turn-off characteristics have been reported. For example, the turn-off time for light is decreased by increasing the reset current intensity¹⁰⁾. Tomita et al. have reported opti-

mizing the bias condition for the reset region to maximize the relaxation frequency¹³⁾. Tomita et al. achieved flip-flop operation at a repetition rate of 500 Mbit/s using set light signals with a pulse width of 250 ps (2 Gbit/s RZ signals). In Chap. 2, this paper reports an improvement in the electrical reset from a different point of view for higher repetition rate. The repetition rate is mainly limited by large carrier density changes caused by the reset pulse. Therefore, the bias condition for the reset region was optimized to minimize the carrier density change. This produces a flip-flop operation at a repetition rate of 2.5 Gbit/s using set light signals with a pulse width of 130 ps.

As basic research for future technology, the possibility of all-optical signal processing was studied, using no electrical signals even for the reset signals. This is because it has advantages such as no electrical cross-talk, and freedom from grounding and impedance mismatch problems. Only one trial for the optical reset of the BSLD has been reported so far. Inoue et al. have reported the optical reset using the beat vibration between an injected light and the lasing light of the BSLD¹⁶⁾, where the injected light wavelength had to be precisely tuned to the lasing wavelength of the BSLD. In Chap. 3, this



a) Schematic structure



b) Light output vs. electrical bias

Fig. 1—Basic characteristics of the BSLD (Bistable laser diode).

paper proposes and confirms another new optical resetting using gain quenching phenomenon. This has the advantage that the injected light wavelength does not need to be tuned to the lasing wavelength precisely^{17),18)}. This paper also demonstrates all-optical flip-flop operations using light signals having two different wavelengths or two different intensities.

2. Improvement of electrical reset

2.1 Basic mechanism of the BSLD

The basic mechanism of the BSLD is as follows: Figure 1a) shows a schematic diagram of the BSLD structure. It has gain regions and a saturable absorption region. Figure 1b) shows the light output vs. electrical bias. The upper branch is the lasing state and the lower is the *EL* state. By setting the bias current within the hysteresis region, the BSLD operates as an optical flip-flop. When a light is injected into the BSLD, the light pumps the saturable absorption region and the BSLD starts to lase. Then the saturable absorption region is pumped by the lasing light. Therefore, after decreasing the injected light, the BSLD continues to lase. This is the set operation. To reset the BSLD, the gain of the laser should be decreased. For the purpose, the electrical bias is decreased below the hysteresis. Then, the BSLD stops lasing. This is the reset operation.

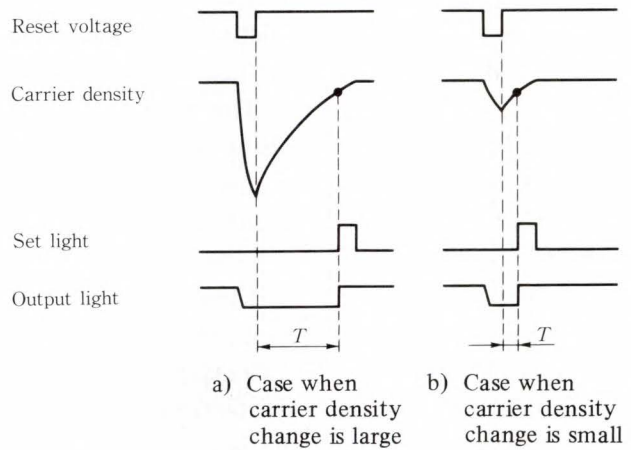


Fig. 2—Carrier density changes after a reset operation.

2.2 Principle of the electrical reset for decreasing the carrier density change.

The repetition rate of the BSLD is limited mainly by the recovery time of the carrier density after a reset operation. Figure 2 shows the carrier density changes of the BSLD after a reset. In Fig. 2a), when the carrier density change caused by a reset pulse is large, small light injection cannot set the BSLD unless the time interval *T* between the reset and set pulse is long, i.e. the recovery time of the carrier density is long. However, in Fig. 2b) when the carrier density change is small, a small light injection can set the BSLD just after the reset, i.e. the recovery time is short. Thus the recovery time of the carrier density is decreased by decreasing the

carrier density change even if its time constant is not shortened.

Figure 3 shows the principle of the method used for decreasing the carrier density change¹⁵⁾. As is well known, the differential gain is higher at lower carrier densities. Thus, at low carrier density (condition B), the carrier density change (Δn_B) with gain change (Δg) is much smaller than Δn_A at the high carrier density (condition A). Therefore, keeping a low carrier density in the reset region is good for small carrier density change. For the low carrier density, the reset region was biased much lower than usual.

2.3 Structure of BSLD

Figure 4 shows the structure of the BSLD used. It has tandem electrodes to control the optical hysteresis characteristics. The cavity is 300 μm long, and the saturable absorption region is about 30 μm long. The reset pulse was applied to region 1. The lasing wavelength was about 1.31 μm . The active region is embedded with a semi-insulating (SI) InP layer grown by MOVPE²²⁾. The resistivity of the SI InP layer is more than $10^8 \Omega\text{cm}$. This BH laser is superior to the conventional p-n junction BH laser because the tandem electrode BSLD must have a high resistance between the two electrodes, allowing independent control of the injection currents. The contact layer of the saturable absorption region was removed by chemical etching to increase the resistance between the two electrodes. This resistance is about 8 k Ω . The capacitance of the device is less than 3 pF over 300 μm .

2.4 Experiment

2.4.1 Methods for maintaining low carrier density

To maintain a small carrier density in the reset region (region 1 in Fig. 4), the following operations were performed.

- 1) The reset region was biased with a constant-voltage source to keep the carrier density low even when the region was pumped by a lasing light.
- 2) The reset region was biased below 1 V for a small carrier density.
- 3) As the reset region has a large loss, the

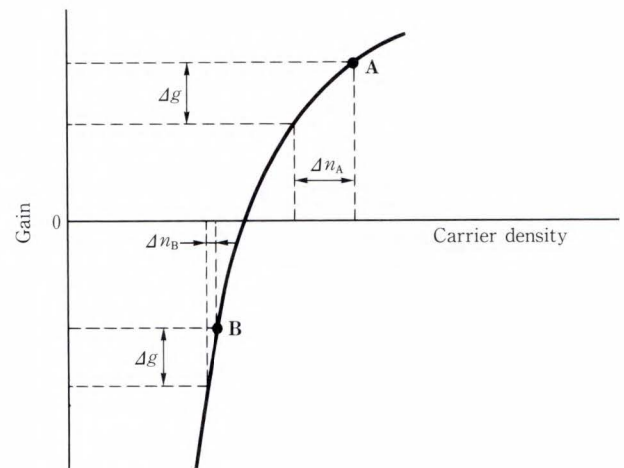


Fig. 3—Principle of the improvement of the electrical reset.

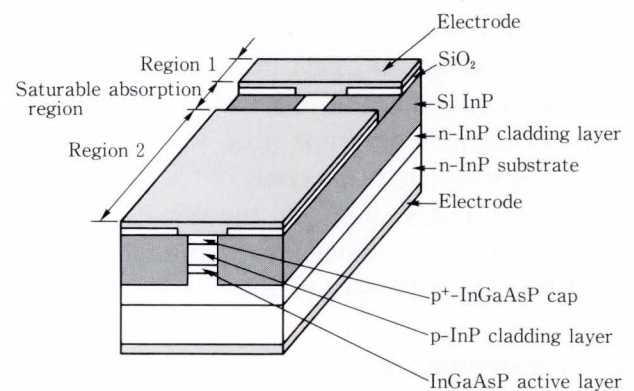


Fig. 4—Structure of BSLD.

region was made only 16 μm long to prevent a large increase in the threshold current.

2.4.2 Static characteristics

Figure 5 shows light output vs current of the BSLD. I_2 is the bias current of the gain region (region 2), and V_1 is the bias voltage of the reset region. The hysteresis width narrows with decreasing V_1 and disappears below $V_1 = 0.2 \text{ V}$. The lowest voltage (V_1) for stable operation is about 0.4 V.

Figure 6 shows the current density (J_1) vs. bias voltage (V_1) of the reset region with the electrode of region 2 open. Conventionally, semiconductor lasers are biased above 1 kA/cm². Therefore by setting V_1 below 1 V, a very low carrier density was expected with the differential gain (loss) being larger than the conventional value.

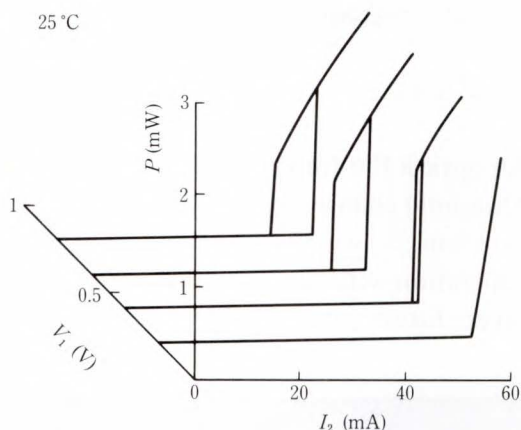


Fig. 5—Light-output vs. current characteristics.

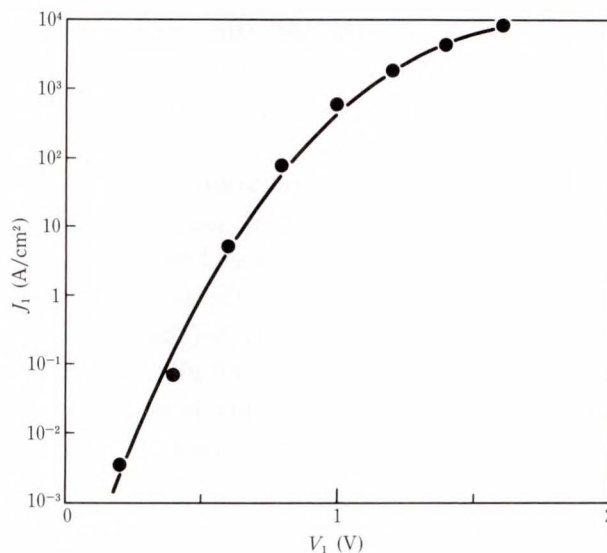


Fig. 6—Current density vs. bias voltage of the reset.

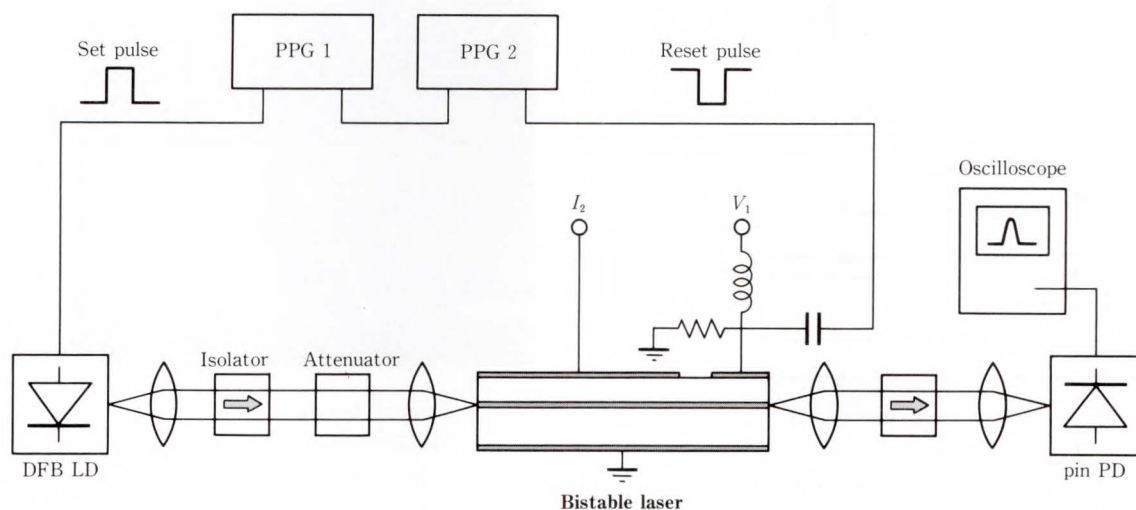


Fig. 7—Experimental setup for dynamic operation.

2.4.3 Experimental setup

Figure 7 shows the experimental setup for dynamic operation. A DFB laser was used for the set light source, and the light was injected into the BSLD. The input light intensity was controlled by an optical attenuator. The light intensity was evaluated by the photo-current of the BSLD. The light output from the BSLD was detected by an InGaAs pin photodiode (10-GHz bandwidth). A 50-Ω resistor was inserted in parallel with the reset region to match the impedance.

2.4.4 Measurement of carrier density change caused by a reset pulse

Instead of directly estimating the carrier density change after the reset, the change of the threshold set light intensity (P_{th}) was measured after the reset operation (see Fig. 8). The horizontal axis shows the time after a reset pulse. The bias was changed from 0.7 V to 0.4 V. Reset and set pulse widths were both 200 ps. The reset pulses height was fixed to be 0.4 V. ΔP is defined as $P_{th}(t=0) - P_{th}(t=\infty)$. The larger the carrier density change caused by the reset, the larger the threshold set light intensity just after the reset $\{P_{th}(t=0)\}$. Therefore it is possible to evaluate the carrier density changes by measuring ΔP . The lower the bias of the reset

region, the smaller the ΔP (the carrier density change). Therefore a lower bias voltage is better for fast operation, as long as the hysteresis exists.

2.4.5 Fast flip-flop operation

A fast optical flip-flop (see Fig. 9) was achieved with the reset region biased at 0.4 V. The reset pulse was 200 ps wide and 0.2 V high. The set pulse width was 130 ps (about 4 Gbit/s RZ signals) with a power of 80 μW . The repetition rate was 2.5 Gbit/s. This is several times faster than any rate yet reported¹³⁾⁻¹⁵⁾. The

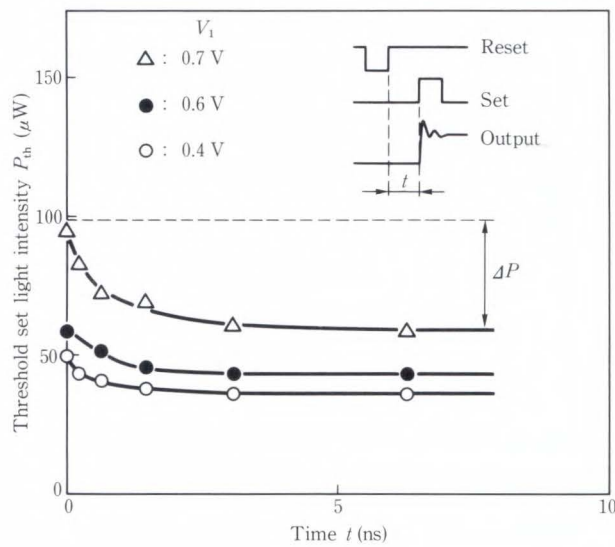


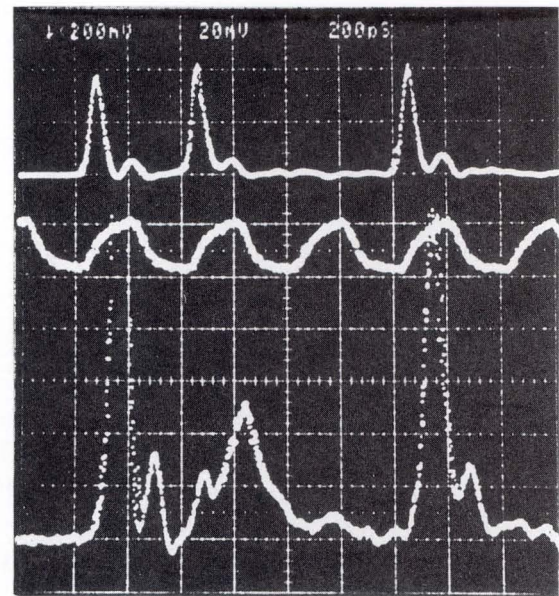
Fig. 8—Change of threshold set light intensity after a reset.

output light corresponds to the set light signal sequence of 1, 1, 0, 1, although there are some pattern effects.

3. All-optical flip-flop operation

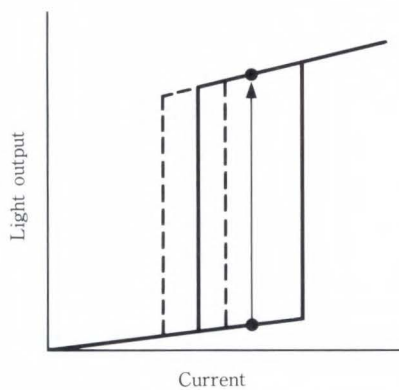
3.1 Threshold changes by light injection

In Chap. 2, we discussed the optical flip-flop operation with optical and electrical signals. However, future optical technology is expected

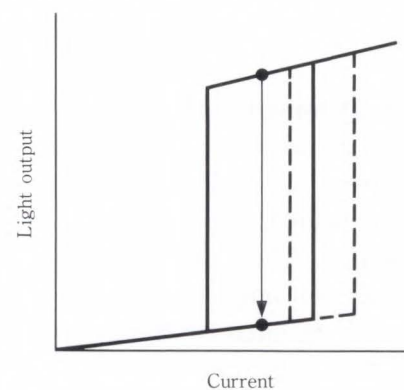


Upper: Set light
Middle: Reset voltage
Lower: Output light of the BSLD

Fig. 9—Fast optical flip-flop operation.



a) Set operation by light injection which pumps the saturable absorption region



b) Reset operation by light injection which quenches the gain of the gain region

Fig. 10—Two operations by threshold current changes caused by light injection.

In both cases, the solid lines show light output vs. current characteristics without light injection, and the dashed lines show those with light injection.

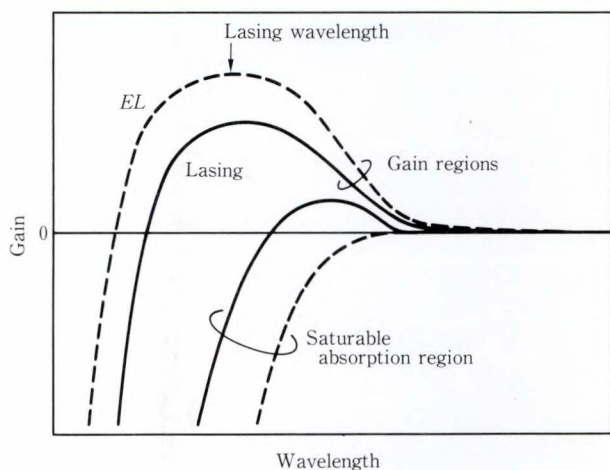


Fig. 11—Gain spectra of the BSLD. The upper two traces are those of the gain regions and the lower two traces are those of the saturable absorption region. The dashed lines show those in the *EL* state, and the solid lines are those in the lasing state.

to consist of all optical signal processing because there is no electrical cross-talk and so on. For all-optical flip-flop operation, it is necessary to perform set and reset operations by light injection. Figure 10 shows schematic diagrams of threshold turn-on and turn-off current changes by light injection. The solid lines show light output vs. current without light injection, and the dashed lines are those with light injection. Case a) shows a well-known set operation using the optical pumping phenomenon. As mentioned above, when an injected light pumps the saturable absorption region, the loss of region decreases and the threshold currents become smaller as shown by the dashed lines. Then the BSLD starts to lase. For the optical reset, however, as shown in b), it is necessary to quench the gain of the gain region and to increase the threshold currents. The authors found that optical reset is possible by using the gain spectra changes of the saturable absorption region between the *EL* and the lasing state.

3.2 Optical reset

3.2.1 Mechanism

The authors first considered the gain spectra of the BSLD. In Fig. 11, the upper two traces show the gain spectra of the gain region, and the

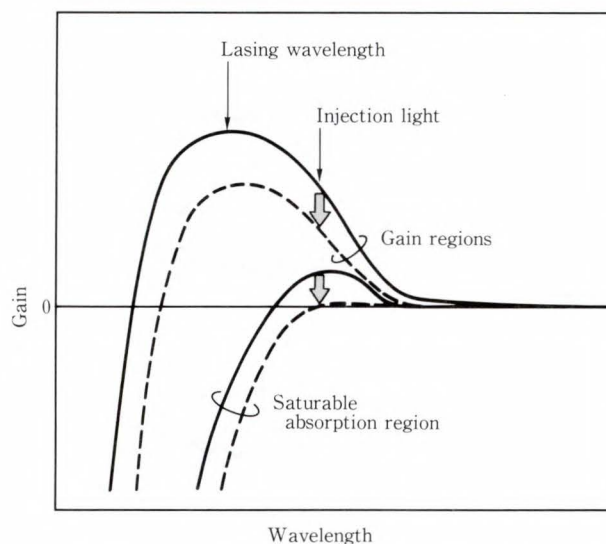


Fig. 12—Gain spectra changes by injection light with a wavelength slightly longer than the lasing wavelength. The solid lines are gain spectra and saturable absorption regions in the lasing state without light injection. The dashed lines are those with light injection.

lower are those of the saturable absorption region. The dashed lines are those in the *EL* state and the solid lines are those in the lasing state. As is well known, in the *EL* state, the saturable absorption region has a large loss coefficient over a wide wavelength range because there is no current injection. Therefore, light in the wide wavelength range can pump the saturable absorption region and set the BSLD. Precisely speaking, for the set operation, the BSLD has a high sensitivity around the lasing wavelength¹⁹⁾. However, in the lasing state, it may have a gain coefficient or small absorption coefficient at a wavelength slightly longer than the lasing wavelength because the region is pumped by the lasing light. Figure 12 shows the gain spectra changes by the injection light with the wavelength slightly longer than the lasing wavelength. In the gain region, the light decreases the carrier density by stimulated emission, and quenches the gain at the lasing wavelength. In the saturable absorption region, the light also reduces the carrier density or scarcely pumps the region. Therefore the light will quench the net gain at the lasing wavelength and stop the lasing¹⁷⁾.

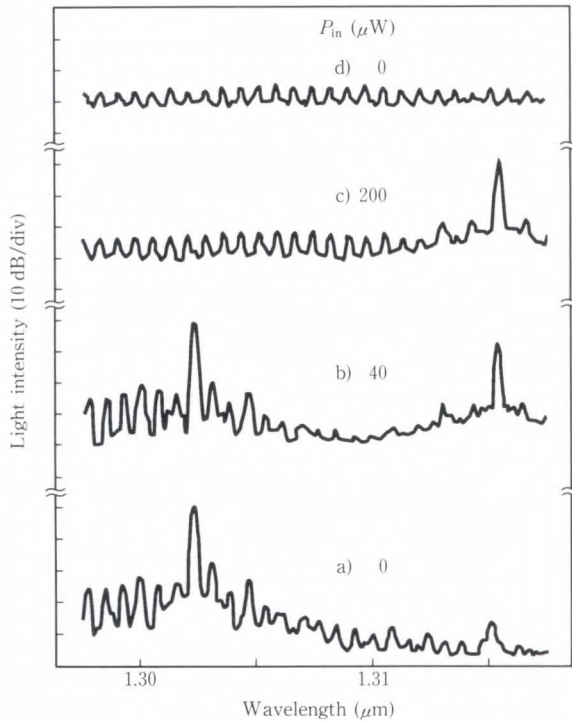
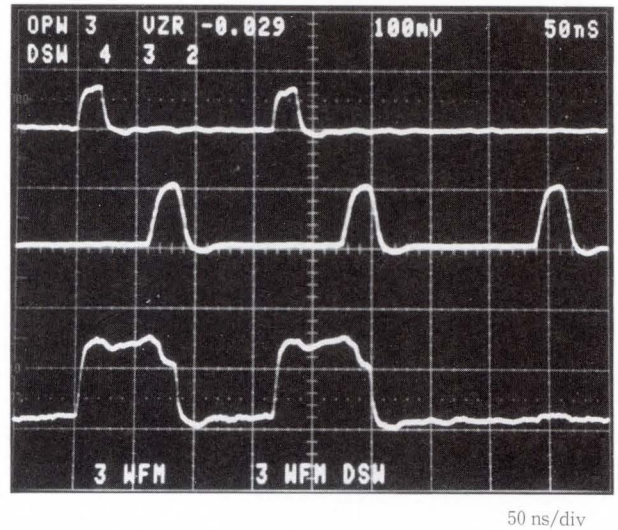


Fig. 13—Spectral changes caused by injection light with a wavelength slightly longer than the lasing wavelength.

3.2.2 Optical reset in the static condition

The optical reset mentioned above was confirmed experimentally. The structure of the BSLD used here was the same as that for the electrical reset experiment described in section 2.3, except for the length of the electrodes. Region 1 was 70 μm long, region 2 was 190 μm long, and the saturable absorption region was 40 μm long. Unlike in Chap. 2, region 1 was biased at the normal condition and acts as a gain region.

Figure 13 shows the results of the optical reset experiment. First, the BSLD was set in the lasing state a). The lasing wavelength was about 1.302 μm. Then, light with a wavelength 13 nm longer than the lasing wavelength was injected into the BSLD b). Lasing continued when the injection light intensity was 40 μW. However, when the injection light intensity reached 200 μW, the BSLD stopped lasing c). Only the amplified injection light was observed. This is evidence of the gain quenching by the light injection discussed above. After this, the injection light intensity was decreased to 0 d).



Upper: Set light
Middle: Reset light
Lower: Output light of the BSLD

Fig. 14—All-optical flip-flop operation¹⁷⁾.

The BSLD remained in the *EL* state. In short, the BSLD was reset by the injection of light with a longer wavelength.

3.2.3 Optical flip-flop operation with light signals of different wavelength

Using the set and reset by light injection, all-optical flip-flop operation was demonstrated (see Fig. 14)¹⁷⁾. The upper trace is the set light, the middle is the reset light, and the lower is the light output from the BSLD. The wavelength of reset light was selected at 1.3154 μm, which is about 13 nm longer than the lasing wavelength. The wavelength of the set light (1.3044 μm) was near the lasing wavelength. The reset and set light intensities were 90 μW and 30 μW. The pulse width was about 20 ns. Light output from the BSLD corresponded to the injection set light signal sequence 1,1,0. Thus, using light having two different wavelengths, optical pumping and gain quenching was achieved.

3.3 Optical set and reset using single-wavelength light signals

3.3.1 Wavelength dependence of threshold set and reset light intensity

The method of optical reset was described above. However the method requires two optical signals of different wavelengths to set and

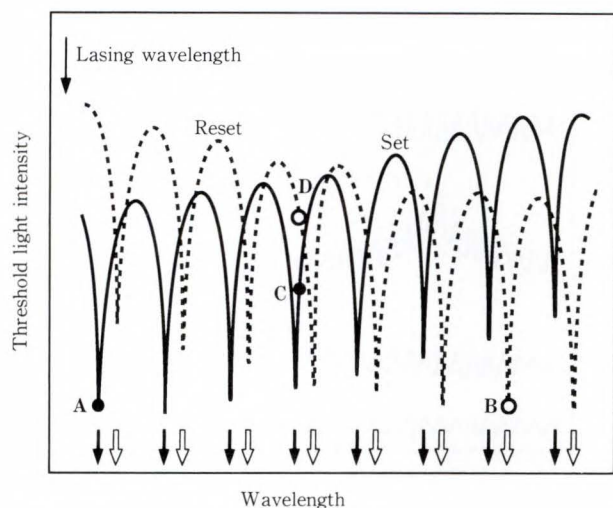


Fig. 15—Wavelength dependence of threshold set and reset light in intensity. The solid line shows the threshold set light intensity, and the dashed line shows threshold reset light intensity. Black and white arrows indicate the resonant wavelength in the *EL* and the lasing state. Points **A** and **B** show conditions of set and reset using light beams of two different wavelengths. Points **C** and **D** show those using light beams of two different intensities.

reset the BSLD. Here, to optically set and reset the BSLD using single-wavelength light signals, the wavelength dependence of the threshold set and reset light intensity is discussed in detail.

As mentioned in subsection 3.2.1, the sensitivity for set operation is high around the lasing wavelength, and the sensitivity for reset is high around the wavelength slightly longer than the lasing wavelength. In addition, the BSLD has a Fabry-Perot cavity. So, when light is collinearly injected into the BSLD, the wavelength dependence of the threshold set or reset light intensity will be modulated by the resonant characteristics of the Fabry-Perot cavity as shown in Fig. 15. The solid line shows the threshold set light intensity and the dashed line shows threshold reset light intensity. The black and white arrows are the resonant wavelengths in the *EL* and the lasing state. They are different because the carrier densities of the gain and saturable absorption regions change between the *EL* and the lasing state, and as a result, the refractive index of the regions changes. The

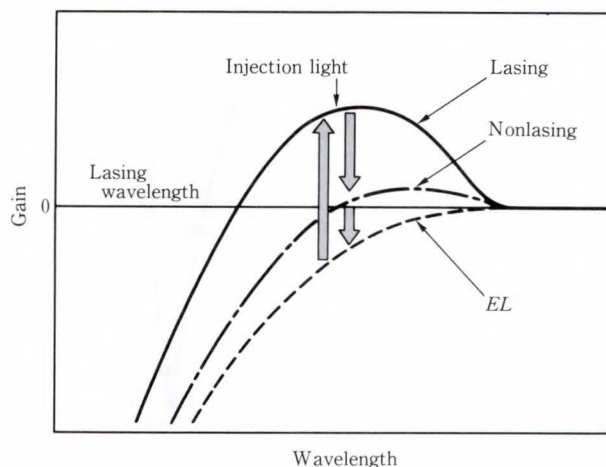


Fig. 16—Mechanism of optical set and reset using single-wavelength light signals. As the injection light intensity increases, the gain spectrum changes from the lower line (the *EL* state) to the upper line (the lasing state) and to the middle line. When the injection light is decreased quickly, the gain spectrum goes to the lower line (*EL* state) again.

threshold set light intensity has minima near the resonant wavelengths in the *EL* state, and the threshold reset light intensity has minima near those in the lasing state¹⁷⁾. In short, they have minima near the resonant wavelengths in the initial state before light injection.

In subsection 3.2.3, a light at point **A** was used for setting and a light at point **B** for resetting. Thus by changing the wavelength of injection light, optical pumping and gain quenching were achieved. However, if a light at point **C** acts as the set light and a light at point **D** acts as the reset light, single-wavelength light will pump the saturable absorption region and quench the gain by changing the intensity of the light.

As shown in Fig. 16, the gain spectrum in the saturable absorption region will probably be changed by injection light with a wavelength at point **C** and **D**. The lower dashed line shows the gain spectrum in the *EL* state. In this state, the region has a loss coefficient even at a wavelength slightly longer than the lasing wavelength. So when light at the wavelength is injected into the BSLD, the light pumps the saturable absorption region and sets the laser diode. The

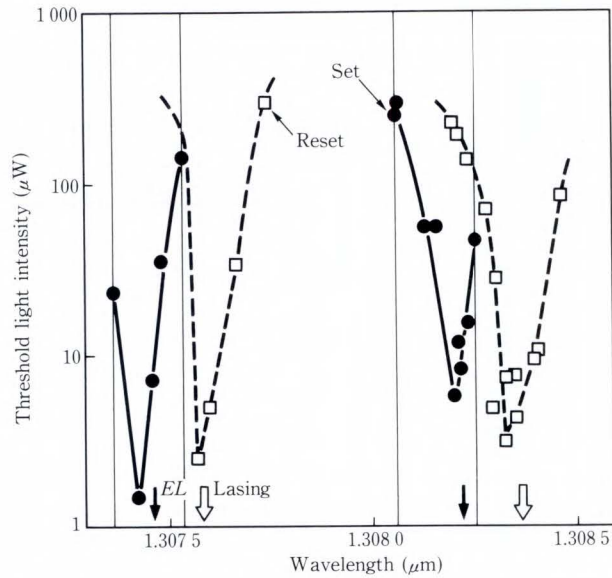


Fig. 17—Experimental results of the wavelength dependence of the threshold set or reset light intensity. Circles show the threshold set light intensity and squares are the threshold reset light intensity. Black and white arrows indicate the resonant wavelength in the *EL* and the lasing state.

gain spectrum then changes as shown by the upper solid line. In this state, because the saturable absorption region is pumped by the lasing light, it has a gain coefficient at a wavelength longer than the lasing wavelength, as mentioned in subsection 3.2.1. However, when the injection light intensity is further increased, the light will quench the gain of the saturable absorption region as shown by the middle line. Thus the light stops the lasing. Although when the light is then decreased slowly, the BSLD starts to lase again, when the light is decreased faster than the recovery time of the net gain, the BSLD will enter the *EL* state. Therefore, it is possible to set and reset the BSLD with a single-wavelength light having a wavelength slightly longer than the lasing wavelength.

3.3.2 Experimental results under static conditions

Figure 17 shows the experimental results of the wavelength dependence of the threshold set and reset light intensity. A DFB laser is used for the set and reset light source and the light is injected into the BSLD collinearly with the

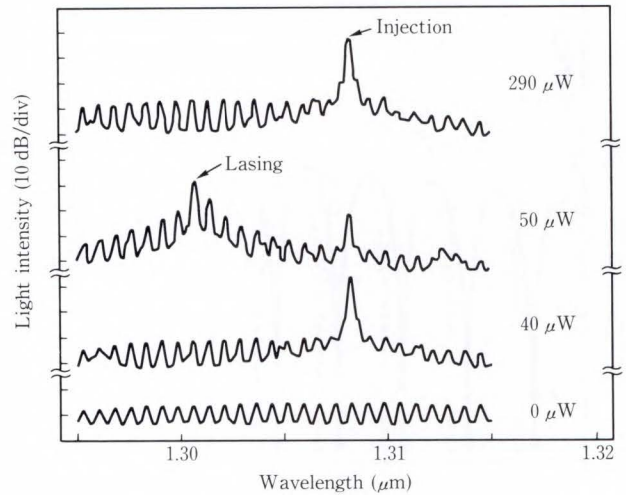


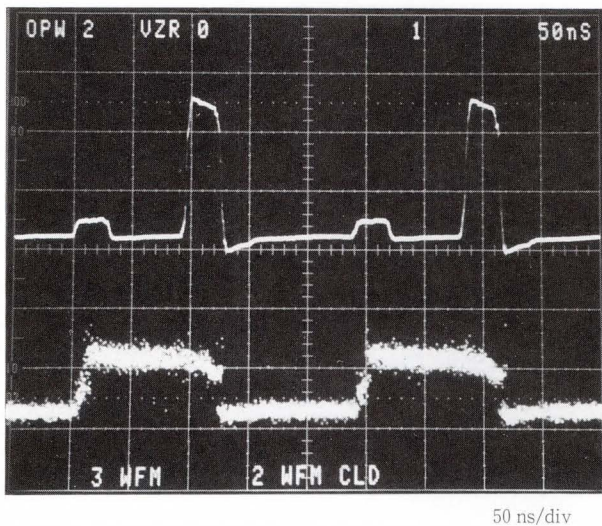
Fig. 18—Spectral changes caused by light injection. The wavelength of the injection light is in the shaded region of Fig. 17.

lasing light of the BSLD. The circles show the threshold set light intensity, and the squares show the threshold reset light intensity. As mentioned above, the wavelength dependence has resonant characteristics. In addition, the threshold set and reset light intensity have different resonant wavelengths. It should be noted that in the shaded wavelength region at the right, the single-wavelength light sets the BSLD and stops the lasing as expected.

Figure 18 shows the spectral changes of the BSLD caused by single-wavelength light injection in the shaded wavelength region of Fig. 17. First, the BSLD was in the *EL* state. Light with a wavelength slightly longer than the lasing wavelength ($1.302 \mu\text{m}$) was injected into the BSLD and the $50 \mu\text{W}$ injection set the laser diode. When the injected light intensity reached $290 \mu\text{W}$, the lasing stopped. In short, single-wavelength, low-intensity light pumped the saturable absorption region and set the laser diode, and high-intensity light quenched the net gain and stopped the lasing.

3.3.3 Optical flip-flop operation with single-wavelength light signals

We achieved optical flip-flop operation of the BSLD with single-wavelength light signals, using the phenomena described above¹⁸⁾. Figure 19 shows the optical flip-flop operation.



Upper: Set and reset light
Lower: Output light of the BSLD

Fig. 19—Optical flip-flop operation using single-wavelength signals.

The upper trace is the set and reset light. The lower trace is the output light. The wavelength of the set and reset light was $1.30822 \mu\text{m}$. The set light intensity was $30 \mu\text{W}$ and the reset light intensity was $170 \mu\text{W}$. Their pulse width was 30 ns. The single-wavelength, low-intensity light set the BSLD and the high-intensity light reset it.

Optical flip-flop operation was also achieved using single-wavelength light signals which have different pulse widths but the same intensity.

4. Conclusion

A bistable laser diode with a saturable absorber was studied from two points of view. One is high-speed operation using electrical reset and optical set signals. And the other is a new optical reset for all-optical signal processing, which will be important in the future.

1) High-speed operation

The repetition rate of the BSLD is mainly limited by the large carrier density changes caused by the electrical reset. To reduce the carrier density change, the reset region was biased lower than 1 V where differential gain (loss) is large. And by experiment, it was confirmed that the lower bias of the reset region is better for small carrier density change. Flip-flop

operation at a 2.5 Gbit/s repetition rate was achieved.

2) Optical reset using optical gain quenching

A new optical reset method using optical gain quenching has been proposed and experimentally confirmed for the first time. And all optical flip-flop operations with light signals of two different wavelengths or two different intensities were successfully demonstrated.

References

- 1) Gibbs, H. M., Tarng, S. S., Jewell, J. L., Weinberger, D. A., Tai, K., Gossard, A. C., McCall, S. L., Passner, A., and Wiegmann, W.: Room-temperature excitonic optical bistability in a GaAs–GaAlAs superlattice etalon. *Appl. Phys. Lett.*, **41**, 3, pp. 221-222 (1982).
- 2) Otsuka, K., and Iwamura, H.: Analysis of a multistable semiconductor light amplifier. *IEEE J. Quantum Electron.*, **QE-19**, 7, pp. 1184-1186 (1983).
- 3) Miller, D.A.B., Chemra, D.S., and Damen, T.C.: Novel hybrid optically bistable switch: The quantum well self-electro-optic effect device. *Appl. Phys. Lett.*, **45**, 1, pp. 15 (1984).
- 4) Kasahara, K., Tashiro, Y., Hamano, N., Sugimoto, M., and Yanase, T.: Double heterostructure optoelectronic switch as a dynamic memory with low-power consumption. *Appl. Phys. Lett.*, **52**, 9, pp. 679-681 (1988).
- 5) Lasher, G.J.: Analysis of a proposed bistable injection laser. *Solid-State Electron.*, **7**, 10, pp. 707-716 (1964).
- 6) Kawaguchi, H., and Iwane, G.: Bistable operation in semiconductor lasers with inhomogeneous excitation. *Electron. Lett.*, **17**, 4, pp. 167-168 (1981).
- 7) Harder, Ch., Lau, K.Y., and Yariv, A.: Bistability and pulsations in cw semiconductor lasers with a controlled amount of saturable absorption. *Appl. Phys. Lett.*, **39**, 5, pp. 382-384 (1981).
- 8) Ueno, M. and Lang, R.: Conditions for self-sustained pulsation and bistability in semiconductor lasers. *J. Appl. Phys.*, **58**, 4, pp. 1689-1692 (1985).
- 9) Liu, H.F., Kamiya, Y., and Du, B.X.: Temperature Dependence of Bistable InGaAsP/InP Lasers. *J. Quantum Electron.*, **QE-22**, 9, pp. 1579-1586 (1986).
- 10) Tomita, A., Terakado, T., and Suzuki, A.: Turn-off characteristics of bistable laser. *J. Appl. Phys.*, **59**, 6, pp. 1839-1842 (1986).

- 11) Hori, Y., Sato, H., Serizawa, H., and Kajiura, T.: Effect of device parameters on bistable semiconductor laser. *J. Appl. Phys.*, **60**, 2, pp. 534-537 (1986).
- 12) Liu, H.F., Hashimoto, Y., and Kamiya, T.: Switching characteristics and maximum repetitive frequency of InGaAs/InP bistable injection lasers. *IEEE J. Quantum Electron.*, **QE-24**, 1, pp. 43-51 (1988).
- 13) Tomita, A., Ohkouchi, S., and Suzuki, A.: 170 ps fast switching response in bistable laser diodes with electrically controlled saturable absorber. Tech. Digest Photonic Switching, 1987, FC2, pp. 119-121.
- 14) Öhander, U., Blixt, P., and Sahlén, O.: Operation tolerances of a bistable laser optically switched at 500 MHz with picosecond, ultra-low energy pulses. Proc. Europ. Conf. Opt. Commun. 1, WeB16-1, 1989, pp. 288-291.
- 15) Sanada, T., Odagawa, T., Machida, T., Wakao, K., and Yamakoshi, S.: New reset method for optical bistable laser diodes. Extended Abst. 21st Conf. Solid-State Devices Mat., Tokyo, 1989, Jpn. Soc. Appl. Phys., D-6-2, pp. 321-324.
- 16) Inoue, K., and Oe, K.: Optically triggered off-switching in a bistable laser diode using a two-electrode DFB-LD. *Electron. Lett.*, **24**, 9, pp. 512-513 (1988).
- 17) Odagawa, T., Sanada, T., and Yamakoshi, S.: All optical flip-flop operation of bistable laser diode. Extended Abst. 20th Conf. Solid-State Devices, Mat., Tokyo, 1988, Jpn. Soc. Appl. Phys., D-5-1, pp. 331-334.
- 18) Odagawa, T., Yamakoshi, S.: Optical set-reset operations of bistable laser diode with single-wavelength light. *Electron. Lett.*, **25**, 21, pp. 1428-1429 (1989).
- 19) Suzuki, S., Terakado, T., Komatsu, K., Nagashima, K., Suzuki, A., and Kondo, M.: An experiment on high-speed optical time-division switching. *IEEE J. Lightwave Technol.*, **LT-4**, 7, pp. 894-899 (1986).
- 20) Shimoe, T., Kuroyanagi, S., Murakami, K., Rokugawa, H., Mekada, N., and Odagawa, T.: An experimental 512-Mbps time-division photonic switching system. Tech. Digest Photonic Switching, 1989, FC2, pp. 136-138.
- 21) Fujimoto, N., Rokugawa, H., Yamaguchi, K., Masuda, S., Yamakoshi, S.: Photonic highway: Broad-band ring subscriber loops using optical signal processing. *IEEE J. Lightwave Technol.*, **7**, 11, pp. 1798-1805 (1989).
- 22) Wakao, K., Nakai, K., Sanada, T., Kuno, M., Odagawa, T., and Yamakoshi, S.: InGaAsP/InP planar buried hetero-structure lasers with semi-insulating InP current blocking layers grown by MOCVD. *J. Quantum Electron.*, **QE-23**, 6, pp. 943-947 (1987).



Tetsufumi Odagawa

Optical Semiconductor Devices
Laboratory
FUJITSU LABORATORIES, ATSUGI
Bachelor of Science
Kyoto University 1984
Master of Information Processing
Tokyo Institute of Technology 1986
Specializing in Optical Semiconductor
Lasers



Shigenobu Yamakoshi

Optical Semiconductor Devices
Laboratory
FUJITSU LABORATORIES, ATSUGI
Bachelor of Electronic Eng.
Kanazawa University 1970
Dr. of Electronic Eng.
Tohoku University 1975
Specializing in Optical Semiconductor
Devices



Tatsuyuki Sanada

Optical Semiconductor Devices
Laboratory
FUJITSU LABORATORIES, ATSUGI
FUJITSU Technical College 1975
Specializing in Optical Semiconductor
Devices

High Performance p-Substrate Buried Heterostructure Laser Emitting at 1.3 μm

• Katsuhiko Kihara • Shuichi Miura • Ichiro Ushijima

(Manuscript received November 30, 1989)

A high performance buried heterostructure laser diode emitting at 1.3 μm has been developed by applying a p-substrate to a flat-surface buried heterostructure. A high internal quantum efficiency of 94.3 percent, a very low threshold current of 5.8 mA at 25 °C, and a high temperature operation (for example, up to 15 mW at 100 °C) have been achieved with this structure. An error-floor-free transmission of up to 600 Mbit/s NRZ using pseudo-random modulation with a -80 ps/nm fiber dispersion and up to 1.2 Gbit/s with a -40 ps/nm fiber dispersion have also been obtained. Moreover, a high reliability (median lifetime of more than 1×10^6 h for 70 °C at 5 mW) has been realized.

1. Introduction

A 1.3 μm wavelength InGaAsP/InP laser diode has been developed as a key device for long-haul high-bit-rate optical transmission systems. The 1.3 μm wavelength was chosen because at 1.3 μm a single mode fiber has zero dispersion and a low loss. We have developed a long wavelength flat-surface buried heterostructure distributed feedback (FBH-DFB) laser. This laser exhibited a high performance, for example, low threshold current, high external differential efficiency, and high single longitudinal mode operation yield. It was developed for long-distance and giga-bit optical transmission systems^{1,2}.

Recently, 1.3 μm wavelength lasers have been demanded in order to increase communication capacity in short and medium distance communication, high bit rate local area networks, local loops, and computer links. Such lasers must operate in harsh environments, for example, high temperature. To realize high performance, several types of structures for 1.3 μm p-substrate laser diodes have been developed. Some examples are a buried heterostructure (BH) laser on p-substrate^{3,4}, a p-substrate buried crescent (PBC) laser⁵, and

a V-grooved inner stripe on p-substrate (VIPS) laser⁶.

We have developed a high performance laser diode by applying a p-substrate to a flat-surface buried heterostructure⁷. Its excellent static characteristics include a high internal quantum efficiency of 94.3 percent, a very low threshold current of 5.8 mA at 25 °C, and up to 15 mW of output at 100 °C.

Error-free transmission characteristics have been obtained up to 600 Mbit/s NRZ using pseudo-random modulation with a -80 ps/nm fiber dispersion, and up to 1.2 Gbit/s with a -40 ps/nm fiber dispersion. A high reliability (median lifetime of more than 1×10^6 h for 70 °C at 5 mW) has also been realized.

In this paper, we describe the design, fabrication, characteristics, and reliability of this device.

2. Design concept

Figure 1 shows a schematic cross-section of the p-substrate flat-surface buried heterostructure (P-FBH) laser diode. To realize high performance even at high temperature, the p-substrate flat-surface buried heterostructure is made using several techniques.

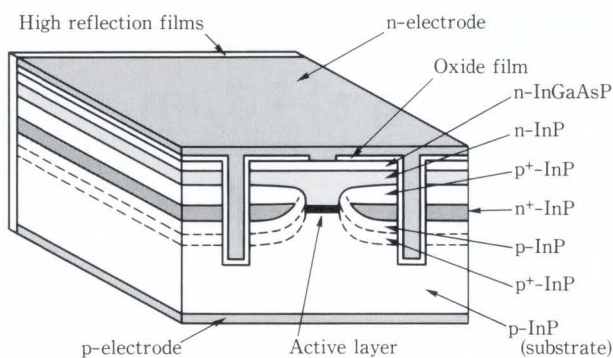


Fig. 1—Schematic cross-section of 1.3 μm wavelength P-FBH laser diode.

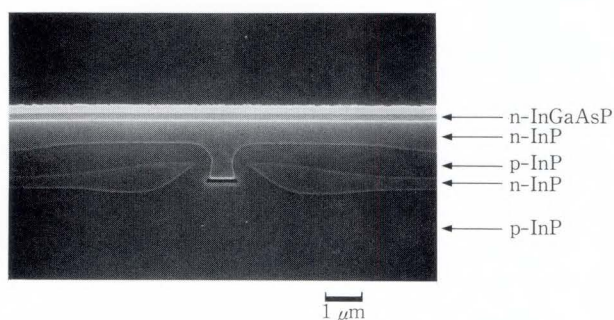


Fig. 2—Scanning electron photomicrograph of cross-section of 1.3 μm wavelength P-FBH laser diode.

The key points are as follows:

- 1) The side walls of the mesa are shifted from the (111)A surface. This reduces the leakage current generated by the formation of non-radiative recombination center of the (111)A interface.
- 2) The p-n-p-n current blocking layers are composed of a p-n-p and n-p-n transistor. The bases must be more highly doped than the emitters in order to reduce the gain. Therefore, a blocking layer doping level of $p^+ (2 \times 10^{18}/\text{cm}^3)$ - $p (4 \times 10^{17}/\text{cm}^3)$ - $n^+ (1.4 \times 10^{18}/\text{cm}^3)$ - $p^+ (2 \times 10^{18}/\text{cm}^3)$ - $n (5 \times 10^{17}/\text{cm}^3)$ is used. This suppresses the thyristor action of the p-n-p-n blocking layers⁸⁾⁻¹⁰⁾.
- 3) In the second growth stage, the first p^+ -p InP layers are grown sufficiently thick so that the next n-InP layer can be separated from the n-cladding layer. As a result, there is no contact between the n-cladding and

n-blocking layers.

Therefore, there is no compensated region between the n-cladding and n-blocking layers. A scanning electron photomicrograph of a cross-section of the P-FBH laser is shown in Fig. 2. By using this technique, the separation width between the n-cladding and n-blocking layers is controllable within 0.3-0.5 μm over the whole wafer. The leakage current near the active region can be reduced by using a narrow separation width. The gate current of the p-n-p-n thyristor can also be suppressed. This blocking layer sufficiently confines the driving current to the active region and sufficiently suppresses the gate current. This is the case even at high temperatures. The above conditions are necessary for the realization of fabrication reproducibility, excellent uniformity of device characteristics, and high operation yield.

3. Fabrication

P-FBH lasers were fabricated by three-step liquid phase epitaxial (LPE) growth. In the first growth, a p-InP buffer layer, p-InGaAsP active layer (0.12 μm thick), n-InP cladding layer, and n-InGaAsP cap layer were grown on a p-InP substrate. A SiO_2 mask to delineate the stripe geometry was patterned on this wafer, and the wafer was then etched with an etchant of HBr, H_2O_2 , and H_2O to form the mesa structure¹¹⁾. By using this etchant, the side walls of the active layer were shifted from the (111)A surface. The width of the active region was 0.8-1.2 μm . In the second growth, p^+ -p-n $^+$ - p^+ -n InP blocking layers (1.0-1.5 μm thick) were grown. The second p-InP layers were grown thick to separate the n-InP and n-cladding layers. After removing the SiO_2 mask and etching the n-InGaAsP cap layer of the first growth, an n-InP cap and n-InGaAsP contact layers were grown in the third growth.

After the growth process, the mesa structure was formed to reduce the capacitance of the p-n junction in the current-blocking layers. This structure enables a high speed response. The mesa width was about 10 μm . Next, an n-electrode and p-electrode were formed, the rear facet was coated with three layers of

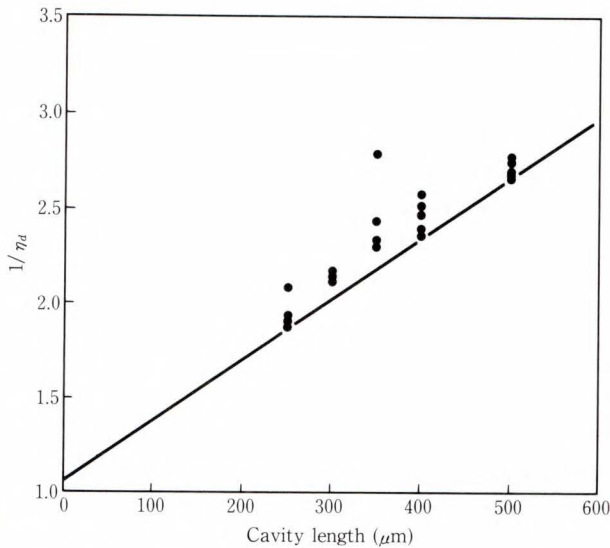


Fig. 3—Reciprocal of external differential quantum efficiency versus cavity length.

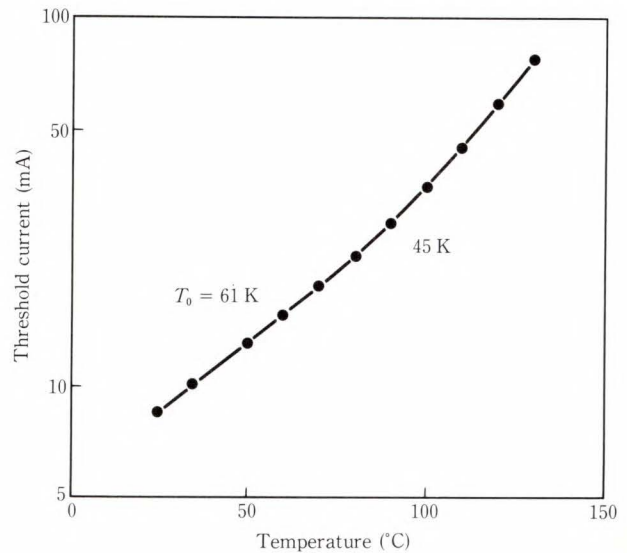


Fig. 5—Temperature dependence of threshold current of P-FBH laser.

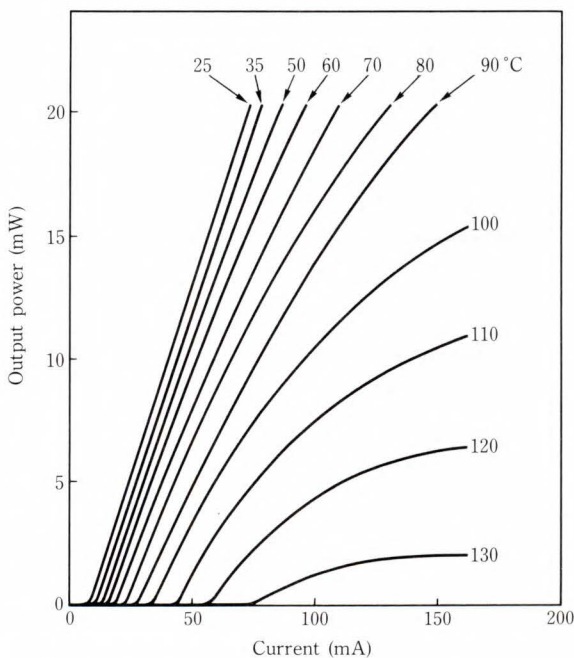


Fig. 4—Temperature dependence of CW output-power/current characteristics of P-FBH laser.

high reflection (HR) films of ($\text{SiO}_2/\text{a-Si}/\text{SiO}_2$). The reflectivity was about 80 percent. Finally, the front facet was cleaved and the P-FBH laser diode was mounted junction-up on a heatsink.

4. Characteristics

4.1 Static characteristics

Internal quantum efficiency is estimated

from the CW output-power/current characteristics of lasers with different cavity lengths. The equation for the differential quantum efficiency is given by

$$\frac{1}{\eta_d} = \frac{1}{\eta_i} \left\{ 1 + \frac{2\alpha_i L}{\ln\left(\frac{1}{R_f \cdot R_r}\right)} \right\}, \quad \dots (1)$$

where η_d is the total external differential quantum efficiency of the front and rear facets, η_i is the internal quantum efficiency, α_i is the internal loss, L is the cavity length, and R_f and R_r are the reflectivities of the front and rear facets. When $1/\eta_d$ is plotted against L , the intercept at $L = 0$ gives the internal quantum efficiency and the internal loss can be solved using Equation (1). The CW output-power/current characteristics of five or six samples for each cavity length from 250 μm to 500 μm were measured. The front/rear ratio of the external differential quantum efficiency was 4.0. The results are shown in Fig. 3. At 25 $^\circ\text{C}$, the internal quantum efficiency was 94.3 percent and the internal loss was 20.7/cm¹²). This internal quantum efficiency is the best so far reported for double heterostructure (DH), and we believe it to be due to the optimum design and high quality of the crystal.

The temperature dependence of the CW output-power/current of a P-FBH laser with a cavity length of 300 μm is shown in Fig. 4. A high power operation of up to 15 mW at 100 $^{\circ}\text{C}$ and up to 6 mW at 120 $^{\circ}\text{C}$ have been achieved using the P-FBH structure. The highest lasing temperature was 130 $^{\circ}\text{C}$ and the output-power was 2 mW.

The temperature dependence of the threshold current is shown in Fig. 5. The threshold current was 8.5 mA at 25 $^{\circ}\text{C}$ and 34.1 mA at 100 $^{\circ}\text{C}$. The characteristic temperature was 61 K at 50 $^{\circ}\text{C}$ and 45 K at 100 $^{\circ}\text{C}$. The lowest thresh-

old current of n-substrate FBH (N-FBH) lasers with HR films was 11.6 mA at 25 $^{\circ}\text{C}$ and 55.7 mA at 100 $^{\circ}\text{C}$. Therefore, the threshold current of the P-FBH laser was 30 percent less than that of the N-FBH laser.

Figure 6 shows an example spectrum at 25 $^{\circ}\text{C}$, 5 mW. The peak wavelength was 1.306 μm and the full width at half maximum (FWHM) of the spectrum was 1.8 nm. A small FWHM is essential for long distance and high bit rate transmissions.

Figure 7 shows a typical far field pattern (FFP) at 25 $^{\circ}\text{C}$, 3 mW. The FWHM of the FFP

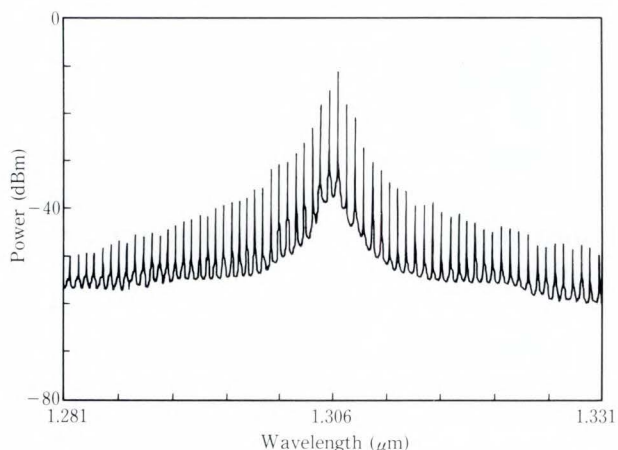


Fig. 6—Example spectrum of P-FBH laser at 25 $^{\circ}\text{C}$, 5 mW.

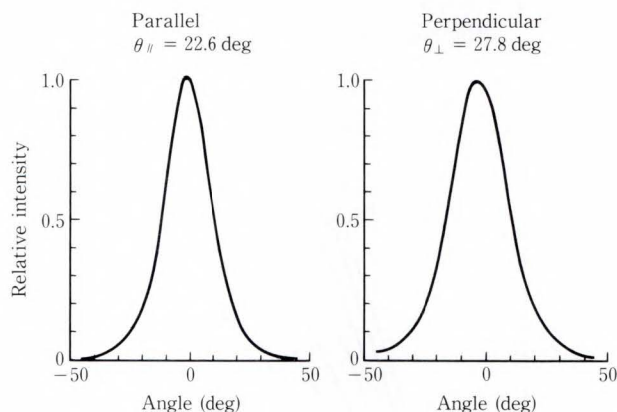
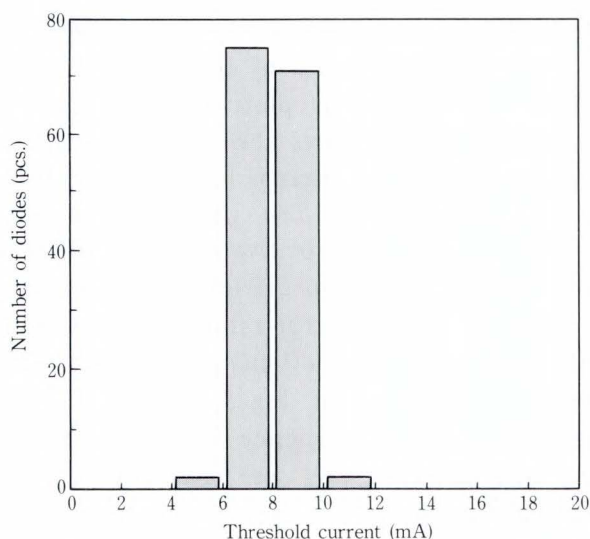
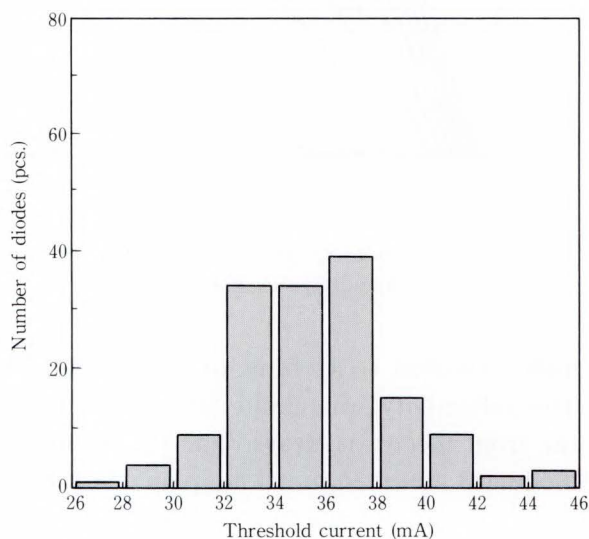


Fig. 7—Typical far field pattern (FFP) of P-FBH laser at 25 $^{\circ}\text{C}$, 3 mW.

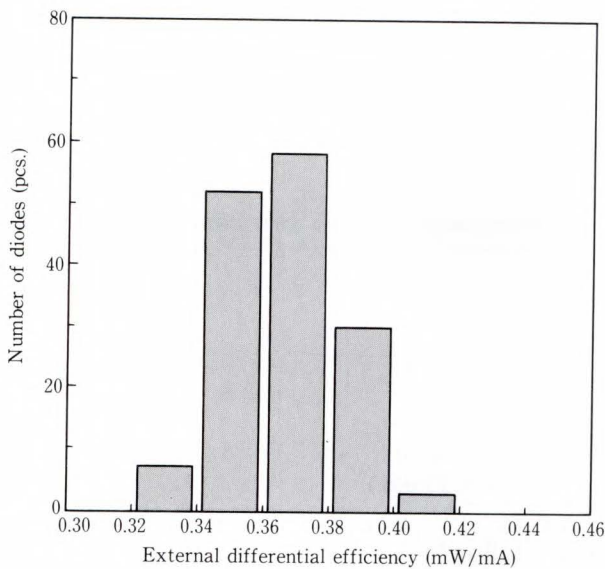


a) $T_a = 25^{\circ}\text{C}$

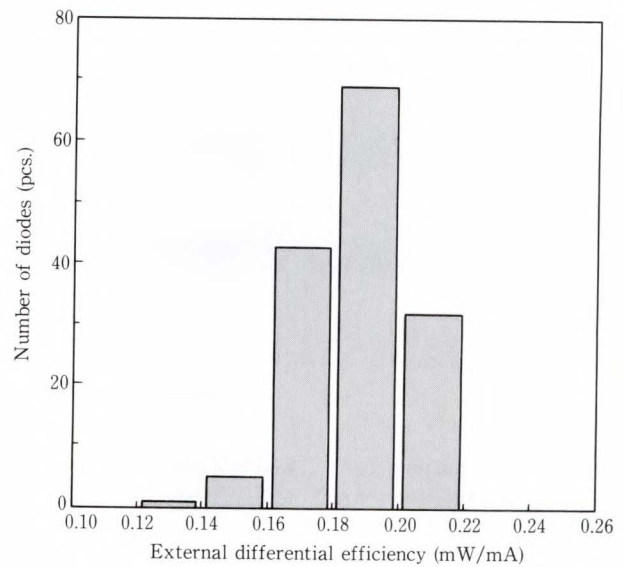


b) $T_a = 100^{\circ}\text{C}$

Fig. 8—Histograms of CW threshold current of P-FBH lasers ($N = 150$ pcs.).



a) $T_a = 25^\circ\text{C}$



b) $T_a = 100^\circ\text{C}$

Fig. 9—Histograms of external differential efficiency at 3 mW from front facet of P-FBH lasers ($N = 150$ pcs.).

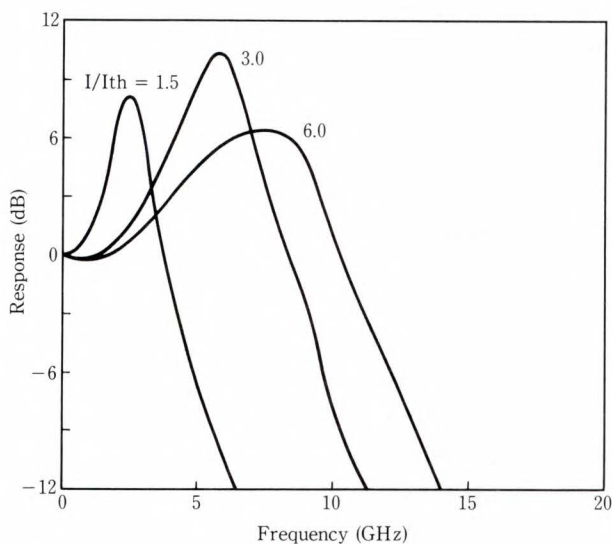


Fig. 10—Small-signal frequency response of P-FBH laser without HR films.

was 22.6 deg in the parallel direction and 27.8 deg in the perpendicular direction. A narrow and stable single lobe was obtained. These results show that high coupling to a single mode fiber can be realized with a narrow FFP.

One hundred and fifty chips having a threshold current below 20 mA at 25 °C and a cavity length of 300 μm were cleaved from ten wafers. The CW output-power/current characteristics were measured at 25 °C and 100 °C. Histograms of the threshold current and the external dif-

ferential efficiency at 3 mW from the front facet are shown in Figs. 8 and 9. The average value of the threshold current was 7.9 mA at 25 °C and 35.6 mA at 100 °C. The average value of the external differential efficiency was 0.365 mW/ mA at 25 °C and 0.186 mW/mA at 100 °C. The lowest threshold current was 5.8 mA at 25 °C and 26.7 mA at 100 °C. These results show that P-FBH lasers with high-performance static characteristics even at high temperatures are achievable.

4.2 Modulation characteristics

Figure 10 shows the small-signal frequency response of the P-FBH laser without HR films. The bias current was set at 1.5Ith, 3Ith, and 6Ith. The -3 dB modulation bandwidth above 11 GHz was achieved at a bias current of 6Ith. This frequency response is sufficient for use in giga bit modulation. Figure 11 shows the eye pattern under modulation at 2.4 Gbit/s NRZ. The bias current was set at the threshold level and the peak power was 5 mW. A well-opened eye pattern was obtained. The high speed response characteristics are due to the 10 μm mesa P-FBH structure, which reduces the parasitic capacitance of the p-n junction in the current blocking layers.

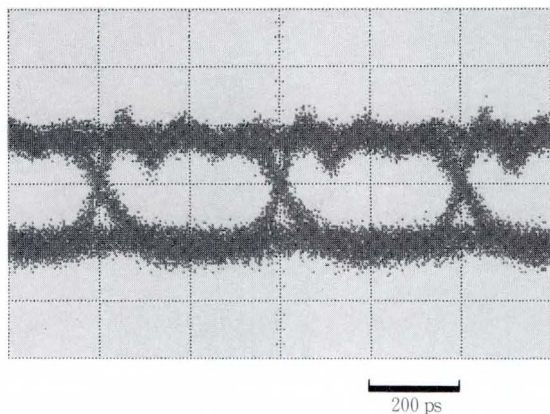


Fig. 11—Eye pattern using 2.4 Gbit/s NRZ pseudorandom modulation (threshold bias current, 5 mW peak power).

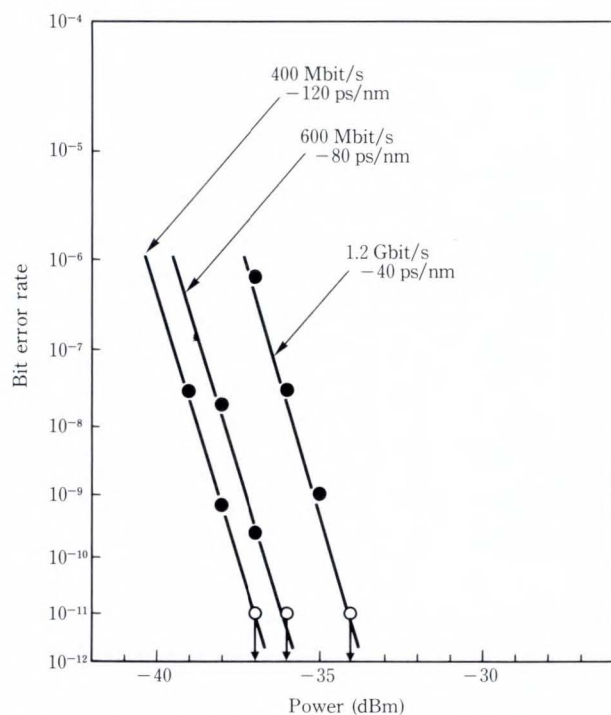


Fig. 12—Results of bit-error-rate measurement. Conditions are 400 Mbit/s NRZ with a -120 ps/nm dispersion, 600 Mbit/s NRZ with a -80 ps/nm dispersion, and 1.2 Gbit/s NRZ with -40 ps/nm dispersion (threshold bias current, 3 mW peak power).

4.3 Transmission characteristics

Figure 12 shows the results of bit-error-rate measurements. The bit rates were 400-, 600-Mbit/s, and 1.2 Gbit/s using NRZ pseudorandom modulation. In the measurements, the bias current was set at the threshold level and the peak optical power was set at 3 mW.

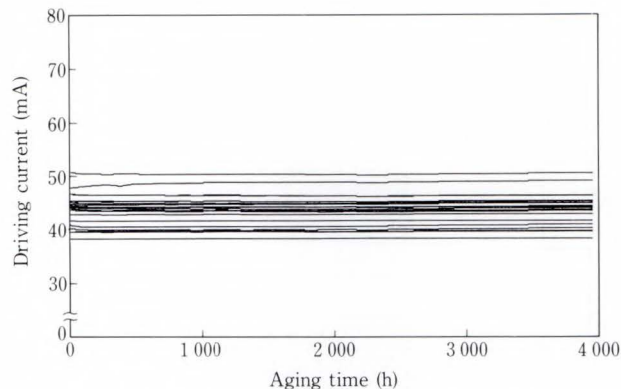


Fig. 13—APC aging tests of P-FBH lasers at 70 °C, 5 mW ($N = 25$ pcs.).

The following floor-free performances were obtained: 400 Mbit/s with a -120 ps/nm fiber dispersion (45 km distance), 600 Mbit/s with a -80 ps/nm fiber dispersion (30 km distance), and 1.2 Gbit/s with a -40 ps/nm fiber dispersion (15 km distance). The high speed response characteristics and narrow stable spectrum enable high bit rate transmission even for modulation at 1.2 Gbit/s.

5. Reliability

To investigate the reliability of the P-FBH laser diode, an automatic power control (APC) mode aging test at an ambient temperature of 70 °C and an optical power output of 5 mW was carried out. There were 25 samples in the test. The lasers were selected by automatic current control (ACC) screening at 85 °C, 150 mA, and 48 h. Figure 13 shows the results of the aging tests. The driving currents ranged from 38 mA to 52 mA. The samples operated for about 4000 h. In 19 samples, the change in driving current from the initial values were within the measurement error. For the other six samples, the degradation rates were within one percent. If the lifetime is defined as 1.5 times the initial driving current, the median lifetime of P-FBH for 70 °C at 5 mW is estimated to be more than 1×10^6 h. Thus, the reliability of P-FBH lasers is very high.

6. Conclusion

We have developed a high performance P-FBH laser diode. Its excellent characteristics

have been achieved using several fabrication techniques. A high internal quantum efficiency of 94.3 percent, a very low threshold current of 5.8 mA at 25 °C, and a high temperature operation (for example, up to 15 mW at 100 °C) have been achieved. Error-floor-free transmissions at 600 Mbit/s NRZ modulation with a -80 ps/nm fiber dispersion, and 1.2 Gbit/s NRZ modulation with a -40 ps/nm fiber dispersion have been achieved. Error-floor-free transmissions at estimated to be more than 1×10^6 h for 70 °C at 5 mW, which clearly shows that the P-FBH structure has a high reliability.

References

- 1) Ishikawa, H., Soda, H., Wakao, K., Kihara, K., Kamite, K., Kotaki, Y., Matsuda, M., Sudo, H., Yamakoshi, S., Isozumi, S., and Imai, H.: Distributed Feedback Laser Emitting at 1.3 μm for Gigabit Communication Systems. *IEEE J. Lightwave Technol.*, **LT-5**, 2, pp. 848-855 (1987).
- 2) Ishikawa, H., Yamakoshi, S., and Isozumi, S.: Distributed Feedback Laser Emitting at 1.3 μm for High-Bit-Rate Systems. *FUJITSU Sci. Tech. J.*, **22**, 5, pp. 451-460 (1986).
- 3) Nakano, Y., and Noguchi, Y.: 1.3 μm Buried-Heterostructure Lasers on p-Type InP Substrates. *IEEE J. Quantum Electron.*, **QE-21**, 5, pp. 452-457 (1985).
- 4) Asano, T., and Okumura, T.: 1.3 μm High-Power BH Laser on p-InP Substrate. *IEEE J. Quantum Electron.*, **QE-21**, 6, pp. 619-622 (1985).
- 5) Sakakibara, Y., Higuchi, H., Oomura, E., Nakajima, Y., Yamamoto, Y., Goto, K., Namizaki, H., Ikeda, K., and Susaki, W.: High-Power 1.3 μm InGaAsP P-Substrate Buried Crescent Laser. *IEEE J. Lightwave Technol.*, **LT-3**, 5, pp. 978-984 (1985).
- 6) Oshiba, S., Matoba, A., Kawahara, M., and Kawai, Y.: High-Power Output over 200 mW of 1.3 μm GaInAsP VIPS Lasers. *IEEE J. Quantum Electron.*, **QE-23**, 6, pp. 783-743 (1987).
- 7) Ushijima, I., Osaka, S., Fukushima, A., Ohizumi, T., Nakai, S., Kihara, K., Isozumi, S., and Shibata, T.: 1.3 μm InGaAsP/InP Flat-Surface Buried Heterostructure Laser Diode Fabricated on P-type Substrate. Proc. SPIE, 1st Int. Conf. Indium Phosphide Related Materials Advanced Electr. **1144**, pp. 406-411 (1989).
- 8) Ishikawa, H., Imai, H., Tanahashi, T., Hori, K., and Takahei, K.: V-Grooved Substrate Buried Heterostructure InGaAsP/InP Laser Emitting at 1.3 μm Wavelength. *IEEE J. Quantum Electron.*, **QE-18**, 10, pp. 1704-1711 (1982).
- 9) Oomura, E., Higuchi, H., Sakakibara, Y., Hirano, R., Namizaki, H., Susaki, W., and Fujikawa, K.: InGaAsP/InP Buried Crescent Laser Diode Emitting at 1.3 μm Wavelength. *IEEE J. Quantum Electron.*, **QE-20**, 8, pp. 866-874 (1984).
- 10) Ohtoshi, T., Yamaguchi, K., and Chinone, N.: Analysis of Current Leakage in InGaAsP/InP Buried Heterostructure Lasers. *IEEE J. Quantum Electron.*, **QE-25**, 6, pp. 1369-1375 (1989).
- 11) Kusunoki, T., Okazaki, N., and Tanahashi, T.: Liquid Phase Epitaxial Growth of Buried Heterostructure DFB Lasers. *FUJITSU Sci. Tech. J.*, **24**, 2, pp. 133-142 (1988).
- 12) Susaki, W., and Fujikawa, K.: Internal Loss of InGaAsP/InP Buried Crescent ($\lambda = 1.3 \mu\text{m}$) Laser. *Appl. Phys. Lett.*, **41**, 4, pp. 320-321 (1982).



Katsuhiko Kihara

Optoelectronic Device Engineering Dept.
Compound Semiconductor Device Div.
FUJITSU LIMITED
Bachelor of Physics
Tsukuba University 1983
Specializing in Semiconductor Laser Technology



Ichiro Ushijima

Optoelectronic Device Engineering Dept.
Compound Semiconductor Device Div.
FUJITSU LIMITED
Bachelor of Physics
Kyushu University 1980
Specializing in Optoelectronic Device Technology



Shuichi Miura

Optoelectronic Device Engineering Dept.
Compound Semiconductor Device Div.
FUJITSU LIMITED
Bachelor of Physics
Tohoku University 1981
Specializing in Optoelectronic Device Technology

Sputtered Garnet Media for Magneto-Optic Recording

• Keiji Shono • Hiroshi Kano • Sumio Kuroda

(Manuscript received December 14, 1989)

In-situ crystallized Bi-substituted iron garnet films were deposited by RF sputtering. The films had a columnar microstructure and the surfaces were as smooth as a single crystal. They showed square hysteresis loops with large coercivity.

The films' perpendicular magnetic anisotropy is ascribed to inverse magnetostriction. A disk four inches in diameter was dynamically recorded using an Ar ion laser. The figure of merit of the disk with an Al reflector was about ten times higher than that of a magneto-optic disk made of an amorphous rare-earth transition metal. CNRs of 57 dB and 54 dB were obtained for bit lengths of 5 μm and 1.4 μm , respectively.

1. Introduction

At present magneto-optic (M-O) recording is the most highly developed erasable optical data storage technology¹⁾. Recording is performed by thermomagnetically writing magnetic domains. The readout is obtained using the magneto-optic effect such as polar Kerr rotation or Faraday rotation.

A good M-O recording medium should have 1) high coercivity to support micron or sub-micron sized domains for high-density storage, 2) a strong M-O effect to produce a large readout signal, 3) good writing sensitivity for the use of semiconductor lasers, and 4) long-term stability.

An amorphous rare-earth transition metal (RE-TM) is now the leading candidate for M-O recording media because the noise of the medium is extremely small. In addition, it has high coercivity and good writing sensitivity²⁾. However, the Kerr rotation of RE-TM is typically as small as 0.3 degrees, whereas a larger Kerr rotation is required for higher readout performance. Moreover, the chemical stability is very poor unless the film is well protected.

Bi-substituted rare-earth iron garnet (Bi:RIG) is very attractive for M-O recording media because it has a huge Faraday rotation in

the visible region³⁾. Moreover, there is no problem with long-term stability since garnet is stable oxide. Liquid phase epitaxy (LPE) has been mostly used to prepare garnet film⁴⁾. However, it is difficult to obtain a film of high coercivity, large size and high Bi-substitution using LPE. These properties are required for M-O recording media.

Recently there have been attempts to produce garnet films by sputtering⁵⁾⁻⁷⁾. It is rather easy to obtain a large uniform film with high Bi-substitution by sputtering. There are two methods for preparing a sputtered garnet film on a single crystal $\text{Gd}_3\text{Ga}_5\text{O}_{12}$ (GGG). One way is to crystallize an as-sputtered amorphous film by postannealing. The other way is to make a crystallized film during deposition, keeping the substrate temperature above 500 °C.

With Bi, Ga:YIG on GGG, there are major differences in the microstructure and magnetic properties of postannealed film and crystallized-as-deposited film⁷⁾. The crystallized-as-deposited film has a columnar microstructure and its surface is quite smooth, while the postannealed film has a granular microstructure and its surface is rather rough. The postannealed film shows a square hysteresis loop with large co-

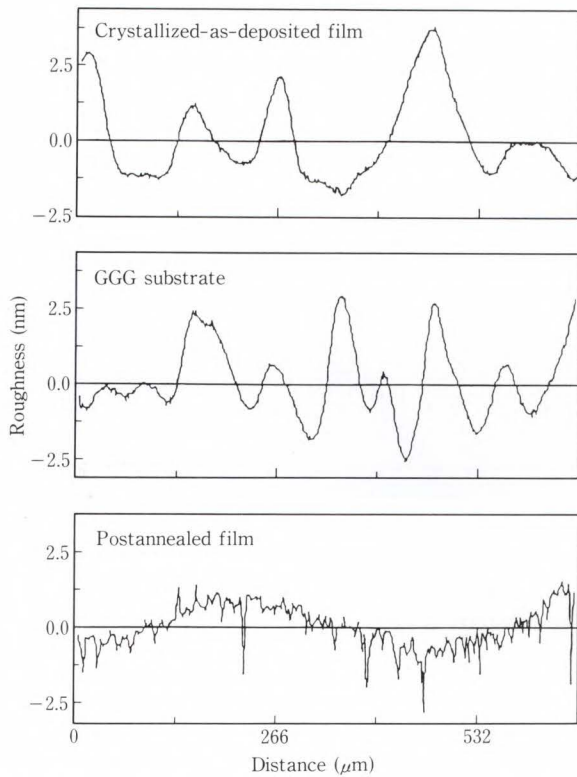


Fig. 1—Surface roughness measured by scanning optical differential interference.

eracity. But the squareness ratio and coercivity of the crystallized-as-deposited film are both small.

Postannealed film was dynamically recorded using an Ar ion laser^{8),9)}. However, the media noise was very large due to light being scattered by the granular microstructure. Crystallized-as-deposited film could conceivably be used for M-O recording, but it has not been used because of its low coercivity. To overcome this problem, the authors changed the composition to Bi, Ga:DyIG with large magnetostriction, and attained large coercivity and low noise.

This paper describes the microstructure and magnetic properties of crystallized-as-deposited Bi, Ga:DyIG films, and shows the dynamic recording characteristics using an Ar ion laser.

2. Film properties

2.1 Film preparation

Films were prepared by RF diode magnetron sputtering.

Substrates were (111) GGG wafers three

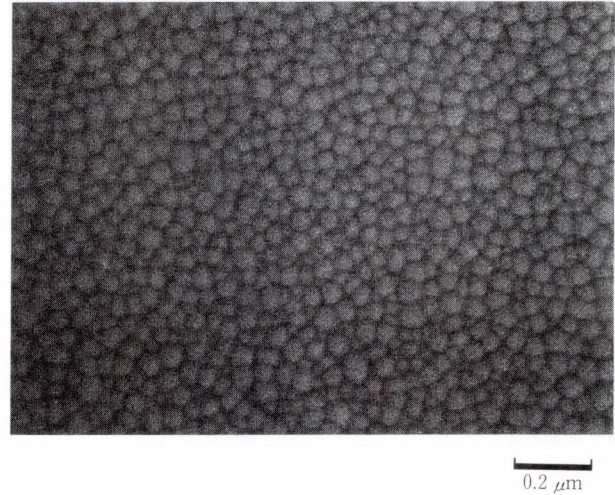


Fig. 2—FF-SEM image of the surface.

inches and four inches in diameter. The target was composed of Bi, Dy, Ga, and Fe oxide, which was made by conventional sintering. A mixture of Ar and O₂ was used as the sputtering gas. The substrates were kept at 570 °C for crystallization during deposition. The substrates were rotated to produce uniform films.

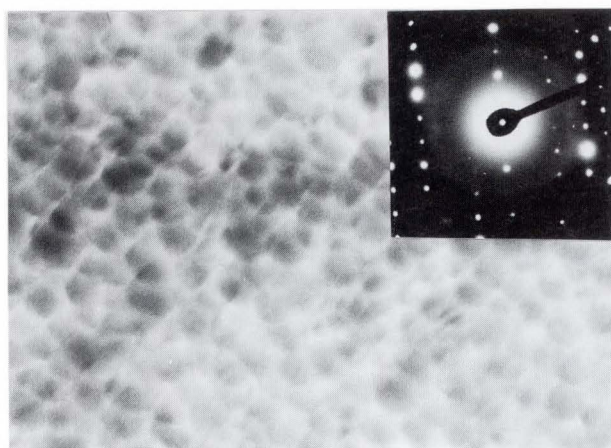
The film composition was Bi_{1.5}Dy_{1.1}Ga_{0.7}Fe_{4.6}O₁₂. This was determined by the Inductive Coupled Plasma (ICP) method assuming eight as the total number of cations.

The X-ray diffraction pattern showed only a (444) peak of garnet phase. The lattice mismatch between the film and the substrate was about one percent. No impurity phase was observed despite the large deviation from the stoichiometric value.

2.2 Surface morphology

The surface roughness of the films are shown in Fig. 1.

These were measured by the scanning optical differential interference method with a beam spot size of 1 μm. The roughness of the substrate and the postannealed film are also shown for comparison with that of the crystallized-as-deposited film. The crystallized-as-deposited film has no surface roughness except due to that of the substrate, whereas the postannealed film has its own roughness. The long-range undulations in each figure originate from the striation of the substrate.



a) Top

100 nm



b) Cross section

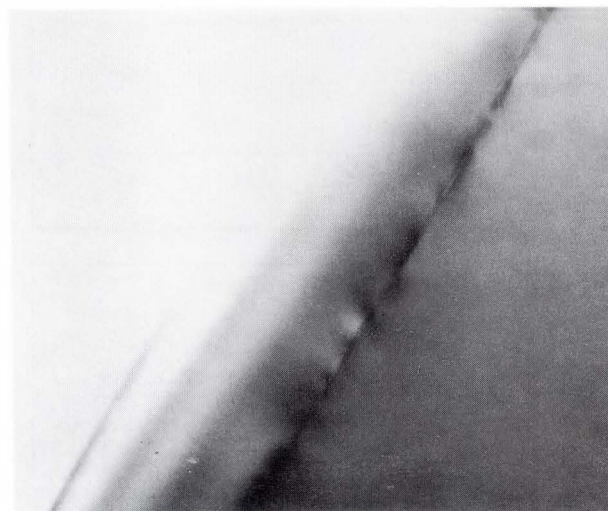
Fig. 3—TEM image of the film.

The features of the surface of the crystallized-as-deposited film could not be seen using an ordinary scanning electron microscope. But a microstructure smaller than 100 nm was revealed by field emission SEM (Hitachi S-800). This is shown in Fig. 2.

2.3 Microstructure

The microstructure was observed using a transmission electron microscope (TEM). The specimens for TEM were prepared, removing the substrate by mechanical polishing and ion milling.

Figure 3 shows the TEM images of top view and cross section of the film. Although there are small crystallites of 50 nm, the diffraction pattern is like that of a single crystal. A columnar structure is clearly seen in the cross section.



200 nm

Fig. 4—TEM image of the cross section.

The substrate is single-crystal $(\text{Gd, Ca})_3(\text{Ga, Mg})_5\text{O}_{12}$.

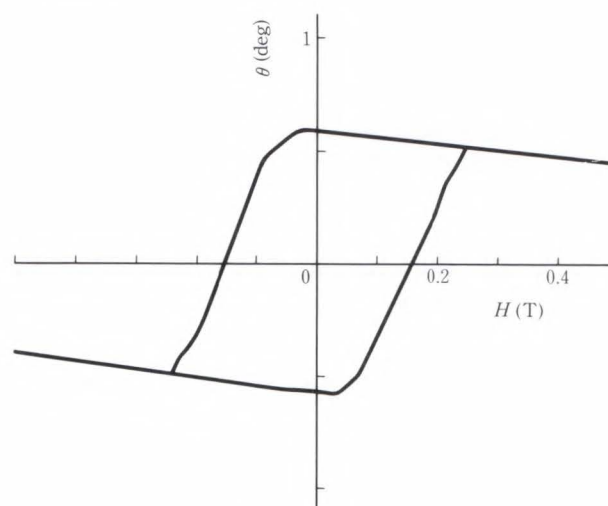


Fig. 5—Faraday hysteresis loop.

The columnar structure seems to be caused by the lattice mismatch. Figure 4 shows a cross section of the film where a single crystal $(\text{Gd, Ca})_3(\text{Ga, Mg})_5\text{O}_{12}$ was used as a substrate. In this case, the lattice mismatch was less than 0.1 percent, and no features were observed except for the interface.

2.4 Magnetic properties

The Faraday hysteresis loop is shown in Fig. 5. The coercive force of 0.16 T is not as large as that of RE-TM, but it is acceptable for M-O recording.

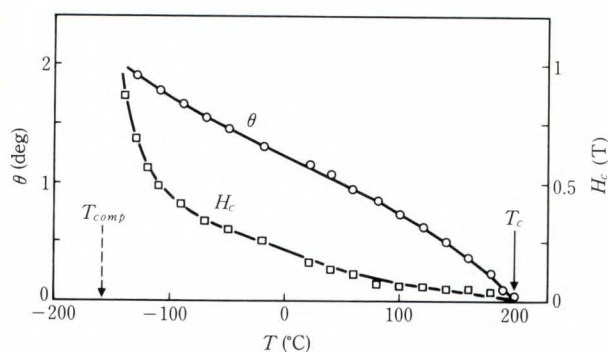


Fig. 6—Temperature dependence of Faraday rotation and coercivity.

The film thickness is 0.2 μm and the Faraday rotation was measured at a wavelength of 514 nm.

By changing the composition from Bi, Ga:YIG to Bi, Ga:DyIG, the coercivity was increased about 50 times. Even when a single crystal (Gd, Ca)₃(Ga, Mg)₅O₁₂ was used as a substrate, the coercivity was almost the same as that of the film on GGG. Therefore, the perpendicular magnetic anisotropy does not originate from the shape effect. It is considered that the perpendicular anisotropy is caused by inverse magnetostriction.

If so, the anisotropy constant, *Ku*, is given by Equation (1)¹⁰.

$$Ku = -(3/2)\lambda_{111}\sigma. \quad \dots \dots \dots (1)$$

Here, *Ku* is positive, because the magnetostriction coefficient, λ₁₁₁, is negative and the stress, σ, is positive.

DyIG has one of the largest values of λ₁₁₁ among rare-earth iron garnets which have a negative magnetostriction coefficient¹¹. Furthermore, the thermal expansion coefficient of the film is larger than that of the substrate, which causes tensile stress in the film¹². In the crystallized-as-deposited film, the stress acting along the grain boundaries is much smaller than that of postannealed film. This is why the coercivity of crystallized-as-deposited Bi, Ga:YIG film is small.

Figure 6 shows the temperature dependence of the Faraday rotation and coercive force. The Faraday rotation and coercive force decreases monotonically with increasing temperature and

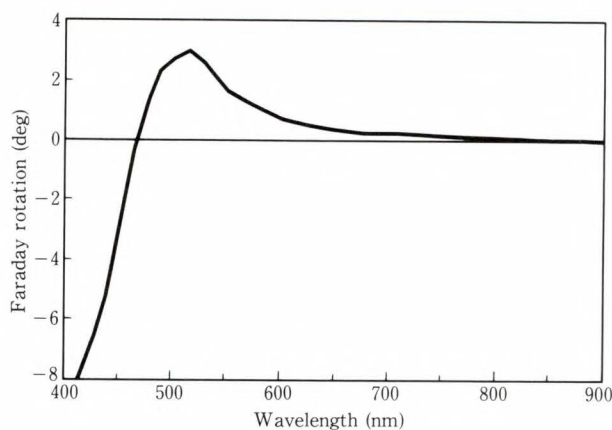


Fig. 7—Wavelength dependence of Faraday rotation. The film thickness is 0.5 μm.

they vanish at the Curie temperature of 200°C. Since the coercive force increases rapidly at low temperature, the compensation temperature seems to exist below -160 °C. The saturation magnetization was about 0.057 T at room temperature.

2.5 Faraday rotation spectrum

The wavelength dependence of Faraday rotation is shown in Fig. 7. The Faraday rotation increases with decreasing wavelength and has a maximum value around 500 nm. This is the specific Faraday rotation spectrum of Bi:RIG. The huge Faraday rotation has been ascribed to the charge transfer transition around 450 nm, which is strongly enhanced by Bi-substitution¹³.

A larger Faraday rotation near the infrared range is desirable for practical applications using a laser diode. Recently it was found that Ce-substituted garnets (Ce:YIG) have a large Faraday rotation around 800 nm^{14), 15)}.

Investigation of the applicability to M-O recording is now in progress on sputtered Ce, Ga:DyIG film¹⁶⁾.

3. Dynamic recording

3.1 Read-write system

Dynamic recording was carried out using a 514-nm Ar ion laser as a light source. An Ar laser was used in order to obtain the largest reproduced signal, as is shown in Fig. 7.

The read-write system is shown in Fig. 8.

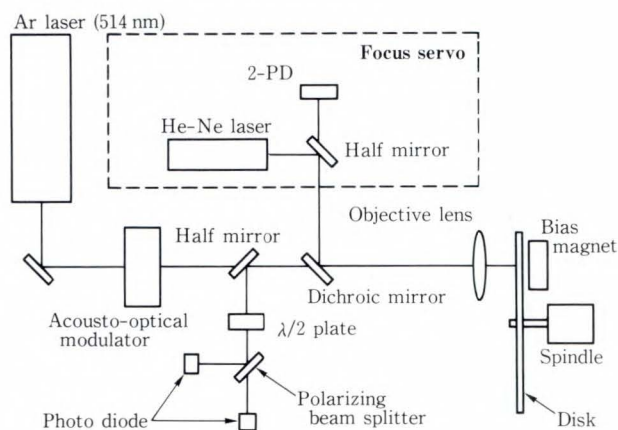


Fig. 8—Read-write system.

An acousto-optic device was used to modulate the Ar laser. A He-Ne laser was used for the focus servo. The half-width of the focused Ar laser beam was $1\ \mu\text{m}$ on the media. This value was measured by the knife-edge method. The numerical aperture of the objective lens was 0.45 and a slide glass with appropriate thickness was attached to the optical head to obtain the half-width of $1\ \mu\text{m}$. A tracking servo was not used because the disks have no tracking grooves. An ordinary differential detection scheme was used to reduce the media noise.

3.2 Disk structure

On the $0.23\ \mu\text{m}$ thick garnet film, $0.1\ \mu\text{m}$ thick Al film was deposited as a reflector. The Al film also acts as a heat absorber. Since the garnet film is still transparent at the wavelength of the Ar laser, the writing sensitivity is much improved by coating the disk with a metal reflector⁹⁾.

The reproduced signal is proportional to the figure of merit, which is defined as the product of the reflectivity R and the effective M-O rotation angle θ . Both R and θ are strongly affected by the thickness of the transparent garnet film because the interference is extremely large in the multilayer structure. Therefore, the garnet film thickness must be optimized to obtain the largest reproduced signal. A garnet film thickness of $0.23\ \mu\text{m}$ is the optimum. This was determined by both calculation and experiment¹⁷⁾.

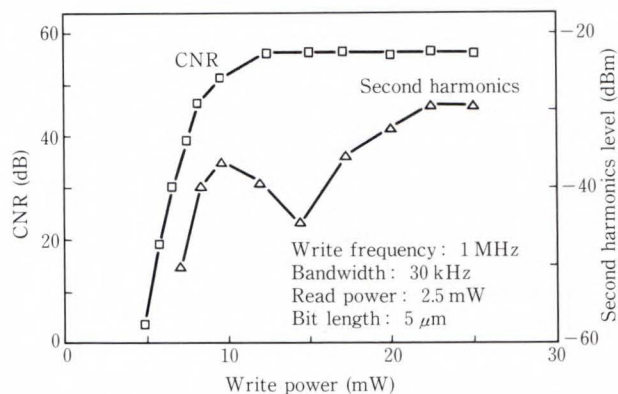


Fig. 9—Write power dependence of CNR.

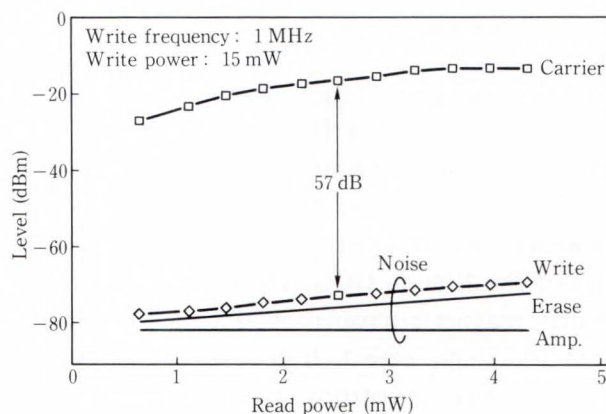


Fig. 10—Read power dependence of carrier and noise level.

The figure of merit of the optimized disk is 2.1 degrees at the wavelength of 514 nm, as θ was 4.5 degrees and R was 46 percent. This figure of merit is more than ten times that of RE-TM disk.

3.3 Read-write characteristics

Figure 9 shows the write power dependence of the carrier-to-noise ratio (CNR) at a write frequency of 1 MHz, a linear velocity of 10 m/s and a read power of 2.5 mW. The resolution bandwidth of the spectrum analyzer was 30 kHz. The threshold power is 5 mW, and CNR reaches 57 dB when the second harmonic is minimum at 15 mW. Since the threshold power of an ordinary RE-TM disk is about 4 mW under the same writing conditions, this writing sensitivity is moderate. The writing sensitivity can be improved if more absorptive metal such as Cr is used as a reflector⁹⁾.

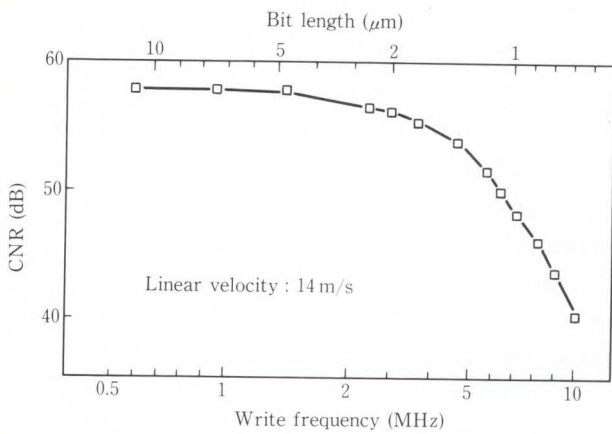


Fig. 11—Write frequency dependence of CNR.

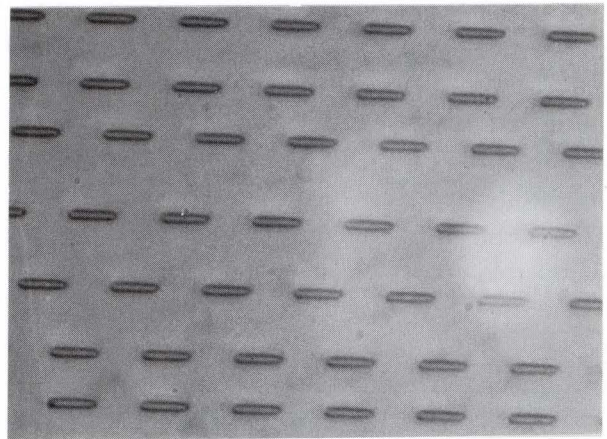


Fig. 13—Recorded bits.

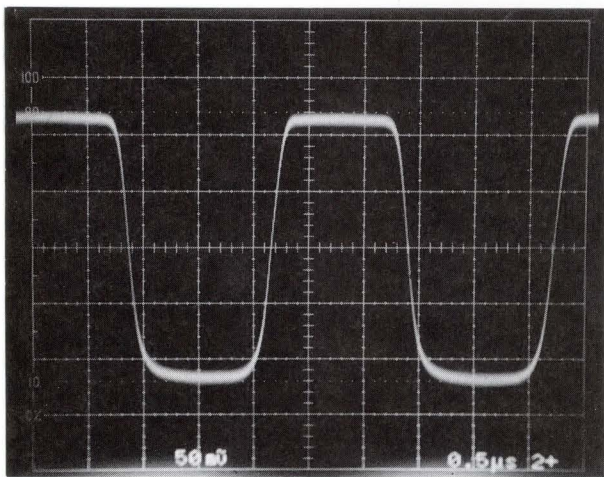


Fig. 12—Reproduced signal.

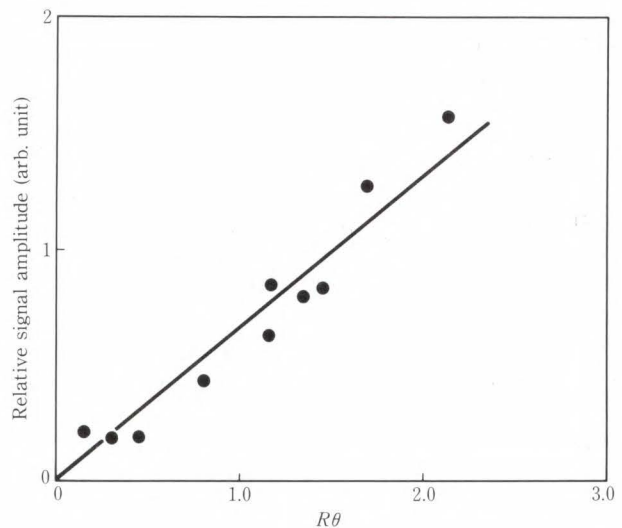


Fig. 14—Relative signal amplitude vs. $R\theta$.

The read power dependence of the carrier and noise level at the optimum write power is given in Fig. 10. The noise level increases by 2 dB after recording. The erase noise level was compared with that of a typical RE-TM disk with the same read-write system under the same conditions. It was found that the erase noise level of sputtered garnet disk was only 1 dB higher.

The write frequency dependence of CNR is shown in Fig. 11. CNR decreases gradually with increasing write frequency or decreasing bit length. This is because the bit length becomes close to the beam size. At 5 MHz, the CNR is 54 dB.

Since the linear velocity is 14 m/s, the bit length is only 1.4 μm . This value of CNR is

slightly higher than that of a typical RE-TM disk.

The reproduced signal and recorded bits are shown in Figs. 12 and 13. The bit width is 1 μm and the edges of the bits are very sharp. The sharp edges of bits lead to low write noise.

3.4 Signal amplitude

Though a good CNR was obtained, it was much smaller than expected. The figure of merit of the sputtered garnet disk is more than ten times that of an RE-TM disk, and the noise level was comparable. Therefore, the CNR of a sputtered garnet disk is to be 20 dB higher than that of an RE-TM disk.

The CNR sometimes greatly depends on the read-write system. To check that the M-O signal was correctly obtained, the signal amplitude was measured for various sputtered garnet disks. Figure 14 shows the relative signal amplitude dependence on the figures of merit. The signal amplitude is proportional to the figure of merit, as determined theoretically. Therefore, the read-write system may be thought to be insensitive to the M-O signal, as the slope of the straight line in Fig. 14 is small.

One possible reason for the low CNR is that the optical components in the read-write system were not well optimized. For example, when the M-O rotation angle is very large, the half-mirror placed before the half-wave plate must be chosen considering the appropriate separation ratio of the p- and s-wave. If the half-mirror is not chosen appropriately, the signal amplitude is reduced to about half by incomplete differential detection. However, a big difference will still remain between the obtained CNR and the predicted one even after the read-write system is well optimized.

The other reason might be related to ellipticity, which is caused by the Faraday effect or birefringence. How much the ellipticity influences the signal amplitude is not clear, and this seems to be the key to obtaining the predicted CNR.

4. Conclusion

Films of high quality and good magnetic properties were produced by crystallizing Bi, Ga:DyIG films on GGG during deposition. The film has a columnar microstructure resembling a single crystal and a square hysteresis loop with large coercivity. The perpendicular magnetic anisotropy is ascribed to the inverse magnetostriction of DyIG.

The figure of merit of the optimized disk is more than ten times that of RE-TM disk. A CNR as high as 54 dB was obtained for a bit length of 1.4 μm using Ar laser. The noise level was comparable to that of RE-TM disk, and high-density recording is possible.

A high CNR is a great advantage for high-density recording. In addition, the recording

density can be increased by using a laser diode with a shorter wavelength. A high-power visible laser diode will be available in the near future. The CNR of the RE-TM disk has already reached the theoretical limit of its ability. But it is not necessarily sufficient for use in a computer memory that requires a very high data rate.

Sputtered garnet film is promising for the next generation of M-O disks having ultra-high recording density and high reliability.

References

- 1) Lin, C.-J.: Materials for magneto-optic data storage. *Mat. Res. Soc. Symp. Proc.*, **150**, pp. 15-31 (1989).
- 2) Kryder, M.H.: The design and fabrication of magneto-optic recording materials. *Mat. Res. Soc. Symp. Proc.*, **150**, pp. 3-14 (1989).
- 3) Scott, G.B., and Lacklison, D.E.: Magneto-optic Properties and Applications of Bismuth Substituted Iron Garnets. *IEEE Trans. Magn.*, **MAG-12**, 4, pp. 292-311 (1976).
- 4) Levinstein, H.J., Licht, S., Landorf, R.W., and Blank, S.L.: Growth of High-Quality Garnet Thin Films from Supercooled Melts. *Appl. Phys. Lett.*, **19**, 11, pp. 486-488 (1971).
- 5) Gomi, M., Utsugi, K., and Abe, M.: RF sputtered film of Bi-substituted garnet for magneto-optical memory. *IEEE Trans. Magn.*, **MAG-22**, 5, pp. 1233-1235 (1986).
- 6) Krumme, J.P., Doormann, V., Stroocka, B., and Willich, P.: Selected-area sputter epitaxy for iron-garnet films. *J. Appl. Phys.*, **60**, 6, pp. 2065-2068 (1986).
- 7) Shono, K., Kano, H., Koshino, N., and Ogawa, S.: Microstructure of sputtered garnet films for magneto-optical recording. *J. Appl. Phys.*, **63**, 8, pp. 3639-3641 (1988).
- 8) Kano, H., Shono, K., Koshino, N., and Ogawa, S.: Read/write characteristics of sputtered garnet optical disks. Digest 10th Ann. Conf. Magnetics, Jpn., 1986, p. 32.
- 9) Shono, K., Kano, H., Koshino, N., and Ogawa, S.: Magneto-optical recording of sputtered garnet films using laser diode. *IEEE Trans. Magn.*, **MAG-23**, 5, pp. 2970-2972 (1987).
- 10) Heinz, D.M., Bezzer, P.J., Owens, J.M., Mee, J.E., and Pullian, G.R.: Mobile Cylindrical Magnetic Domains in Epitaxial Garnet Films. *J. Appl. Phys.*, **42**, 4, pp. 1243-1251 (1971).
- 11) Iida, S.: Anomalous Magnetostriction of $\text{Tb}_3\text{Fe}_5\text{O}_{12}$

and $\text{Eu}_3\text{Fe}_5\text{O}_{12}$. *Phys. Lett.*, **6**, 2, pp. 165-167 (1963).

- 12) Besser, P.J., Mee, J.E., Elkins, P.E., and Heinz, D.M.: A Stress Model for Heteroepitaxial Magnetic Oxide Films Grown by Chemical Vapor Deposition. *Mater. Res. Bull.*, **6**, 11, pp. 1111-1123 (1971).
- 13) Hansen, P., and Krumme, J.P.: Magnetic and magneto-optical properties of garnet films. *Thin Solid Films*, **114**, pp. 69-107 (1984).
- 14) LeGall, H., Guillot, M., Marchand, A., Nomi, Y., Artinan, M., and Desvignes, J.M.: Faraday rotation in bismuth substituted iron garnets. Advances in magneto-optics, *J. Magn. Soc., Jpn.*, **11**, Suppl. S1,

pp. 235-340 (1987).

- 15) Gomi, M., Satoh, K., and Abe, M.: Giant Faraday rotation of Ce-substituted YIG films epitaxially grown by RF sputtering. *Jpn. J. Appl. Phys.*, **27**, 8, pp. L1536-L1538 (1988).
- 16) Alex, M., Shono, K., Kuroda, S., Koshino, N., and Ogawa, S.: Ce-substituted garnet media for magneto-optic recording. To appear in *J. Appl. Phys.*, May, 1990.
- 17) Kano, H., Shono, K., Kuroda, S., Koshino, N., and Ogawa, S.: Optimized structure of sputtered garnet disk. *IEEE Trans. Magn.*, **MAG-25**, 5, pp. 3737-3841 (1989).



Keiji Shono

Optical Disks Laboratory
FUJITSU LABORATORIES,
KAWASAKI
Bachelor of Electronics Eng.
Waseda University 1973
Dr. of Electronics Physics
Tokyo Institute of Technology 1982
Specializing in Magnet-Optic Materials



Sumio Kuroda

Optical Disks Laboratory
FUJITSU LABORATORIES,
KAWASAKI
Bachelor of Electronics Eng.
Gunma University 1987
Specializing in Materials Science



Hiroshi Kano

Optical Disks Laboratory
FUJITSU LABORATORIES,
KAWASAKI
Bachelor of Physics
Kyoto University 1980
Master of Physics
Kyoto University 1982
Specializing in Materials Science

Overseas Offices

Abu Dhabi Office

Suite 802, A1 Masaoed Tower,
Seikh Hamdan Street, Abu Dhabi,
U.A.E.
Telephone: (971-2)-333440
FAX: (971-2)-333436

Algiers Office

9, Rue Louis Rougie Chateau Neuf,
E1 Biar, Alger 16030, Algeria
Telephone: (213)-2-78-5542
Telex: 408-67522

Amman Office

P.O. Box 5420, Ammán, Jordan
Telephone: (962)-6-62417
FAX: (962)-6-62417

Bangkok Office

Room 405, 4th Floor, Dusit
Thani Bldg., 1-3, Rama IV,
Bangkok, Thailand
Telephone: (66-2)-236-7930
FAX: (66-2)-238-3666

Beijing Office

Room 1601, Scite Tower
Jianguomen-wai Dajie, Beijing,
People's Republic of China
Telephone: (86-1)-512-3610
FAX: (86-1)-512-9041

Bogotá Office

Cra. 13 No. 27-50,
Edificio Centro Internacional
Tequendama, Interior 326,
Bogotá, D.E. Colombia
Telephone: (57-1)-286-7061
FAX: (57-1)-286-7148

Brussels Office

Avenue Louise 176, Bte 2
1050 Brussels, Belgium
Telephone: (32-2)-648-7622
FAX: (32-2)-648-6876

Hawaii Branch

6660 Hawaii Kai Drive, Honolulu,
HI 96825, U.S.A.
Telephone: (1-808)-395-2314
FAX: (1-808)-396-0059

Indonesia Project Office

16th Floor, Skyline Bldg.,
Jalan M.H. Thamrin No. 9,
Jakarta, Indonesia
Telephone: (62-21)-3105710
FAX: (62-21)-3105983

Jakarta Office

16th Floor, Skyline Bldg.,
Jalan M.H. Thamrin No. 9,
Jakarta, Indonesia
Telephone: (62-21)-333245
FAX: (62-21)-327904

Kuala Lumpur Office

Letter Box No. 47, 22nd Floor,
UBN Tower No. 10, Jalan P.
Ramlee, 50250, Kuala Lumpur,
Malaysia
Telephone: (60-3)-238-4870
FAX: (60-3)-238-4869

London Office

2, Longwalk Road, Stockley Park,
Uxbridge, Middlesex, UB11 1AB,
England
Telephone: (44-81)-573-4444
FAX: (44-81)-573-2643

Munich Office

c/o DV18 Siemens AG, Otto-
Hahn-Ring 6, D-8000, München
83, F.R. Germany
Telephone: (49-89)-636-3244
FAX: (49-89)-636-45345

New Delhi Office

Flat No. 517-B, 5th Floor, World
Trade Centre, Barakhamba Lane,
New Delhi, 110001, India
Telephone: (91-11)-331-1311
FAX: (91-11)-332-1321

New York Office

680 Fifth Avenue, New York,
N.Y. 10019, U.S.A.
Telephone: (1-212)-265-5360
FAX: (1-212)-541-9071

Paris Office

Batiment Aristote,
Rue Olof Palme 94006,
Creteil Cedex, France
Telephone: (33-1)-4-399-0897
FAX: (33-1)-4-399-0700

Shanghai Office

Room 1504 Ruijin Bldg.,
205 Maoming Road South,
Shanghai, People's Republic
of China
Telephone: (86-21)-336-462
FAX: (86-21)-336-480

Taipei Office

Sunglow Bldg., 66, Sung Chiang
Road, Taipei, Taiwan
Telephone: (886-2)-561-7715
FAX: (886-2)-536-7454

Washington, D.C. Office

Republic Place, 1776 Eye Street,
N.W. Washington D.C., U.S.A.
Telephone: (1-202)-331-8750
FAX: (1-202)-331-8797

Overseas Subsidiaries

		Telephone	Facimile
FKL Dong-Hwa Ltd.	338-13, Daehong-Ri, Sunghwan-Eub, Chunwon-Gun, Chungnam, Republic of Korea	(82-417)-4-3660	(82-417)-63-3671
Fujian Fujitsu Communications Software Ltd.	Wu, Li Ting, Fu Ma Lu, Fuzhou, Fujian Province, People's Republic of China	(86-591)-560070	(86-591)-560022
Fujitsu America, Inc.	3055 Orchard Drive, San Jose, CA 95134-2017, USA	(1-408)-432-1300	(1-408)-432-1318
Fujitsu Australia Ltd.	475 Victoria Ave., Chatswood, NSW 2067, Australia	(61-2)-410-4555	(61-2)-411-8603
Fujitsu Australia Software Technology Pty. Ltd.	1st Floor, Techway House, 18 Rodborough Road, French Forest, N.S.W. 2086, Australia	(61-2)-936-1111	(61-2)-975-2899
Fujitsu Business Communication System, Inc.	3190 Miraloma Ave., Anaheim, CA 92806, USA	(1-714)-630-7721	(1-714)-630-7660
(Sales Headquarter)	2411 West 14th Street, Tempe, AZ 85281, USA	(1-602)-921-5900	(1-602)-921-5999
Fujitsu Canada, Inc.	6280 Northwest Drive, Mississauga, Ontario, Canada L4V 1J7	(1-416)-673-8666	(1-416)-673-8677
Fujitsu Component (Malaysia) Sdn. Bhd.	No. 1, Lorong Satu, Kawasan Perindustrian Parit Raja, 86400 Batu Pahat, Johor, Malaysia	(60-7)-482111	(60-7)-481-771
Fujitsu Component of America, Inc.	3330 Scott Boulevard, Santa Clara, CA 95054-3197, USA	(1-408)-562-1000	(1-408)-748-7655 or (1-408)-727-0355
Fujitsu Customer Service of America, Inc.	12670 High Bluff Drive, San Diego, CA 92130-2103, USA	(1-619)-481-4004	(1-619)-481-5175
Fujitsu Deutschland GmbH	Frankfurter Ring 211, 8000 München 40, F.R. Germany	(49-89)-323-780	(49-89)-323-78100
Fujitsu do Brasil Ltda.	Rua Manoel da Nóbrega, 1280-2 Andar, C.E.P. 04001, São Paulo, SP, Brazil	(55-11)-885-7099	(55-11)-885-9132
Fujitsu España, S.A.	Edificio Torre Europa 5ª, Paseo de la Castellana, 95, 28046 Madrid, Spain	(34-1)-581-8000	(34-1)-581-8300
Fujitsu Europe Ltd.	2, Longwalk Road, Stockley Park, Uxbridge, Middlesex, UB11 1AB, England	(44-81)-573-4444	(44-81)-573-2643
Fujitsu Finance (U.K.) PLC	2, Longwalk Road, Stockley Park, Uxbridge, Middlesex, UB11 1AB, England	(44-81)-569-1628	(44-81)-573-2643
Fujitsu France S.A.	Bâtiment Aristote 17, Rue Olof Palme 94006, Creteil Cedex, France	(33-1)-4-399-4000	(33-1)-4-399-0700
Fujitsu Hong Kong Ltd.	Room 2521, Sun Hung Kai Centre, 30 Harbour Road, Hong Kong	(852)-8915780	(852)-721724 or (852)-8383630
Fujitsu Imaging Systems of America, Inc.	3 Corporate Drive, Commerce Park, Danbury, CT 06810, USA	(1-203)-796-5400	(1-203)-796-5665 or (1-203)-796-5723
Fujitsu International Finance (Netherlands) B.V.	Officia 1, De Boelelaan 7, 1083 HJ Amsterdam, The Netherlands	-	-
Fujitsu Italia S.p.A.	Via Melchiorre, Gioia No. 8, 20124 Milano, Italy	(39-2)-657-2741	(39-2)-657-2257
Fujitsu Korea Ltd.	9th Floor, Korean Reinsurance Bldg., 80, Susong-Dong, Chongro-Gu, Seoul Special City, Republic of Korea	(82-2)-739-3281	(82-2)-739-3294
Fujitsu Microelectronics Asia Pte. Ltd.	No. 2, Second Chin Bee Road, Jurong Town, Singapore 2261, Singapore	(65)-265-6511	(65)-265-6275
Fujitsu Microelectronics, Inc.	3545 North First Street, San Jose, CA 95134-1804, USA	(1-408)-922-9000	(1-408)-432-9044
Fujitsu Microelectronics Ireland Limited	Greenhills Centre, Greenhills Road, Tallaght, Dublin 24, Ireland	(353-1)-520744	(353-1)-520539
Fujitsu Microelectronics Italia S.r.l.	Centro Direzionale, Milanofiori, Strada No. 4-Palazzo A2, 20090 Assago-Milano, Italy	(39-2)-824-6170	(39-2)-824-6189
Fujitsu Microelectronics Limited	Hargrave House, Belmont Road, Maidenhead, Berkshire SL6 6NE, U.K.	(44-628)-76100	(44)-628-781484
Fujitsu Microelectronics (Malaysia) Sdn. Bhd.	Pesiaran Kuala Selangor, Seksyen 26, 40000 Shah Alam, Selangor Darul Ehsan, Malaysia	(60-3)-511-1155	(60-3)-511-1227
Fujitsu Microelectronics Pacific Asia Limited	Rooms 616-617, Tower B, New Mandarin Plaza, 14 Science Museum Road, Tsimshatsui East, Kowloon, Hong Kong	(852-3)-723-0393	(852-3)-721-6555
Fujitsu Mikroelektronik GmbH	Lyoner Strasse 44-48, Arabella Centre 9. OG/A, 6000 Frankfurt/Niederrad 71, F.R. Germany	(49-69)-66320	(49-69)-6632122
Fujitsu Network Switching of America, Inc.	4403 Bland Road, Somerset Park, Raleigh, NC 27609, USA	(1-919)-790-2211	(1-919)-790-8376
Fujitsu New Zealand Ltd.	6th Floor, National Insurance House, 119-123 Featherston Street, Wellington, New Zealand	(64-4)-733-420	(64-4)-733-429
Fujitsu Nordic AB	Torggatan 8, S-171 54 Solna, Sweden	(46-8)-764-7690	(46-8)-28-0345
Fujitsu Philippines, Inc.	2nd Floor, United Life Bldg., Pasay Road, Legaspi Village, Makati, Metro Manila, Philippines	(63-2)-85-49-51	(63-2)-817-7576
Fujitsu (Singapore) Pte. Ltd.	200, Cantonment Road, #11-01 South Point, Singapore 0208, Singapore	(65)-224-0159	(65)-225-5075
Fujitsu Systems Engineering of America, Inc.	2986 Oakmead Village Court, Santa Clara, CA 95051, USA	(1-408)-988-8012	(1-408)-492-1982
Fujitsu Systems of America, Inc.	12670 High Bluff Drive, San Diego, CA 92130-2013, USA	(1-619)-481-4004	(1-619)-481-4093
Fujitsu (Thailand) Co., Ltd.	3rd Floor, Olympia Thai Bldg., 444 (3rd Floor), Rachadaphisek Road, Bangkok 10310, Thailand	(662-512)-1736	(662-513)-2574
Fujitsu Vitória Computadores e Serviços Ltda.	Avenida Nossa, Senhora da Penha, 570, 8º Andar, Paraia do Canto-Vitória-Espirito Santo, Brazil	(55-27)-225-0355	(55-27)-225-0954
Information Switching Technology Pty. Ltd.	Level 32, 200 Queen Street, Melbourne 3000, Australia	(61-3)-670-4755	-
Intellistor, Inc.	2402 Clover Basin Drive, Longmont, Colorado 80503, USA	(1-303)-682-6400	(1-303)-682-6401
Tatung-Fujitsu Co., Ltd.	5 Floor Tatung Bldg., 225, Nanking East Road 3rd Section, Taipei, Taiwan	(886-2)-713-5396	(886-2)-717-4644

FUJITSU LIMITED

6-1, Marunouchi 1-chome, Chiyoda-ku, Tokyo 100, Japan

Phone: National (03) 216-3211 International (Int'l Prefix) 81-3-216-3211 Telex: J22833 Cable: "FUJITSULIMITED TOKYO"